The Pennsylvania State University

The Graduate School

College of Earth and Mineral Sciences

LABORATORY STUDIES OF FAULT RESTRENGTHENING:

THE ROLE OF SHEAR STRESS AND MINERALOGY INFERRED FROM MECHANICAL AND ULTRASONIC AMPLITUDE MEASUREMENTS

A Dissertation in

Geosciences

by

Kerry L. Ryan

Submitted in Partial Fulfillment

of the Requirements

for the Degree of

Doctor of Philosophy

December 2018

The dissertation of Kerry L. Ryan was reviewed and approved* by the following:

Chris Marone
Professor of Geosciences
Dissertation Advisor
Chair of Committee

Charles J. Ammon
Professor of Geosciences

Demian Saffer
Department Head and Professor of Geosciences

Parisa Shokouhi
Associate Professor of Engineering Science and Mechanics

Mark Patzkowsky
Head of Graduate Programs and Research

*Signatures are on file in the Graduate School

ABSTRACT

During the seismic cycle, faults repeatedly fail and regain strength. The gradual strength recovery is often referred to as frictional healing, and existing works suggest that healing can play an important role in determining the mode of fault slip ranging from dynamic rupture to slow earthquakes. Laboratory studies can play an important role in identifying the processes of frictional healing and their evolution with shear strain during the seismic cycle. These studies also provide data for laboratory-derived friction constitutive laws, which can improve dynamic earthquake models.

In this dissertation, I aim to understand how shear stress impacts frictional restrengthening processes in a variety of fault materials. Specifically, how does stress dependent healing differ between Westerly granite bare surfaces and Westerly granite gouge and how does the presence of phyllosilicates influence shear stress dependent healing behavior. To investigate these questions, I utilize both traditional frictional analysis and work to understand if and how ultrasonic amplitude measurements can add to our understanding of healing processes.

In Chapter 1, I investigate the difference in healing mechanisms between Westerly granite bare surfaces and Westerly granite gouge. I find that the shear stress dependence previously observed in granular quartz holds true for Westerly gouge and likely arises from the granular nature of gouge material as this behavior is not observed in bare surface experiments. In Chapter 2, I investigate how mineralogy impacts shear stress dependent frictional behavior with the addition of phyllosilicates by analyzing the frictional healing behavior of synthetic quartz and smectite mixtures along with several natural fault gouges. The interplay between frictionally strong materials (quartz, feldspar, and calcite) and frictionally weak materials (smectite, illitie, and kaolinite) is complex but I find that phyllosilicates can significantly reduce the overall frictional strength and restrengthening of synthetic quartz gouge mixtures. The presence of 30% smectite in

synthetic mixtures can entirely remove the shear stress dependence observed in quartz. Finally, Chapter 3 focuses on ultrasonic amplitude measurements and understanding how they vary as a function of normal stress and layer thickness. In Chapters 1 and 2 we use ultrasonic amplitudes to continuously probe the frictional state of laboratory faults and in Chapter 3 we work to understand how we can interpret the changes in amplitude we observe during biaxial experiments in the earlier chapters.

This dissertation provides insight to the complex healing behaviors that may arise based on stress state and mineralogy of faults. It also presents lab scale relationships for amplitude based on normal stress and layer thickness which help us to understand the conditions in which ultrasonic amplitude can be used to monitor frictional state.

TABLE OF CONTENTS

List of Tables

List of Figures

Acknowledgments

These past five or so years has been an experience like no other. Transitioning into adulthood is hard enough as is, but diving into a new field of study and seemingly new world of scientific research was sometimes overwhelming. I owe a great deal of gratitude to all the people who helped along the way and provided guidance, support, and assistance and made me feel at home in the geoscience community.

First, I have to thank my advisor, Dr. Chris Marone, who welcomed me into the lab and trusted me to use his very expensive equipment despite my occasional habit of breaking things. His 'if you're not breaking it, you're not trying' attitude encouraged me to never be afraid to test out new ideas. In addition, to providing the resources necessary for a successful doctorate Chris was also a very caring and compassionate advisor. He was first and foremost concerned with the well-being of his students. He provided great opportunities for me throughout my time here and was an endless source of knowledge on rock deformation, the State College Spikes, and brewing beer. All essential to my time at PSU.

I would also like to thank the other members of my thesis committee. Your discussions and suggestions played a valuable role in the progression of my work. It is no small commitment to serve as a committee member and I appreciate the time and effort you invested in my project and me.

I do not think my rock mechanics lab family would ever forgive me if I did not take the time to properly thank them. My time here was greatly improved by the presence of my labmates. Everyone was always willing to lend a hand with an experiment or outreach event or to provide an extra set of eyes on a paper draft (sorry Sharan about that time I forgot to read yours) or abstract submission. Sharing a working environment with so many wonderful people made the difficult days manageable and the good days that much better. Thanks to John and Marco for

welcoming me to the lab and training me as a young experimentalist and promoting a work environment where I felt comfortable asking questions. A big thank you to Abby Kenigsberg for reading through more dissertation drafts than I can count and for 5 years of award winning chili making. And thank you to Peter Miller for being my first grad school friend and sticking with me through the years even when times were tough (like when you had to teach me how to make strike and dip measurements).

I would also like to thank coach Ben Madara and the lab lift team for motivating me to go to the gym which benefitted my physical and emotional well-being. A big thanks to Chas for all the Duck donut breaks and Sharan for bubble tea adventures.

All lab functions were made possible by the one and only Steve Swavely. Thank you for keeping the lab well stocked and running smoothly. I know it is no easy job getting parts ordered and delivered on such short notice and for making sure our samples always made it to their proper homes. Thanks for all the great lunch days, word jumbles, and for introducing us to the Centre Country dairy Princess!

Next, I would like to thank my family for their unconditional love and support. Sometimes I was not sure if you actually knew what I was doing here but as long as I was happy and pursuing my interests that was really all you could ask for. Thank you to my parents for coming to visit and understanding when I forgot to call (basically all the time). Thanks to my sister for always be free for a chat about life and my brother for ignoring 6 or more consecutive texts from me on a regular basis. Love you both anyway.

A big thank you to all my other friends who were there for me along the way! Especially Rebecca VanderLeest, who no matter how near or far always had my back and provided much needed feedback and encouragement!

Introduction

Fault healing is the process by which fault materials restrengthen after an earthquake. This phenomenon has been observed on natural faults (Marone et al, 1995; Tadokoro and Ando, 2002; Li et al, 2003) and in laboratory experiments (Dieterich, 1972; Marone, 1998a). During an earthquake, slip along a fault causes the frictional strength to decrease as stress stored elastically in the fault is released. In order to host subsequent events, the fault must regain strength during the inter-seismic period as stress accumulates. Laboratory studies have been used to systematically investigate the frictional properties of natural and simulated fault materials (Dieterich 1981; Marone 1998a; Tesei et al, 2012; Carpenter et al, 2016).

Fault healing is cited as a possible control for earthquake nucleation, stress drop, and recurrence interval. Understanding fault restrengthening and processes that control earthquake rupture and propagation are important for calculating risk and hazard potential in the vicinity of seismically active faults. Strength depends on a number of factors including mineralogy, hydrological and mechanical properties. Previous work suggests that fault restrengthening is shear stress dependent (Karner and Marone, 1998; 2001; Nankatani and Mochizuki, 1996). This implies that changing the stress state of a fault during the inter-seismic period can play a major role in determining its frictional strength.

Frictional restrengthening can also have an important impact on fault stability which determines the mode of fault slip. In the past, stick-slip behavior was commonly studied as an analog for earthquakes (Brace and Byerlee, 1966; Byerlee and Brace 1986). More recently, studies have focused on investigating the full spectrum of slip behavior from aseismic creep to dynamic rupture, including slow-slip earthquakes and tremors (Johnson et al, 2012; Kaparoth and Marone,

2013; Leeman et al., 2016; Scuderi et al, 2017b). Fault stability is controlled by fault stiffness. More compliant systems are more likely to exhibit unstable sliding behavior. As faults heal and new frictional contacts form, we expect the system to stiffen which can promote fault stability and influence the mode of failure. Therefore, it is possible that shear stress dependent healing could be related to slow-slip which occurs when the fault stiffness is close to the critical stiffness boundary, above which the system slips stably and below which unstable slip is possible.

Slide-hold-slide (SHS) tests traditionally have investigated healing on laboratory faults where the analog stress drop or stress relaxation is minimal and governed by creep relaxation. However, it is important to understand how the stress state of a fault can impact healing as there is evidence that faults can experience complete unloading. For example, a study of the 2011 Tohoku earthquake suggests that the fault was completely unloaded during the event, based on the observed rotation in the maximum stress axis (Hasegawa, et al 2011). Earthquake stress drops are typically on the order of a few megapascals. For shallow faults, in areas where the magnitude of the ambient stress field is low, a stress drop of this size could also result in complete unloading of the fault. Understanding the relationship between shear stress and fault healing can provide insight into how loading and unloading of faults by nearby earthquakes or other stress perturbations may influence frictional healing. This knowledge can also benefit the oil and gas industry for applications in hydraulically fractured reservoirs. In unconventional reservoirs, pressurized fluids are used to induce new fractions and increase hydrocarbon recovery. This research could help understand how these newly formed fractures will heal which has implications for fault permeability.

Mechanical data have traditionally been used to investigate restrengthening processes in laboratory faults by comparing the peak friction after the analog inter-seismic period and the steady-state sliding friction before the inter-seismic period. In these experiments, the measured

change in friction involves processes that occur during the analog co-seismic, inter-seismic, and post-seismic phases. However, we are interested in understanding the processes that occur during each of these phases and cannot investigate them independently with frictional data alone. Therefore, to investigate these processes on the lab scale we use ultrasonic wave amplitude measurements.

Ultrasonic waves have been used as a nondestructive method for investigating the physical and frictional properties of intact rocks and granular fault gouges for a variety of applications on the field and laboratory scale. Ultrasonic emission and active source propagation studies have been used successfully to investigate rock deformation processes (Lockner, D., 1993; Nagata et al, 2008; Nagata et al, 2012; Johnson et al, 2013; Tinti et al, 2016; Scuderi et al, 2017a; Gheibi and Hedayat, 2018). A majority of these studies have focused on techniques that monitor changes in ultrasonic velocity. Interpretation of amplitude variation during laboratory experiments is complicated because samples experience changes in stress state and layer thickness which also influence amplitude. Limited studies have focused on systematic variations in ultrasonic amplitude with these important experimental parameters (Gheibi and Hedayat, 2018).

However, ultrasonic amplitude can provide unique insight into deformation processes and contact area evolution (Nagata, et al, 2008). Ultrasonic wave amplitude will vary as a function of applied stress, contact area, and sample thickness. The relationships between these parameters are not well studied for granular fault materials. In Chapters 1 and 2 we discuss observations of acoustic amplitudes during deformation experiments. In Chapter 3 our primary concern is deconvolving the portions of the signal resulting from layer thickness changes and the portion we

can attribute to time and slip dependent healing that alter the material properties and frictional state of laboratory faults during SHS tests.

Chapter 1

Shear Stress Dependent Fault Healing and Frictional Aging of Westerly Granite

K.L. Ryan[1], J. Rivière[2], C. Marone[1]

[1]Dept of Geosciences, Pennsylvania State Univ., University Park, PA 16802, USA
[2]Univ. Grenoble Alpes, ISTerre, F-38000 Grenoble, France

1.1 Abstract:

The seismic cycle involves repeated failure and strength recovery of tectonic faults, known as fault healing. In Earth's crust, where fault strength is dominated by friction, frictional healing is the primary agent of fault healing. Laboratory studies document the role of contact aging and cementation as key mechanisms of frictional healing, however the role of shear stress is not well understood. We describe a laboratory study of frictional healing as a function of shear stress for bare granite surfaces and simulated fault gouge composed of Westerly granite and quartz. Faults are sheared at normal stresses of 5-25 MPa, 100% relative humidity and room temperature. We quantify frictional healing in slide-hold-slide tests for shear stresses from 0 to the sliding friction value and monitor the amplitude of elastic waves propagating across the fault zone. Healing of gouge shows a strong negative dependence on shear stress whereas healing of bare surfaces does not vary systematically with shear stress. In gouge, frictional healing involves shear stress dependent compaction and particle rearrangement, while for bare surfaces frictional strength is derived primarily from contact area evolution. The magnitude of compaction in gouge varies with shear stress, which explains the dependence of healing on shear stress. Elastic wave amplitude increases with hold time and varies inversely with shear stress, consistent with fault zone compaction, shear dilatancy and their impact on strength evolution and healing. Fault zone

compaction during shear unloading and reloading operates with contact aging to dictate frictional healing and fault restrengthening following shear failure.

1.2 Introduction:

The seismic cycle on tectonic faults is based on the concept that faults undergo repeated cycles of failure and strength recovery. The processes of strength recovery are referred to as fault healing, and there are a number of studies that document fault healing in nature using seismic and geodetic data (Scholz et al., 1986; Vidale et al., 1994; Marone et al, 1995; Tadokoro and Ando, 2002; Li et al, 2003; Peng et al, 2005; McLaskey et al, 2012). In the shallow crust, where temperatures and effective mean stresses are below about 350°C and 100 MPa, respectively, fault strength and post-seismic strength recovery are dominated by frictional processes. Laboratory experiments document the effects of time and shear displacement on healing and these are quantified in the rate and state dependent friction laws (Dieterich, 1972, 1979; Ruina, 1983; Rice and Ruina, 1983; Marone, 1998a). Additional processes will also be important for the temperatures and fluid conditions at seismogenic depths (e.g., Muhuri et al., 2003; Niemeijer et al, 2002; Tenthorey et al, 2003) but we focus here on the role of shear stress, as one of the important parameters that impacts fault healing.

During an earthquake, fault slip and frictional weakening cause shear stress to drop dynamically, which releases stored elastic energy in the form of seismic waves. To host subsequent events, the fault must regain frictional strength. Understanding fault healing is a central issue in earthquake mechanics as these processes dictate earthquake nucleation, stress drop, recurrence interval, and other source parameters.

Laboratory studies have investigated the frictional properties of natural and synthetic fault materials (e.g., Dieterich 1981; Scholz, 2002). In the laboratory, frictional healing is quantified using slide-hold-slide (SHS) tests (Figure 1), which are a simple analog for the seismic cycle. The initial period of sliding establishes the steady state friction level during fault slip, i.e. an earthquake, and the hold period represents the inter-seismic period, followed by re-shear, which represents another slip event. The analogy is imperfect but the SHS test produces a simple and accurate measurement of the frictional healing associated with a period between slip (failure) events. During the earthquake cycle, the shear stress drops upon failure and the interseismic period may involve additional stress drop, via aseismic afterslip, prior to strength recovery. Previous lab work shows that the shear stress level during SHS tests has an important effect on frictional healing (Nakatani and Mochizuki, 1996; Karner and Marone, 1998; 2001).

The temporal dependence of frictional healing is well documented in the literature. Dieterich (1972) first observed that peak friction following a hold increases logarithmically with hold duration. Since then, time dependent behavior has been observed under a wide range of conditions in numerous materials (e.g., Beeler et al, 1994; Marone, 1998a; Carpenter et al, 2016). The mechanism of time dependent healing involves processes within and at the boundary of contact junctions that constitute the real area of contact between grains and surface asperities (e.g., Dieterich and Kilgore, 1996; Tian et al., 2017). Such changes in contact area and strength can be tracked with ultrasonic velocity and/or amplitude measurements (Pyrak-Nolte et al., 1990; Nagata et al., 2008).

Previous studies show that frictional healing varies inversely with shear stress during the inter-seismic period, τ_{hold}, for simulated fault gouge (Karner and Marone, 1998; 2001). Here, we are interested in understanding more about how shear stress impacts frictional healing and whether

bare rock surfaces also exhibit shear stress dependent healing. An existing study of bare rock surfaces (Nakatani and Mochizuki, 1996) also found that healing varied with shear stress, but they used surfaces that contained significant natural wear material and co-varied the shearing rate with shear stress, making it difficult to determine the dependence of healing on shear stress. They found that steady state friction increased following holds where the shear stress was unloaded, referred to as the 'tightening-up effect'. They observed that the tightening-up effect was proportional to the maximum value of unloaded shear stress and time independent. However, during these experiments a constant stress state was imposed on the sample, allowing some displacement during the holds. This would allow both slip- and time-dependent mechanisms to contribute to frictional restrengthening. In our experiments, sliding is controlled in displacement feedback mode, minimizing slip that occurs during the hold and allowing for a direct comparison with simulated fault gouge experiments.

Despite observations of shear stress dependent healing, the processes that control healing are not well understood and cannot be accounted for in current earthquake models. Therefore, we focus on a systematic investigation of shear stress dependent frictional healing in bare surface and gouge experiments with Westerly granite to better understand the micromechanical processes that control healing. Our observations include particle size analysis to monitor grain size reduction, as well as ultrasonic amplitude measurements to investigate how frictional strength evolves during each part of the shear stress dependent SHS test (i.e. unloading, hold, and reloading). This level of detail is not obtained with traditional mechanical analysis alone.

1.3 Methods:

1.3.1 Experimental Apparatus

Experiments were conducted in a biaxial testing apparatus (Figure 1.1) using the double direct shear configuration (e.g., Karner and Marone, 1998; Anthony and Marone, 2005; Leeman et al., 2016). Normal and shear loads are applied to the sample using independently controlled hydraulic pistons. The pistons can be controlled in displacement or load mode using an electro-hydraulic servo-controlled feedback system. Force and displacement measurements are recorded at 10 kHz and averaged for storage to rates from 100-1000 Hz depending on loading rate. The normal and shear loads are measured using Beryllium-Copper load cells (resolution ±10 N) fixed to the ends of the hydraulic pistons. Load point displacement measurements are recorded using DCDT transducers with 0.1 μm precision.

1.3.2 Sample Geometry and Properties:

We studied three types of simulated fault zones (Table 1). Bare surfaces of Westerly granite (Comolli Granite Inc. in Ashaway, Rhode Island) were prepared by surface grinding samples square and parallel and then roughening with #60 grit silicon carbide to produce a RMS roughness of ~ 100 μm. Experiments were also run with simulated fault gouge composed of crushed Westerly granite and granular quartz (US Silica Co., Foundry sand F-110). Westerly granite gouge was crushed in a ball mill and sieved to pass a 250-mesh sieve, with mean particle size of 70 μm and a range from 38 to 250 μm. F-110 quartz sand has mean particle size of 127 μm and 95% of the grains are in the range 53-212 μm. For all three cases, our laboratory faults have

nominal frictional contact area of 10×10 cm^2. We use a three-block configuration for double direct shear (DDS; Figure 1.1). For bare surface samples, all three blocks are made of Westerly granite. For granular samples, two 3 mm thick layers of gouge (ground granite or quartz) are sandwiched between three grooved steel forcing blocks. Grooves are 0.8 mm deep with 1-mm wavelength and ensure that shear occurs within the layers and not at the layer boundaries (e.g., Anthony and Marone, 2005; Rathbun et al., 2013). Gouge layers are constructed with the same initial layer thickness and using a leveling jig to ensure reproducibility from experiment to experiment (Table 1).

1.3.3 Ultrasonic measurements:

We probed the evolution of friction and elastic properties during our experiments using P-polarized piezoelectric transducers (PZT) with central frequency 500 kHz. The transducers are embedded in steel blocks located next to the side forcing blocks of the DDS configuration. One transducer transmits short pulses (half a sine cycle at 500 kHz) every millisecond throughout the experiment, while the second PZT is used as a receiver. A 14 bit acquisition system records the waveforms at 25 MHz.

1.3.4 Loading Procedure:

Experiments were conducted at constant normal stress, which was typically 25 MPa for granular experiments and 4 MPa for bare surfaces (Table 1). The initial loading procedure of each experiment consisted of a shear load cycle and a series of velocity steps totaling ~10 mm of displacement (Figure 1.2) modeled after the loading sequence of Karner and Marone (2001). During a shear load cycle the shear stress is completely removed from the sample and quickly

reapplied. This technique takes advantage of shear enhanced compaction (Zhu and Wong, 1997) and comminution to attain a steady state grain size distribution (e.g., Marone and Scholz, 1989) and shear fabric (Logan et al., 1992). We sheared samples at 10 µm/s and unloaded at 300 µm/s.

During a SHS test, the sample is first sheared at a constant load point velocity until steady state friction is attained. The vertical piston is then quickly retracted for a specified amount of time to reach the desired shear stress. Note that for conventional slide hold slide tests there is no unloading stage. Next, the load point velocity is set to zero and the hold begins. After the specified hold time, t_h, the sample is reloaded at 10 µm/s. Upon reloading, friction reaches a peak value and decays to a steady-state, which is rarely different from the initial friction value prior to the SHS test. Consistent with previous works, we quantify frictional healing, Δμ, as the difference between peak friction after the hold and the steady state friction prior to the hold (Figure 1.1). Note that we define friction as the ratio of shear and normal stress calculated from the force measurements and sample dimensions.

We use two types of loading procedures for SHS tests. In type I experiments (Figure 1.2 a and d), we conduct 6 SHS tests in succession at the same shear stress value. We follow Karner and Marone (2001) and quantify shear stress during the hold by η, which is the ratio of the shear stress at the start of the hold to the steady-state shear stress value prior to unloading, $\eta = \frac{\tau_{hold}}{\tau_{pre-unload}}$. The two end member cases are (Figure 1.2): conventional SHS tests where η = 1(black) and the zero shear stress case where η ≈ 0 (grey). In type II experiments (Figure 1.2 g), we conduct a sequence of SHS tests with different η values and therefore at different values of shear strain.

1.4 Results:

1.4.1 Steady-state and frictional healing:

Steady state friction values ranged between 0.68-0.71 for Westerly granite gouge (WGG), 0.65-0.78 for Westerly granite bare surfaces (WGBS), and 0.50 and 0.70 for quartz gouge, consistent with prior studies under similar conditions (Dieterich, 1972; Scholz et al., 1972; Tullis and Weeks, 1986; Marone et al., 1990). In some experiments we observe slight strain hardening or strain weakening (Figure 1.2), with a weak tendency for hardening with bare surfaces and weakening with WGG. These trends were generally quite small and we did not study them in detail.

For WGG and quartz gouge we find that the magnitude of frictional healing decreases systematically as a function of increasing η (Figure 1.3), consistent with previous work on granular quartz (Karner and Marone, 1998; 2001). For a 100 second SHS test, $\Delta\mu$ decreases from 0.08 to 0.02 as η increases from 0 to 1 (Figure 1.3). However, for WGBS frictional healing does not vary systematically with η (Figure 1.3). WGBS data show a fair bit of scatter, but the $\Delta\mu$ values for 18 experiments (Table 1), including Type I and Type II runs, vary from 0.02 to 0.06 for the complete range of η from 0 to 1. In a given experiment, most of the scatter for bare surfaces is the result of variations in $\Delta\mu$ with shear displacement (See supplement; Figures A1 and A2). For comparison, we also show data for quartz gouge (Figure 1.3, yellow circles) from Karner and Marone (2001). Note the similarity between these data and our data for WGG. Frictional healing for gouge varies systematically with the shear stress during aging but not for bare granite surfaces.

Our bare surface experiments were performed at normal stress of 4 MPa, whereas most of our data for gouge are for runs at 25 MPa. We did a suite of tests to study the affect of normal stress on healing of quartz gouge as a function of η (Figure 1.4). These data show that for this range of normal stresses $\Delta\mu$ is independent of normal stress. Figure 1.4 includes data from Type I and Type II experiments. Frictional healing varies somewhat with shear strain, in a given experiment, but this is relatively minor compared to the affect of shear stress during the hold period. Frictional healing for gouge is significantly larger when the applied shear stress is lower during the hold period (Figure 1.4).

1.4.2 Layer thickness evolution and dilatancy:

For granular materials one expects that shear strength will vary as a function of particle size distribution, particle packing, porosity, and the degree of shear localization. To evaluate these effects we analyzed the evolution of fault zone thickness during SHS tests (Figure 1.5). In gouge experiments, the fault zone width is given by the gouge layer thickness. In bare surface experiments, the fault zone width is zero initially and increases with wear and gouge formation as asperities break and become part of a gouge layer. We use vernier calipers to measure initial fault zone thickness under normal load prior to shear in each experiment. These measurements are accurate to ±50 μm. We continue to monitor changes in layer thickness throughout experiments via the DCDTs (Figure 1.1), with a precision of ±0.1 μm.

Our experiments with WGG and quartz show that layers densify upon initial shear and thin steadily as the fault zone undergoes geometric spreading (e.g., Scott et al., 1994) in simple shear (Figure 1.5). WGBS faults thin initially and then increase in thickness with shear (Figure 1.5).

Note that the gouge formation rate is quite low for WGBS. The fault zone increases in thickness by about 15 μm over 40 mm of shear (Figure 1.5a).

We quantify three thickness parameters during SHS tests: unload compaction, ΔT_u, hold compaction, ΔT_h, and reload dilatancy, ΔT_r, (Figure 1.5b). In a SHS test, the fault zone thins as the shear stress is unloaded and continues to gradually decrease throughout the hold period (Figure 1.5b). Upon reloading the layer thickness increases as the layer dilates and we reinitiate shear.

Layer thickness variations plotted as a function of normalized shear stress are shown in Figure 1.6. We observe greater compaction and dilatancy in granular experiments compared to bare surface experiments. Almost no change in layer thickness is observed during the hold period for bare surface experiments. For gouge experiments, unload compaction and reload dilatancy increase as η decreases (Figure 1.6). During a complete SHS test, gouge samples undergo net compaction by an amount that scales inversely with η. In WGBS there is very little net change in layer thickness. The compaction that occurs during unloading is typically offset by the reload dilatancy (Figure 1.6).

The dilatancy rate plays an important role in determining frictional strength. We measure dilatancy rate with shear strain as the volume strain θ per shear strain γ. For the DDS arrangement, $d\theta/d\gamma$ can be calculated from the frictional contact area A and the change in layer thickness dh per unit of shear displacement dx: $d\theta/d\gamma = (dV/V)/(dx/h)$, where V is volume and x is shear displacement. That is, to first order, $dV = dh\,A$, $V = h\,A$, $\gamma = dx/h$; and, thus for constant A, $dV/V = dh/h$ and $d\theta/d\gamma = dh/dx$. We calculate $d\theta/d\gamma$ using a running average slope with a variable window size appropriate for the sampling rate and shear displacement rate (Table 1).

Fault zone dilatancy during shear requires work against the mean stress and, therefore, contributes to the measured value of friction (Bishop 1954; Edmond and Paterson, 1972; Marone et al., 1990). Dilatancy rates in WGG increased from 0.02 to 0.09 as η decreased from 1 to 0 (Figure 7). In WGBS, dilatancy rates increased from 0.05 to 0.3 as η decreased from 1 to 0. The peak dilatancy rate is highest in the bare surface experiments, which is consistent with the smaller shear displacement required in bare surface experiments to overcome peak friction and reinitiate sliding. So while bare surface experiments dilate faster, gouge experiments dilate at a lower rate but for a longer period of time (typically 1-2 seconds for WGG and <1 s for WGBS) and this period increases as η decreases in WGG.

1.4.3 Particle Size Analysis:

We conducted particle size analysis (PSA) to evaluate the possible role of grinding and comminution on healing and its variation with shear strain. PSA was done for Westerly granite gouge layers sheared in Type I experiments and a control sample of undeformed WGG (Figure 1.8). As evidenced by comparison with the control sample, gouge particles break and the mean grain size decreases for all of our tests (Figure 1.8). However, the particle size distribution does not change systematically as a function of η (Figure 1.8a-f).

To investigate more subtle changes in particle size distribution we consider the D10, D50, and D90 values (Figure 1.8g). These values are the particle size intercepts of 10%, 50%, and 90% of cumulative mass (i.e. a D10 value indicates the particle size at which 10% of the total mass of particles is smaller than that size) and are a common metric used to describe particle size distributions. The D10, D50, and D90 values appear relatively constant for all shear stresses. This

suggests that grain size reduction is not the cause of the observed shear stress dependent frictional healing or that changes in grain size are not captured when analyzing the bulk particle size distributions.

1.4.3 Ultrasonic amplitude:

We quantify the temporal evolution of acoustic amplitude during SHS tests. Our approach uses the root-mean square of the wave amplitude. RMS amplitude evolution for two representative WGG and WGBS experiments are shown in Figure 1.9. Amplitude generally increases rapidly as the sample is unloaded, due to layer compaction, and it continues to increase at a gradual rate during the hold period (Figure 1.9). The rate of amplitude increase varies systematically with shear stress during the hold period (Figure 1.9). Following the hold, the transmitted wave amplitude decreases as shear stress increases and the gouge layer dilates during reshear. The amplitude increases during steady-state shear, consistent with layer thinning and densification. Future work will focus on a full description of elastic wave properties. Here we consider only relative changes in amplitude during individual SHS tests.

The characteristics of an individual SHS test in Westerly granite gouge for which $\eta = 0.42$ are shown in Figure 1.10. Here we define three parameters to characterize the amplitude changes: (i) A^U, the change in amplitude during unloading, (ii) A^H, the change in amplitude during the hold, and (iii) A^R, the change in amplitude from the onset of reloading to peak friction (Figure 1.10). Note that these amplitude changes correspond directly to the layer thickness changes discussed above (Figure 1.5). Amplitude increases as the sample compacts and decreases as the layer dilates upon reshearing.

To measure elastic wave amplitudes during SHS tests, we record time relative to the initiation of shear unloading, prior to the hold (Figure 1.10). Amplitude changes are referenced to the amplitude at this point. As the shear stress is removed, the amplitude increases by about 600 amplitude units (AU), i.e. A^U ~600 AU. The amplitude continues to gradually increase during the hold period as the sample continues to compact and we calculate A^H ~200 AU. In this case, where $\eta = 0.42$ processes during unloading account for 75% of the total observed amplitude increase. As the sample is resheared the amplitude decreases and A^R is measured ~600 AU. Combing these three changes results in a net amplitude change of 200 AU during the SHS test from the start of unloading to peak frictional strength upon reloading.

We observe that in WGG the overall change in RMS amplitude increases as η decreases. The amplitude parameters A^U, A^H and A^R (defined in Figure 1.10) are shown for WGG and WGBS in Figure 1.12. Combining the effects of these three parameters gives the total change in RMS amplitude during the SHS test (Figure 1.12d). In WGG, during the unloading and reloading phases, the magnitude of amplitude change varies systematically with η and A^R is typically slightly greater than A^U. However, SHS tests at all η show similar changes during the hold period. Therefore, the relative contributions from processes during both unloading and the hold vary with η. There is notable scatter in the WGG amplitude changes, especially at low η, that likely results from displacement/strain effects. For the three experiments of Figure 1.12, the SHS were conducted in different orders i.e. highest to lowest η, lowest to highest η, and intermixed. For WGBS, the total change in acoustic amplitude during a SHS is very small. The changes in amplitude during unloading and reloading are larger for intermediate η. For a given SHS A^U and A^R scale with one another such that the net change in amplitude is small.

We observed that the rate of amplitude increase varies slightly with shear stress during the hold period (Figure 1.13). The increase in amplitude with the logarithm of time is non-linear. In WGBS, amplitude increases most rapidly for intermediate stress values (Figure 1.13a). For WGG, there does not appear to be a systematic variation with η (Figure 1.13b). Note that while the rates of amplitude change during the hold vary slightly, the difference in amplitude change between the highest and lowest rates is approximately 100 amplitude units for both WGBS and WGG which is only a fraction of the overall amplitude change during the SHS test.

We also considered amplitude variations as a function of shear stress for a WGG experiment (Figure 1.14). As the shear stress is unloaded to the desired η value, the RMS amplitude increases. Then the hold begins, during which the shear stress is relatively constant and the RMS amplitude continues to increase. After 100s of holding, the sample is reloaded and the RMS amplitude decreases until peak friction is reached. This again highlights the net increase in amplitude for a SHS test. The general shape of the amplitude curve is the same for each SHS although some minor differences were noted and will be explored in future work.

1.5 Discussion:

Our data show that frictional aging is strongly dependent on the shear stress during hold periods for granular fault gouge but not for bare rock surfaces in contact. Our results are consistent with previous work on quartz gouge but differ from an existing study of bare surfaces conducted under similar conditions. Layer thickness measurements suggest that net compaction during SHS tests contributes to frictional strength of gouge and accounts for the shear stress dependence of healing. We observe that changes in acoustic amplitude during SHS tests coincide with changes in layer thickness and frictional strength.

1.5.1 Healing in Westerly granite gouge:

In granular material, inter-particle interactions govern frictional restrengthening, which occurs at contact junctions and via many-particle interactions in force chains and their supporting structures of grain networks. Our data demonstrate that these processes vary systematically with the applied shear stress. Analysis of particle size distributions show that similar grain size reduction occurs during experiments at all shear stress values (Figure 1.8). Therefore, particle size is unlikely to be a controlling factor. Nonetheless, it is worth noting that our particle size measurements were for the bulk material recovered from experiment. We cannot rule out the possibility that localized particle size reduction, or changes in size distribution, occurred within shear bands, as demonstrated in previous work (Marone and Scholz, 1989) and had an impact on frictional healing. Investigating such effects would be a useful aim for future work.

Our observation of increasing compaction and reload dilatancy for lower shear stresses during aging indicates higher packing density, which would result in greater frictional strength. Our data are consistent with concepts of critical state soil mechanics, such that the granular porosity reaches a critical value for steady state frictional shear. If the layer density has increased, as we suspect happens due to particle rearrangement during unloading, then more work is required to initiate shearing. As a result, the sample can sustain higher shear stresses and reaches higher peak friction values upon reloading. As more stress is unloaded and η decreases the layer porosity deviates further from the steady-state porosity required for shearing. This is one possible explanation of our observation of higher peak friction and larger $\Delta\mu$ values for lower η.

From acoustic amplitude measurements, we observed that the total change in amplitude during a SHS tests (Figure 1.12d) correlates well with measured frictional healing (Figure 1.3). This suggests that processes that occur during loading, unloading, and the hold period all contribute to the overall frictional strength. Specifically, in gouge we note that the amplitude change during the hold is relatively constant for all shear stresses (Figure 1.12b) but the corresponding frictional healing values vary suggesting the unloading and reloading conditions play a significant role in determining overall peak frictional strength.

Here we propose a possible explanation of the granular interactions that occur during each of these stages under different stress conditions (Figure 1.15a). During unloading, compaction increases packing density, which increases frictional strength. Therefore, samples that are unloaded to lower η values have larger contributions to frictional strength from compaction. During the hold period, frictional strength increases via contact area growth in two ways: 1) growth of existing contacts and 2) increase in particle coordination number, due to particle motion and granular rearrangement. At high η values, we suspect that frictional healing occurs primarily from growth of existing contacts because high inter-granular stresses prevent particle rearrangement. At low η values, growth of existing contacts is expected to be lower because the mean stress is lower; however, these lower stresses also allow greater particle rearrangement. At intermediate stresses, there may be contributions from both increasing the size of existing contacts and the development of new contacts via particle rearrangement. The stresses may be sufficiently high to allow contact area growth and but low enough to allow some particle rearrangement. A combination of these two processes under different stress conditions appears to produce similar overall changes in layer thickness and acoustic amplitude during the hold period (Figures 1.12 and 1.13). Upon reloading, the layer dilates until it overcomes peak frictional strength and reaches steady-state porosity. The

amount of dilation required is a product of the compaction that occurred during the unloading and hold stages of the SHS test.

1.5.2 Healing of bare Westerly granite surfaces:

Our experiments with bare rock surfaces show that shear stress has a negligible affect on frictional healing. We observe wear and gouge development during these experiments, but the wear rates are low and the wear products are only dust sized, with estimated grain size of < 1 μm. The accumulated gouge in our experiments is less than a few microns thick and has a patchy rather than continuous habit. Thus, we posit that frictional restrengthening results primarily from changes in the number and strength of contact junctions, rather than changes in fault zone porosity (Figure 1.15b). Our observations differ from those reported by Nakatani and Mochizuki (1996), who reported that peak friction and frictional healing increased with applied shear stress during aging. They also studied granite, however the rock name was not given. Their procedure involved rapid changes in the loading rate, which has an independent affect on frictional healing (Marone, 1998b), and thus it is difficult to evaluate their results. Moreover, they report that steady-state sliding friction exhibits permanent changes after SHS tests, which is hard to envision. Our data are consistent with the idea of a critical slip distance; such that frictional aging is a transient phenomena that is reset after a shear offset sufficient to rejuvenate asperity contacts.

We observe variations in frictional healing as a function of shear for our bare surface runs. We suspect that these are due to variations in roughness and the effect of wear, however we did not study them in detail.

1.6 Conclusions:

Our investigation of Westerly granite at conditions relevant to the Earth's crust reveals that shear stress dependent restrengthening processes in bare surfaces and synthetic gouge are dominated by different mechanisms. Healing of gouge shows a strong negative dependence on shear stress and healing of bare surfaces is not primarily controlled by shear stress. In bare surfaces, healing is dominated by contact evolution during the hold period. Whereas the shear stress dependence of healing in gouge is strongly affected by granular processes, including compaction, dilatancy, and changes in packing density. Frictional healing and fault strengthening is controlled by a combination of fault zone compaction during shear unloading and reloading and contact aging. For natural faults, our data demonstrate that shear stress can play a key role in the evolution of frictional strength and fault healing. We also show that acoustic amplitude provides a useful tool for capturing continuous measurement of frictional strength that are undetected by traditional mechanical measurements. Elastic wave amplitude increases throughout the hold period and varies inversely with shear stress, consistent with our mechanical observations of fault zone compaction and shear dilatancy.

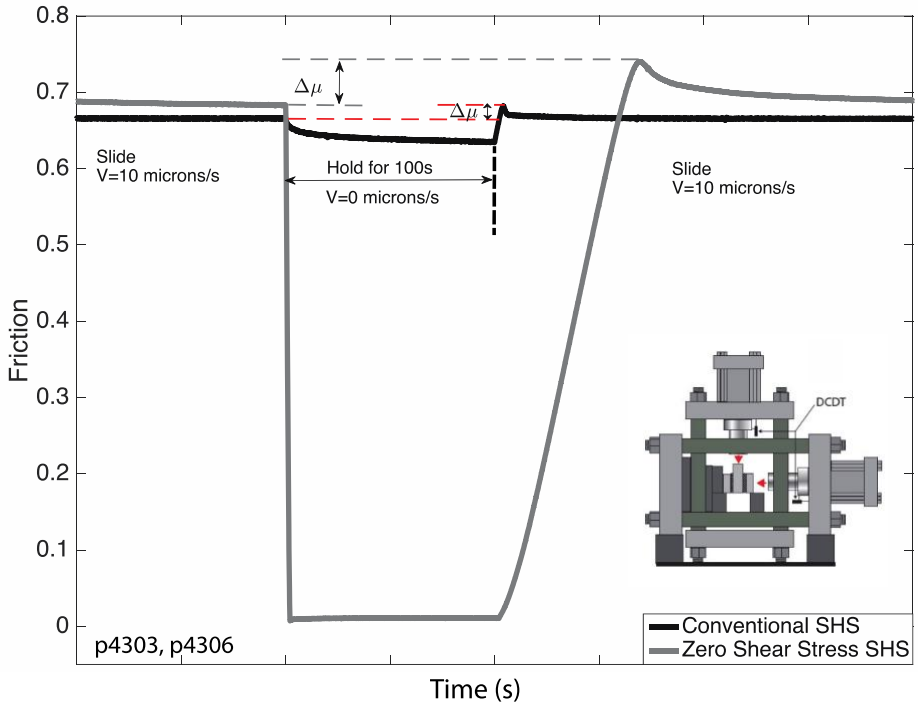

Figure 1.1:
Overview of frictional healing measurements from slide-hold-slide (SHS) tests conducted in a biaxial deformation apparatus (inset from Scuderi, 2014). Shown is the frictional evolution before, during, and after a 100-second hold period. Two shear stress end member cases are shown, the conventional case where the hold begins at the steady state shear stress level (black) and the zero shear stress case where the shear stress is completely removed prior to the hold (gray). Frictional healing, Δμ, is quantified by the difference between peak frictional strength upon reloading the sample after the hold and steady state friction prior to the hold.

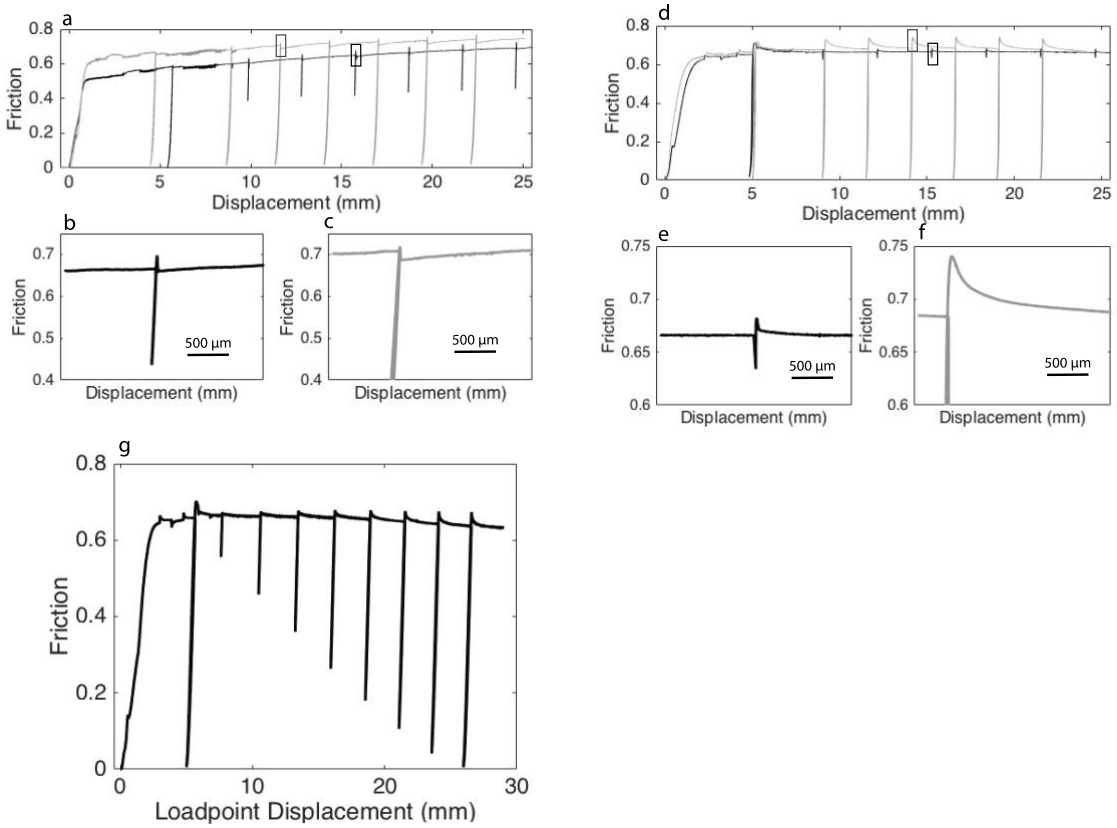

Figure 1.2:
Friction versus loadpoint displacement during Westerly granite bare surface (WGBS) (a-c) and Westerly granite gouge (WGG) (d-f) experiments at two values of η, black (high) and gray (low). The black and gray boxes in (a) denote the areas shown in subplots (b) and (c), respectively which highlight frictional behavior after SHS tests at different η values. In WGBS, peak friction following SHS tests is similar at high (b) and low (c) η values and decays quickly back to a steady-state value. In WGG, peak friction after a SHS test is greater at low η (f) than high eta (e) and friction decays to steady state more slowly for lower η. Shown are two different loading histories, type I (a, d) and type II (g).

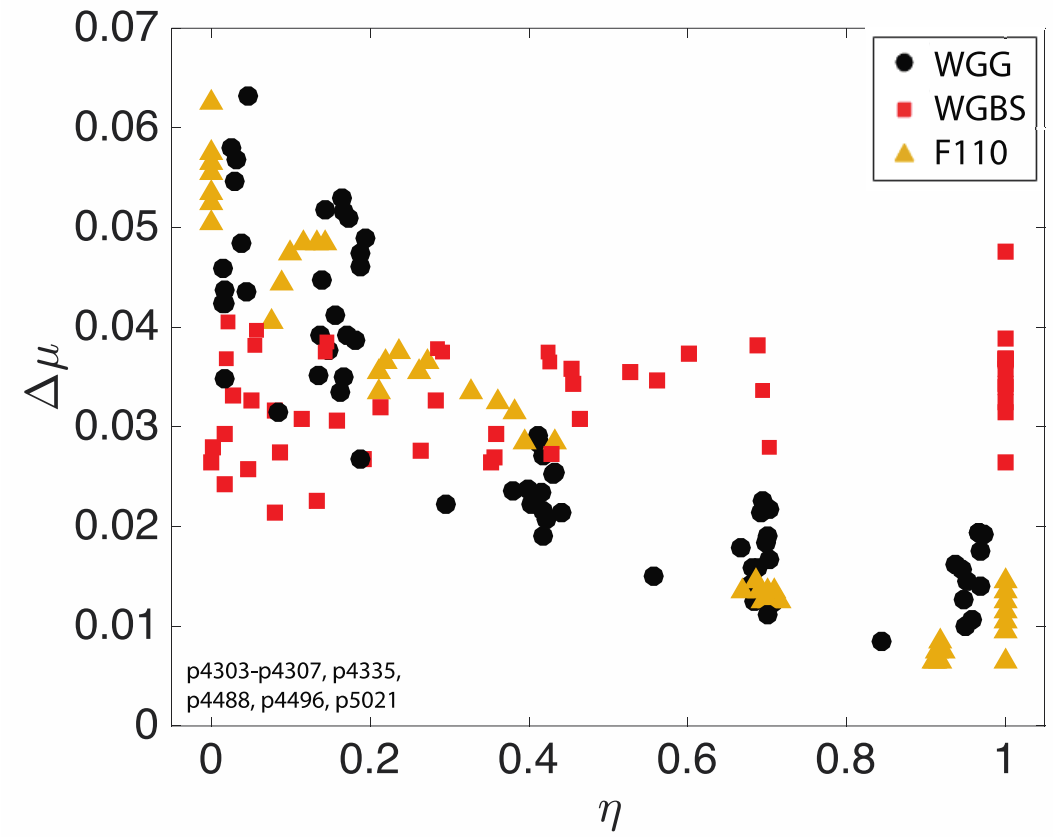

Figure 1.3:
Frictional healing versus normalized shear stress η for F110 (yellow triangles from Karner and Marone, 2001), WGG (black circles), and WGBS (red squares). In granular material, frictional healing shows a clear dependence on η. For bare surfaces, frictional healing does not vary systematically with shear stress.

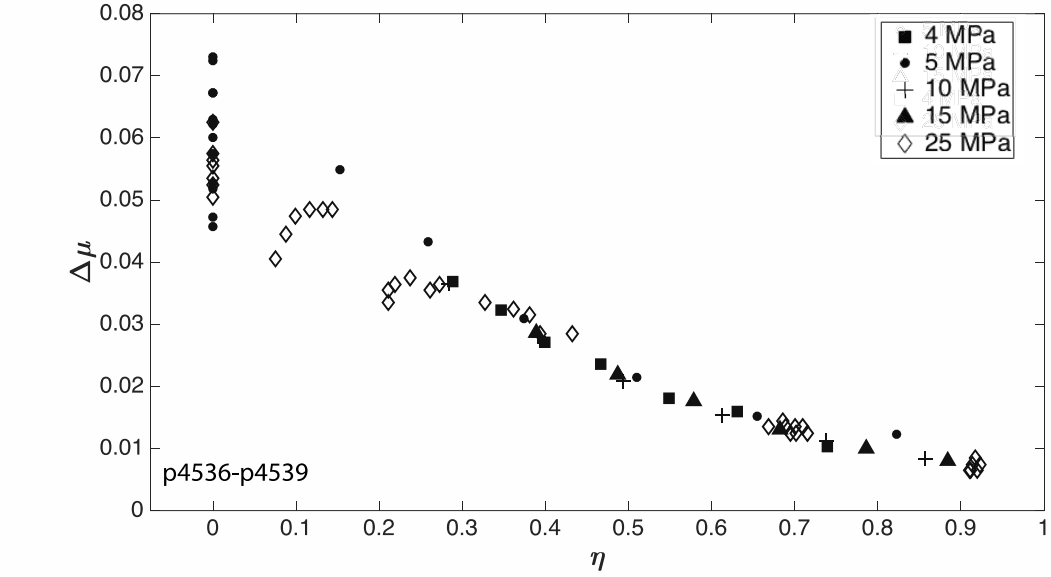

Figure 1.4:
Frictional healing versus η from experiments conducted on quartz powder (F110) at different normal stresses. Here we highlight that F110 exhibits shear stress dependent frictional healing at all normal stresses included in this study (4-25 MPa). 25 MPa data are from experiments of Karner and Marone (2001).

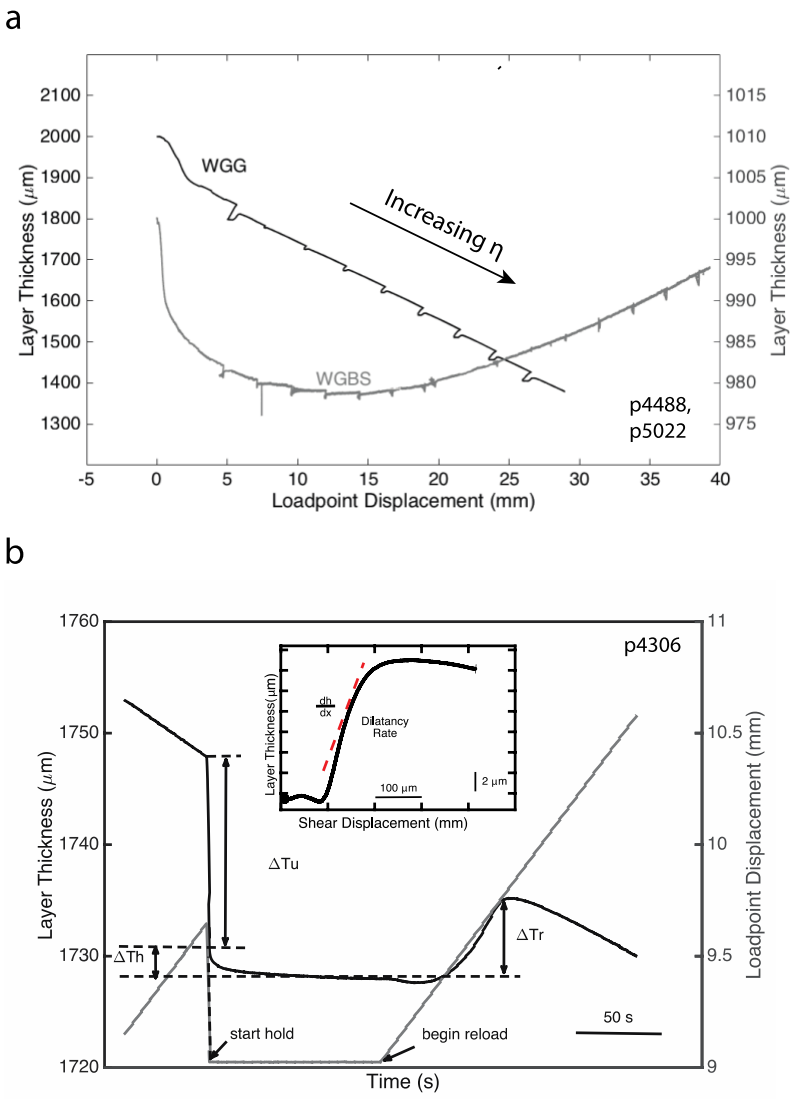

Figure 1.5:
(a) Evolution of layer thickness during type II experiments in WGG and WGBS.
(b) Evolution of layer thickness (black) and shear displacement (gray) with time during a single SHS test. Prior to the hold, the layer compacts as the shear stress is unloaded (ΔTu). The layer continues to compact during the hold period (ΔTh). After the hold, the sample dilates as it is sheared (ΔTr). The total change in layer thickness during the SHS (Δh) is given by ΔTu+ ΔTh-ΔTr. Inset shows the change in layer thickness as a function of vertical displacement during the reloading phase. From this plot, the dilatancy rate dh/dx is calculated using a running average slope. B**:** Zoomed view of fracture process in Berea sandstone experiment. Shear stress (black) and permeability (blue). Permeability decrease during shear loading and shear failure. Direction of increasing normal displacement represents dilation.

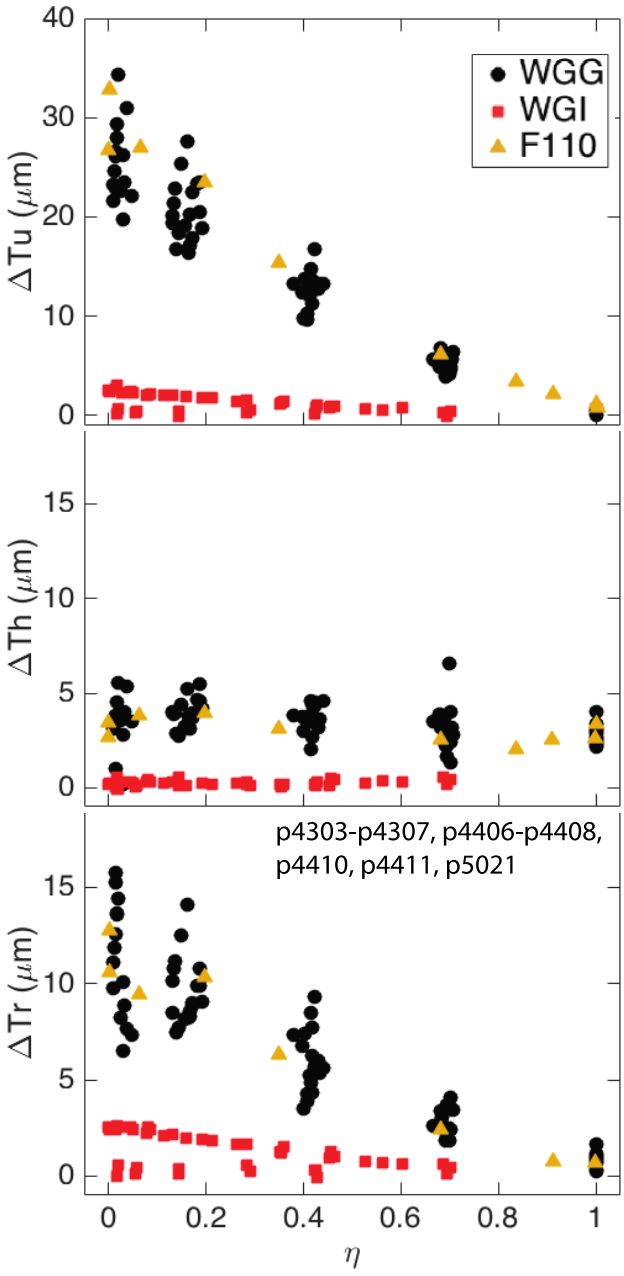

Figure 1.6:
(a) Unload compaction (ΔTu), (b) hold compaction (ΔTh), and (c) reload dilatancy (ΔTr) versus η for WGG(black), WGBS(red) and F110 (yellow). Unload compaction and reload dilatancy are higher for granular materials compared to bare surfaces. Note that for gouge, ΔTu and ΔTr vary systematically with shear stress.

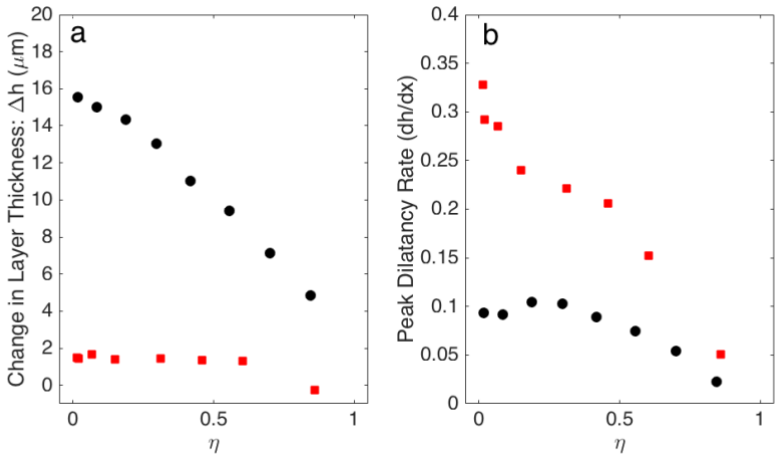

Figure 1.7:
Total change in layer thickness (left) and peak dilatancy rate (right) versus normalized shear stress for WGG (black) and WGBS (red).

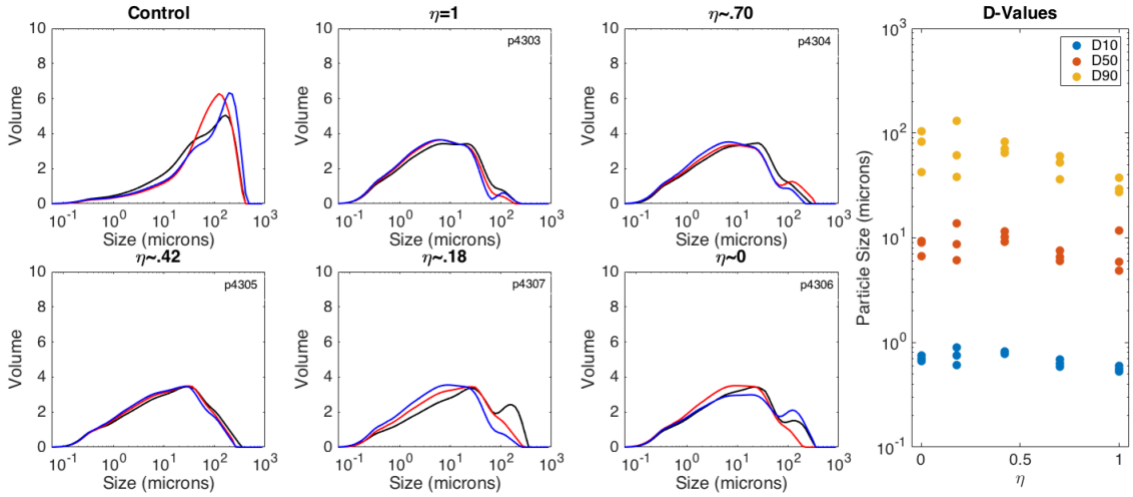

Figure 1.8:
Left: particle size distributions (PSD) for 6 Westerly granite gouge samples. The black, blue, and red lines are 3 separate measurements of PSD using material from a single sample. The control sample is the undeformed gouge and the remaining 5 samples were all recovered after Type I experiments. Each experiment was conducted at a different shear stress. Right: D10, D50, and D90 values as a function of normalized shear stress. D-values are a common metric used to describe particle size distributions. D values are the intercepts of 10%, 50%, and 90% of cumulative mass. We observe the bulk PSD is relatively consistent for experiments with SHS conducted at different η values.

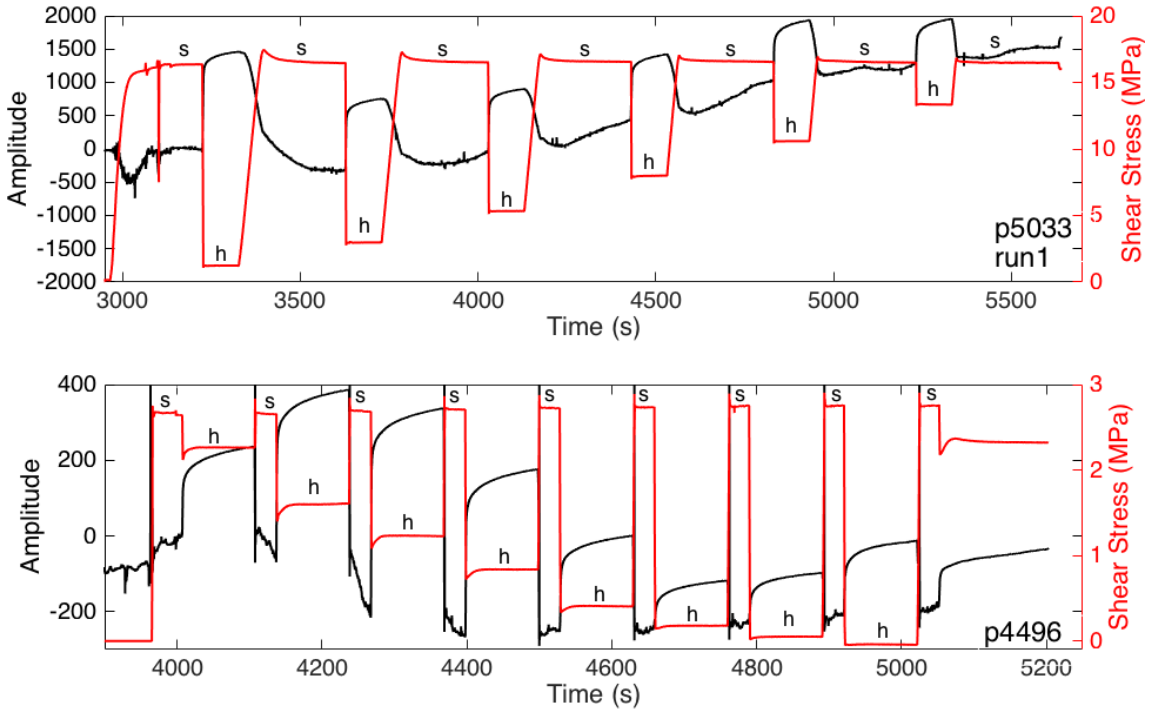

Figure 1.9:
Root mean square amplitude (black, left axis) and Shear Stress (red, right axis) versus time for SHS experiments with WGG (top) and WGBS (bottom). Slide (s) and hold (h) sections are annotated.

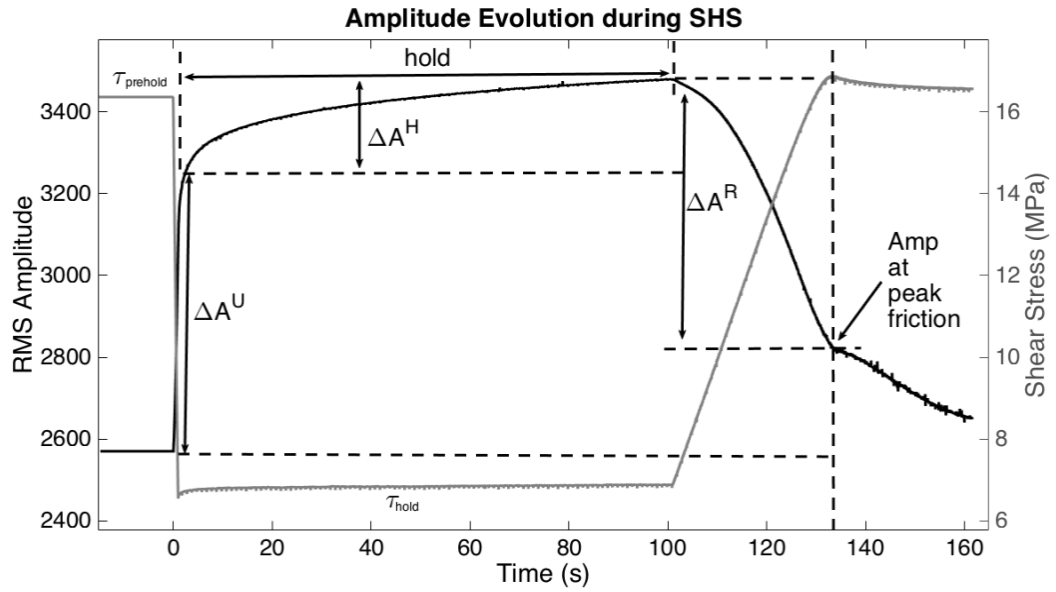

Figure 1.10:
Acoustic amplitude evolution during a SHS test in Westerly granite gouge in which η =0.42 . The amplitude here is defined as the root-mean square (RMS) average of the amplitude of the acoustic wave. Amplitude is shown in black on the left axis and the shear stress is shown in gray on the right axis. Amplitude increases dramatically during unloading and then at a more gradual rate during the hold period. Upon reloading, amplitude decreases at a rate than increases with time until just prior to the peak strength when the second derivative of amplitude vs. time passes through zero. The rate of amplitude decrease changes markedly at the peak strength. Defined are three amplitude measurements, AU, change in amplitude during unloading, AH, the change in amplitude during the hold, and AR, the change in amplitude from the onset of reloading to peak friction.

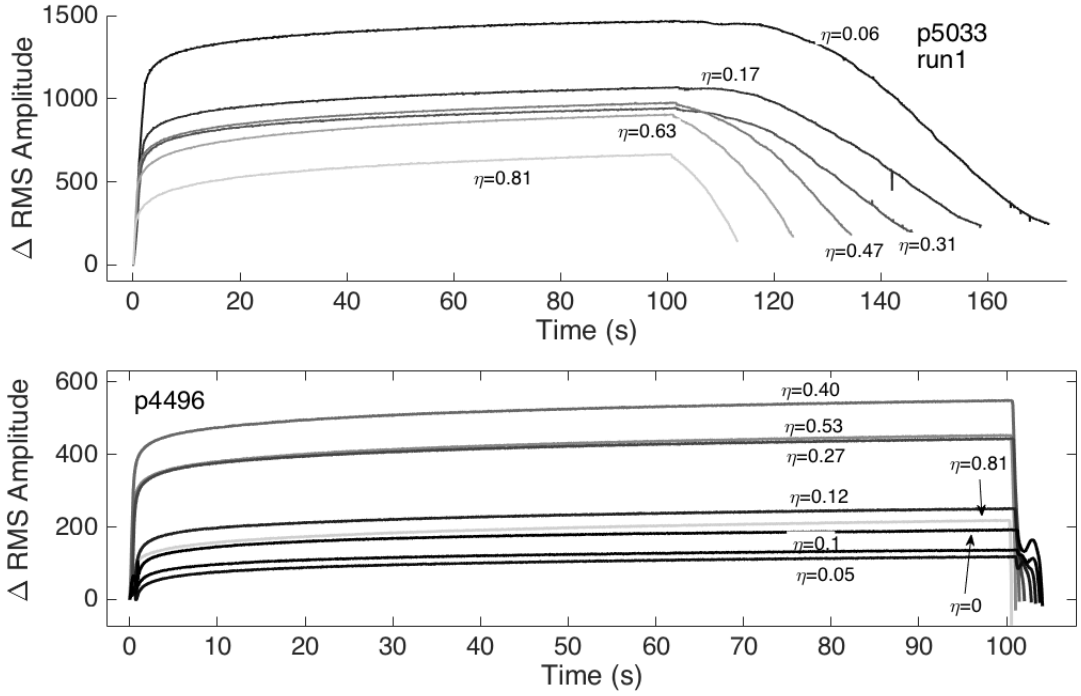

Figure 1.11:
Change in RMS Amplitude vs time for 6 SHS tests in WGG (top) and 8 SHS tests in WGBS (bottom). Time=0 signifies the beginning of unloading and the last time shown corresponds to peak friction after reloading (see Fig 10). The amplitude changes are referenced to the amplitude immediately prior to unloading. Darker lines indicate that more stress was removed prior to the hold (i.e. lower η SHS tests). The RMS amplitude during each SHS exhibits the same general behavior (see Figure 10 for more detailed explanation). We observe that in WGG the overall change in RMS amplitude from the onset of unloading to peak friction upon reloading increases as η decreases. Whereas for WGBS, the total change in acoustic amplitude during a SHS is small.

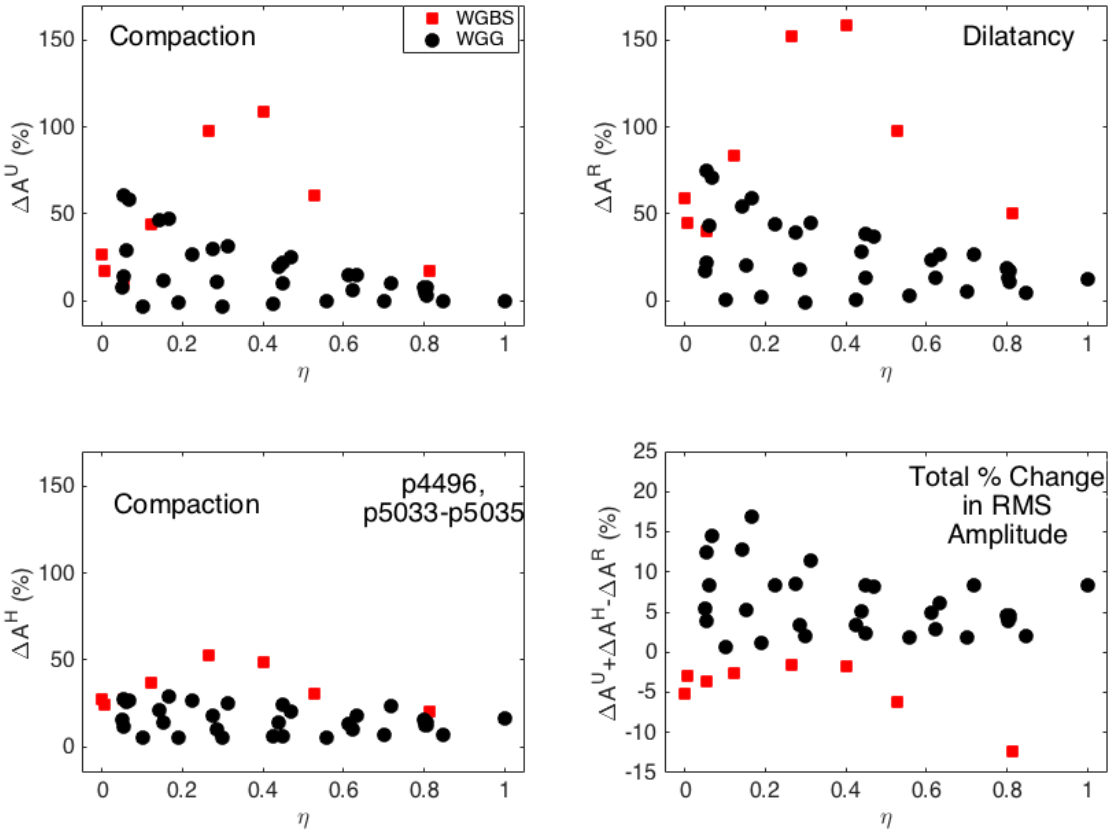

Figure 1.12:
Changes in percent amplitude during the unload (AU), hold (AH) , reload (AR) portions of SHS tests are shown for WGG (black) and WGBS (red) , see Fig. 10. The amplitude prior to unloading is used as the reference amplitude. Percent changes in amplitude during unloading, holding, and reloading for WGBS are generally larger than for WGG and independent of η. For WGG, AU and AR scale with η. The scatter for WGG results from displacement effects. The total change in amplitude (AU +AH -AR) (bottom right) is small for WGBS and ranges from 0 to 20 % for WGG with the highest changes occurring at low η.

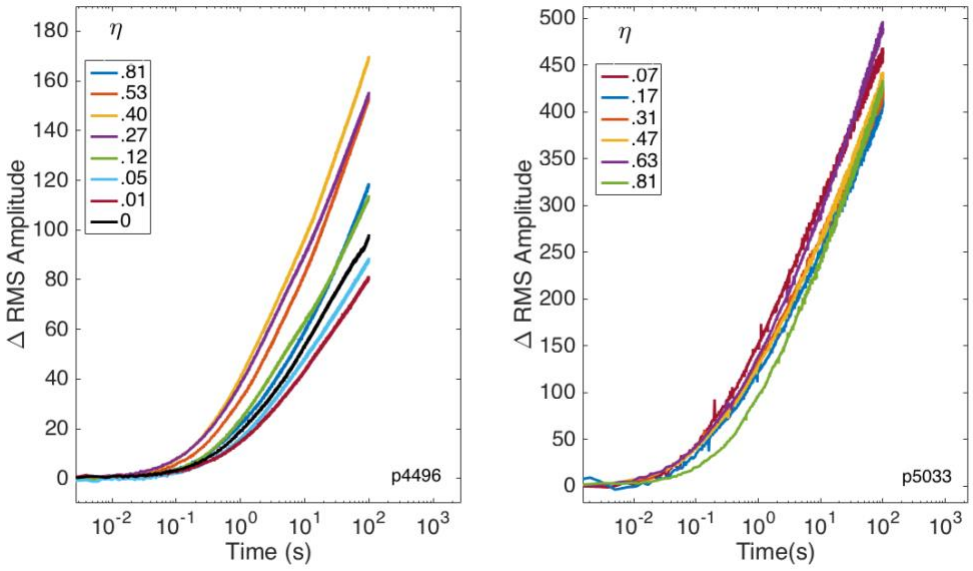

Figure 1.13:
RMS amplitude versus log time for (a) WGBS experiment p4496 and (b) WGG experiment p5033. Note that the time rate change of amplitude increase is highest for intermediate values of shear stress in WGBS whereas it does not vary systematically with shear stress for gouge.

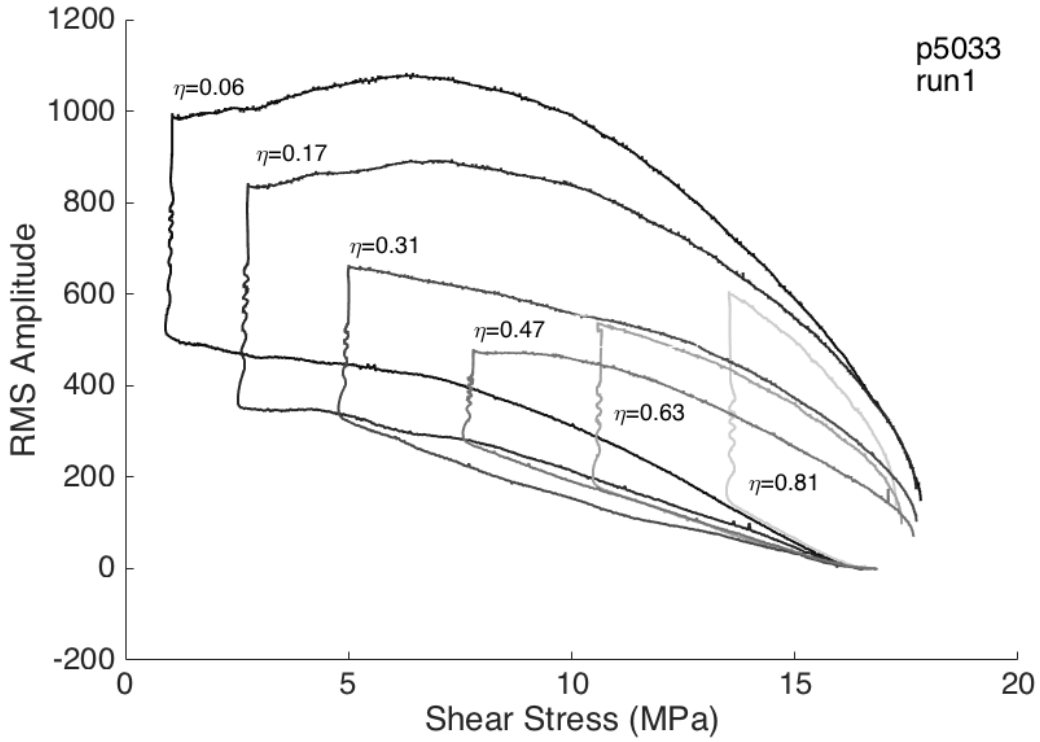

Figure 1.14:
Root-mean-square amplitude versus shear stress during 6 SHS tests from experiment p5033 (WGG). During each SHS test, a reference RMS amplitude (which varies per SHS test) is recorded at the initial steady state shear stress value (16-16.5 MPa). As the shear stress is unloaded to the desired shear stress, the RMS amplitude increases. Then the hold begins, during which the shear stress is relatively constant and the RMS amplitude continues to increase. After 100s of holding, the sample is reloaded and the RMS amplitude decreases until peak friction is reached.

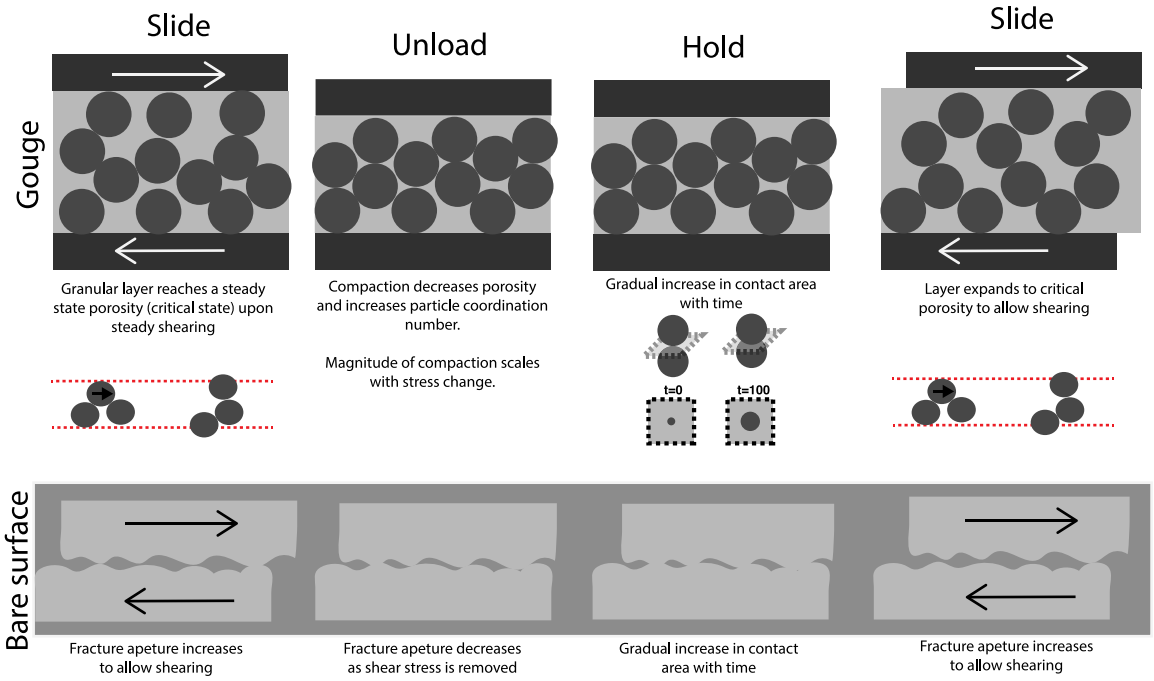

Figure 1.15:
Synoptic model of the micromechanical processes occurring during SHS tests with gouge (top row) and bare surfaces (bottom row).

Experiment #	Normal Stress (MPa)	η	Hold time (s)
Material: F110			
p4096	2	varied	100
p4265	25	varied	100
p4288	25	0	10/100
p4289	25	0	10/100
p4290	4	0	10/100
p4291	10	0	10/100
p4292	4	0	10/100
p4293	4	0	10/100
p4436	25	0	100
p4437	25	0	100
p4438	25	0	100
p4439	25	0	100
p4517	4	varied	100
p4536	5	varied	100
p4537	10	varied	100
p4538	20	varied	100
p4539	15	varied	100
p4707	5	0	100
p4717	5	0	100

Table 1.1:
Experiment list and key parameters from granular quartz (F110) experiments.

Experiment #	Normal Stress (MPa)	η	Hold time (s)
Material: Westerly Granite Gouge			
p4297	25	0	10/100
p4298	25	0	10/100
p4299	25	0	10/100
p4303	25	1	100
p4304	25	0.7	100
p4305	25	0.41	100
p4306	25	0.18	100
p4307	25	0.02	100
p4360	25	0	100
p4371	25	0	varied
p4372	25	0	varied
p4375	25	0	varied
p4376	25	0	varied
p4388	25	1	100
p4389	25	0.68	100
p4391	25	0.4	100
p4392	25	0.16	100
p4393	25	0.02	100
p4406	25	1	100
p4407	25	0.7	100
p4408	25	0.42	100
p4410	25	0.16	100
p4411	25	0.02	100
p4423	25	0	varied
p4424	25	0	varied
p4425	25	0	varied
p4442	25	0	varied
p4448	25	0	varied
p4453	25	0	varied
p4470	25	0	varied
p4488	25	varied	100
p4489	25	varied	100
p4490	25	varied	100
p4563	25	0.42	varied
p4564	25	0.36	varied
p4565	25	0.3	varied
p4566	25	0.19	varied
p4567	25	0	varied
p4568	25	0.42	varied
p5033	25	varied	100
p5034	25	varied	100
p5035	25	varied	100

Table 1.2:
Experiment list and key parameters from Westerly granite gouge experiments.

Experiment #	Normal Stress (MPa)	η	Hold time (s)
Material: Westerly Granite Bare Surfaces			
p4325	4	0.57	100
p4326	4	1	100
p4332	4	0.32	100
p4333	4	0.13	100
p4335	4	1	100
p4367	4	0.57	100
p4369	4	0.57	100
p4440	4	0	100
p4441	4	0.73	100
p4496	4	varied	100
p4544	4	0	100
p4545	4	0	varied
p4546	4	1	varied
p4547	4	0	varied
p4548	4	0.48	varied
p4549	4	0.25	varied
p5021	4	varied	100
p5022	4	varied	100

Table 1.3:
Experiment list and key parameters from Westerly granite bare surface experiments.

Chapter 2

Influence of Phyllosilicates on Shear Stress Dependent Healing

2.1 Abstract:

Frictional healing occurs during the seismic cycle as faults gradually regain strength after failure. Previous laboratory studies indicate that frictional healing in granular materials varies as a function of shear stress. These studies have primarily been conducted on quartz and feldspar rich materials that exhibit high frictional strength and pronounced rates of restrengthening.

However, many faults, including those at subduction zones, are known to be rich in phyllosilicate minerals that have lower frictional strength and exhibit less frictional healing than high friction materials. Here, we focus on the shear stress dependence of frictional healing in materials with lower frictional strength. Our primary goal is to determine if frictional healing in phyllosilicate rich gouges exhibits a similar shear stress dependence as high friction granular materials. We investigate the deformation mechanisms responsible for frictional restrengthening, at high and low shear stress, using mechanical data and ultrasonic amplitude measurements.

Biaxial deformation experiments were conducted on a series of synthetic and natural gouges. The normal stress was held constant at 25 MPa and we performed a series of slide-hold-slide tests at a range of normalized shear stress values. We observe steady-state frictional properties consistent with previous work. Frictional healing in synthetic mixtures of quartz and smectite transitions from the strong negative shear stress dependence observed in quartz to a positive dependence for mixtures with 50 % smectite. For mixtures with > 70 % smectite no healing is observed.

2.2. Introduction:

The seismic cycle on tectonic faults is based on the concept that faults undergo repeated cycles of failure and strength recovery. Fault strength evolution during these cycles impacts fault stability, earthquake nucleation, stress drop, and recurrence interval which ultimately control the mode of failure as well as frequency and size of earthquakes. The processes of strength recovery are referred to as fault healing, and there are a number of studies that document fault healing in nature using seismic and geodetic data (Scholz et al., 1986; Vidale et al., 1994; Marone et al, 1995; Tadokoro and Ando, 2002; Li et al, 2003; Peng et al, 2005; McLaskey et al, 2012). In the shallow crust, where temperatures and effective mean stresses are below about 350°C and 100 MPa, respectively, fault strength and post-seismic strength recovery are dominated by frictional processes.

Laboratory studies have been used to systematically investigate the frictional properties of natural and simulated fault materials and document the effects of time and shear displacement on healing and these are quantified in the rate and state dependent friction laws (Dieterich, 1972, 1979; Ruina, 1983; Rice and Ruina, 1983; Marone, 1998a). Laboratory slide-hold-slide (SHS) tests are commonly used as a simple analog for the seismic cycle. The sliding represents slip along the fault, i.e. an earthquake and the hold time represents the inter-seismic period, during which laboratory faults creep and restrengthen akin to postseismic slip and fault healing. Frictional healing, $\Delta\mu$, is quantified during SHS tests by the change in friction from the steady state sliding value to the peak value upon reloading (Figure 2.1). Previous studies have documented the increase in $\Delta\mu$ with the logarithm of hold time and related these changes to the stress drop recurrence interval relationship observed on faults with reoccurring slip events (Marone et al, 1995; Peng et al, 2005).

In addition, the need to understand how mineral composition of gouges influences fault properties is highlighted by the many recent studies focused on how mineralogy effects fault strength (Giorgetti et al, 2015; Behensen and Faulkner, 2012; Tembe et al, 2010; Saffer and Marone, 2003), stability (Carpenter et al, 2015; Niemeijer and Spiers, 2006), and healing (Carpenter et al, 2016; Tesei et al, 2012).

A number of studies have focused on the mineralogical effect on frictional strengths using synthetic mixtures of strong and weak minerals. Lupini, et al first investigated the transition from high frictional strength to low frictional strength at low normal stresses in soil mixtures of rounded particles and weaker platy particles (1981). Based on their observations, they separated the transition from high friction to low friction of mixtures into 3 regimes. In the first regime, which features mixtures with 0-25 %, clay only a moderate reduction in frictional strength is observed. In the second regime, frictional strength decreases significantly and clay content increases up to 70%. In the third regime, as clay increases up to 100% the frictional strength decreases moderately to approach the minimum strength value of the clay end member. A more recent study evaluated the frictional strength of binary and tertiary mixtures of quartz-feldspathic and phyllosilicates materials at stresses relevant to seiesmogenesis (Tembe et al, 2010). They observed a similar trend to the low normal stress soil experiments of Lupini et al in smectite/quartz and smectite/illite/quartz mixtures. However, Tembe et al observed a linear strength transition from pure quartz to illite. Generally, gouges mixtures tend to decrease in frictional strength as weak, platy phyllosilicate minerals become more abundant.

Carpenter et al conducted a systematic evaluation of the healing behavior of a wide range of natural and monomineralic synthetic gouges (2016). They characterized steady state friction, healing rates and creep relaxation rates for 17 different samples with varying frictional strengths. They find that frictionally strong materials, which also tend to be velocity weakening, exhibit

greater dilation and healing rates making them likely candidates for hosting earthquakes. In contrast, phyllosilicate minerals show low strength and low rates of restrengthening (Figure 2.2). These studies have focused on healing during conventional SHS tests which investigate restrengthening processes that occur when a majority of the shear stress remains on the fault during the hold period. As discussed in chapter 1 and previous studies (Karner and Marone, 2001; Karner and Marone, 1998) granular materials such as Westerly granite and quartz exhibit shear stress dependent fault restrengthening (Figure 2.3). The lower the shear stress during the laboratory simulated interseismic period the higher the observed restrengthening. However, studies of this kind have been limited to frictionally strong materials and it is unknown how mineralogy influences the shear dependence of healing. To address this question, we conduct a suite of experiments on synthetic fault gouges composed of quartz and smectite mixtures and a subset of the natural gouges from Carpenter et al, 2016 in which we vary the shear stress during the hold period of SHS.

To investigate the mechanisms of deformation in phyllosilicate-rich gouge samples we also consider changes in layer thickness and the contribution to healing from net compaction during granular rearrangement. This work illuminates the mechanisms of frictional healing and extends the range of material compositions for which data are available on rates of frictional healing. In particular, the focus on phyllosilicate materials is important for applications to slip stability and permeability of natural faults.

2.3 Methods:

2.3.1 Experimental Apparatus:

Experiments were conducted in a biaxial testing apparatus (Figure 2.1) using the double direct shear (DDS) configuration (e.g., Karner and Marone, 1998; Anthony and Marone, 2005; Leeman et al., 2016). Normal and shear loads are applied to the sample using independently controlled hydraulic pistons. The pistons can be controlled in displacement or load mode using an electro-hydraulic servo-controlled feedback system. Force and displacement measurements are recorded at 10 kHz and averaged for storage to rates from 100-1000 Hz depending on the loading rate. The normal and shear loads are measured using Beryllium-Copper load cells (resolution ±10 N) fixed to the ends of the hydraulic pistons. Load point displacement measurements are recorded using DCDT transducers with 0.1 μm precision.

2.3.2 Sample Material and Geometry:

In this study, we examined two types of sample materials, synthetic mixtures and natural fault gouges. The synthetic mixtures are composed of granular quartz (F110) and the phyllosilicate mineral Calcium-montmorillonite (smectite). We prepared the mixtures by combining varying amounts of quartz and smectite by weight percent. We tested a total of 7 mixtures ranging from 0-100 % phyllosilicate (Table 2.1). For the synthetic mixtures, our laboratory faults have nominal frictional contact area of 10×10 cm^2. We use a three-block configuration for double direct shear (Figure 2.4). Two 5 mm thick layers of gouge are sandwiched between three grooved steel forcing blocks. Grooves are 0.8 mm deep with 1-mm

wavelength and ensure that shear occurs within the layers and not at the layer boundaries (e.g., Anthony and Marone, 2005; Rathbun et al., 2013). Gouge layers are constructed with the same initial layer thickness and using a leveling jig to ensure reproducibility from experiment to experiment (Table 1).

In addition to the synthetic mixtures, we also examined 4 natural gouge samples from both active and inactive fault zones. The natural materials tested included outcrop samples from Alpine Fault (New Zealand), Kodiak fault zone (Alaska), and San Gregorio Fault (California) and a borehole sample from the Nankai subduction zone (Japan). These samples contain different amounts of phyllosilicates (ranging from 33-63 %) as determined in previous studies and reported by Carpenter et al, 2016. Unfortunately, the uncertainty in these measurements remains unclear. For the natural samples we use the same DDS configuration as for the synthetic mixtures. The initial layer thickness is also 5mm. However, the natural sample laboratory faults have nominal frictional contact area of 5×5 cm^2 as limited natural gouge material is available.

2.3.3 Loading Procedures:

Experiments were conducted at a constant normal stress of 25 MPa. Loading procedures were slightly different for synthetic mixtures and natural samples primarily due to displacement limitations of the 5×5 cm^2 sample configuration.

For synthetic mixtures the initial loading procedure of each experiment consisted of a shear load cycle and a series of velocity steps totaling ~10 mm of displacement (Figure 2.5) modeled after the loading sequence of Karner and Marone (2001). During a shear load cycle the shear stress is completely removed from the sample and quickly reapplied. This technique takes advantage of shear enhanced compaction (Zhu and Wong, 1997) and comminution to attain a steady state grain size distribution (e.g., Marone and Scholz, 1989) and shear fabric (Logan et al., 1992). We sheared

samples at 10 µm/s and unloaded at 300 µm/s. After the initial loading procedure, we conducted a series of 6 SHS tests.

During a SHS test, the sample is first sheared at a constant load point velocity until steady state friction is attained. The vertical piston is then quickly retracted for a specified amount of time to reach the desired shear stress. Note that for conventional slide hold slide tests there is no unloading stage. The load point velocity is then set to zero and the hold begins. After the specified hold time, 100 seconds for our experiments, the sample is reloaded at 10 µm/s. Upon reloading, friction reaches a peak value and decays to steady-state. Consistent with previous works, we quantify frictional healing, Δµ, as the difference between peak friction after the hold and the steady state friction prior to the hold (Figure 2.1). Note that we define friction as the ratio of shear and normal stress calculated from the force measurements and nominal surface area of the sample.

To investigate the impact of shear stress on healing, SHS tests are conducted at different normalized shear stress values (η). We follow the convention of Karner and Marone (2001) and quantify η during the hold by the ratio of the shear stress at the start of the hold to the steady-state shear stress value prior to unloading.

$$\eta = \frac{\tau_{hold}}{\tau_{pre-unload}}$$

The two end member cases are presented in Figure 2.1 for a conventional SHS test where η = 1 (black) and the zero shear stress case where η ≈ 0 (grey).

For natural samples, the initial loading procedure is shortened to ~8 mm, but it also consists of a shear load cycle and a series of velocity steps. After the initial load up, we conduct a total of 36 SHS tests at 18 different η values. The SHS tests are conducted using a series of control files which control the velocity of the vertical piston. Two controls files were used to cover the range of η values investigated in this study. Each control file featured 9 SHS tests and each of the files was run two times for a total of 36 SHS tests. We only have access to a small amount of natural fault

gouge which limits the amount of shear during a single experiment and the number of experiments we can conduct on a given fault material. To allow for more SHS tests in a single experiment we reduced the amount of shear between tests from 2 mm (synthetic mixtures) to 0.5 mm (natural gouges).

2.3.4 Ultrasonic Measurements:

We probed the evolution of friction and ultrasonic amplitude during our experiments using P-polarized piezoelectric transducers (PZT) with central frequency 500 kHz. The transducers are embedded in steel blocks located next to the side forcing blocks of the DDS configuration. One transducer transmits short pulses (half a sine cycle at 500 kHz) every 4-10 milliseconds throughout the experiment, while the second PZT is used as a receiver. A 14 bit acquisition system records the waveforms at 25 MHz.

Acoustic measurements were recorded during 10 synthetic mixture experiments. Two sets of steel blocks containing PZT's were used (Figure 5.4). The flat block geometry features a set of acoustic blocks placed outside of the traditional DDS sample setup and coupled using molasses. The second geometry utilized grooved acoustic blocks that also serve as the forcing blocks in the 3-block DDS setup (Figure 2.4). Seven experiments used the flat block geometry and three used the grooved block geometry (Table 2.2).

2.4 Results

2.4.1 Steady-state Friction:

Simulated gouge mixtures containing 0-100% smectite exhibit steady state friction (μ_{ss}) values between 0.12 and 0.65 with friction generally decreasing with increasing smectite content (Figure 2.6). Steady state friction values were measured after the initial loading sequence of each experiment at ~ 10mm displacement (Table 2.2). While mixture composition appears to exert the first order control on frictional strength, we observe some instances in which a mixture is frictionally stronger than another mixture containing slightly less smectite. For example, μ_{ss} of the 30 % smectite mixture (0.47-0.49) is higher than the 40 % smectite mixture (0.45-0.46). In some experiments, pure smectite was frictionally stronger than the 30% smectite mixture.

We observe differences in initial loading behavior between quartz dominated and smectite dominated mixtures (Figure 2.6). For mixtures with ≥ 50% smectite, initial yielding is characterized by a well-defined frictional peak followed by decay to a lower steady state value. This behavior is frequently observed in materials containing weak, phyllosilicate material and likely results from the alignment of platy minerals as fabrics develop allowing for sliding along weak shear planes. Whereas in mixtures with ≤50% F110 we observe rollover during initial yielding at values close to the steady state friction value. Friction evolves to a steady state after ~5 mm in most experiments.

The steady-state friction of the 4 natural samples ranges from 0.40-0.65 (Figure 2.7; Table 2.2). Steady-state friction measurements were taken at ~6.6 mm displacement. The Nankai gouge contains the least amount of phyllosilicates (33 %) but exhibits the lowest μ_{ss} of the natural samples studied. The Alpine fault gouge with the second lowest phyllosilicate percentage (40 %)

has the highest μ_{ss} of our natural samples. The San Gregorio and Kodiak gouges have intermediate friction values of 0.50 and 0.54 for phyllosilicate contents of 52% and 63%, respectively. However, as previously mentioned, the uncertainties associated with the phyllosilicate content measurements are not clear and it is possible that the errors in these measurements obscure any potential trends between phyllosilicate content and steady-state frictional strength. Nonetheless, for the η=0 case we observe that frictional healing is very low for materials with friction values below 0.4 and increases with steady-state friction for $\mu_{ss} > 0.4$ (Figure 2.8)

The natural samples also exhibit interesting strain dependent behavior. The San Gregorio, Alpine Fault, and Kodiak samples yield and rollover at friction values close to their respective μ_{ss} over the first 1-3 mm of displacement. In the Nankai sample we observe a well-defined friction peak and decay to μ_{ss} within 1-3 mm of displacement. Long-term strain weakening is observed in the Nankai and Kodiak gouges and slight strain hardening in the San Gregorio gouge (Figure 2.7). The Alpine Fault sample did not show a long-term strain dependent trend.

2.4.2 Shear Stress Dependent Frictional Healing:

In the synthetic mixtures, frictional healing ($\Delta\mu$) also varied systematically with increasing smectite content, consistent with previous work that focused on conventional SHS tests (Figure 2.10; Carpenter et al, 2016). Here we are interested specifically in how the addition of smectite impacts the shear-stress dependent strengthening trend that is observed in pure quartz and Westerly granite gouges (Figure 2.3). For mixtures with < 20% smectite, frictional healing continues to show a dependence on η in which healing increases as η decreases. For the 20% smectite mixture, $\Delta\mu$ increases from 0.006 to 0.022 as η decreases from 0.72 to 0.01. For

samples with ≥ 50% smectite, we no longer observe an inverse dependence on η. Instead, frictional healing increases from 0 to 0.002 with increasing η. For intermediate compositions with 30-40% smectite we notice a transition between these two behaviors in which Δμ appears independent of η.

With the exception of the Alpine Fault sample, all of the natural gouge samples show an increase in Δμ with increasing η (Figure 2.11). These samples experience greater healing than quartz -smectite mixtures containing similar percentages of phyllosilicates. The Nankai gouge restrengthens the least with negligible healing during zero shear stress SHS and Δμ increasing up to 0.027 for η=0.83. The San Gregorio and Kodiak gouges exhibit very similar healing behaviors with Δμ increasing from ~0.01 to ~ 0.05 with increasing η. The Alpine Fault gouge had the highest frictional healing of all samples including the pure quartz end member (Figure 2.9). The Alpine Fault healing values range from 0.041 to 0.078. Slightly higher values are observed at lower η. This sample also has more variability in Δμ with shear displacement than observed in the other natural samples (Figure 2.11). During the natural sample experiments we ran the same series of SHS tests two times and therefore have healing measurements at similar η from two different shear displacements. Figure 2.11 shows a comparison of Δμ measurements taken during the first set of SHS (circles) and those from the second set of SHS tests (triangles). In the Alpine Fault gouge there appears to be a change in the shear stress dependence of healing between the first and second SHS tests not observed in the other natural gouges.

2.4.3 Layer Thickness Evolution:

For granular materials shear strength varies as a function of particle size distribution, particle packing, porosity, and the degree of shear localization. To evaluate these effects, we continuously monitor the evolution of fault zone thickness during shearing and SHS tests (Figure

2.12). We use vernier calipers to measure initial fault zone thickness under normal load prior to shear in each experiment. These measurements are accurate to ±50 μm. We continue to monitor changes in layer thickness throughout experiments via the DCDTs (Figure 2.1), with a precision of ±0.1 μm. In all experiments layers densify upon initial shear and thin steadily as the fault zone undergoes geometric spreading (e.g., Scott et al., 1994) in simple shear (Figure 2.12). The amount of initial compaction varies systematically with smectite content in the synthetic mixtures. Pure smectite layers compact by over 60 % whereas the quartz end member experiences less than a 20% reduction in layer thickness. During SHS tests the layers compact and dilate as the experimental faults are loaded and unloaded. From the continuous record we examine changes in layer thickness during 3 parts of the SHS test to help understand the microscale processes invoking these changes.

We calculate unload compaction (ΔTu), hold compaction (ΔTh), and reload dilatancy (ΔTr) (Figure 1.5). In the synthetic mixtures unload compaction varies systematically as a function of quartz content and normalized shear stress (Figure 2.13a). Mixtures with > 50% smectite do not compact during unloading. Unload compaction for samples with 20% smectite varies from 4 to 15 μm with decreasing shear stress. Hold compaction varies between 1-4 μm for most samples with < 50 % smectite and mixtures above this threshold exhibit very little change in layer thickness throughout SHS tests (Figure 2.13b). The addition of as little as 20 % smectite reduces the amount of reload dilatancy to less than 3 μm (Figure 2.13c). Dilation in pure quartz is the greatest and the only synthetic gouge that has a clear η dependence.

In all of the natural gouges unload compaction scales inversely with η and with the frictional strength of the material (Figure 2.13d). For zero shear stress SHS tests, the magnitude of ΔTu ranges from 5-13 μm compared to 1-2 μm observed during conventional SHS tests. Hold compaction is < 5 μm for all natural samples (Figure 2.13e). The lowest ΔTh correspond to the

lowest stress holds where $\eta<0.2$. As η increases above 0.2 the hold compaction appears to level off. Reload dilatancy was noticeably higher for the Alpine Fault gouge, up to 2 times the amount observed in the San Gregorio, Kodiak, and Nankai gouges (Figure 2.13f). The η dependence is also more pronounced in the Alpine Fault gouge.

Frictional healing characterizes the processes that occur during an entire SHS test. Therefore, we are interested in the total change in layer thickness that occurs during these tests and examine the combined effects of unload compaction, hold compaction, and reload dilatancy Figure 2.14). Quartz dominated mixtures exhibit the greatest change in layer thickness which scales inversely with η. Intermediate mixtures (30-50 % smectite) and the natural gouge samples show a less pronounced η dependence and total layer thickness change typically between 5 and 10 μm. Mixtures with more than 50 % smectite have a total change in layer thickness of < 5 μm.

2.4.4 Ultrasonic Amplitude Evolution:

During synthetic mixture experiments we monitored the ultrasonic acoustic amplitude during SHS tests. We select the maximum amplitude in a 3 μs window near the first arrival which corresponds to the first positive arrival. A background increase in peak amplitude is observed during steady state shearing. The rate of increase is greater for mixtures with less phyllosilicates. Changes in amplitude during SHS tests decrease as smectite content increases (Figure 2.15). We analyze changes in amplitude during each portion of the SHS test and characterize three amplitude measurements, A^U, change in amplitude during unloading, A^H, the change in amplitude during the hold, and A^R, the change in amplitude from the onset of reloading to peak friction (defined in Figure 2.16 for a frictionally strong sample). We observed that A^U is smaller than both A^H and A^R (Figure 2.17) . The amplitude change during unloading is less than half of the

change observed during both the hold and reloading. Amplitude changes vary systematically with η for mixtures with < 50 % smectite but the effect becomes muted for the 50% smectite mixture and is absent in the 70% smectite mixture.

To investigate the time dependent restrenthening that occurs during the hold period we focus in on the amplitude evolution during that time (Figure 2.18). For a given experiment, that the time dependent evolution of amplitude is similar for all shear stress values. The amplitude increases with the logarithm of time rates are generally faster for higher stresses with the exception of the smectite dominated mixture (70 %) which has similar rates for all shear stresses.

2.5 Discussion:

2.5.1 Discussion Steady State Friction:

Our results are consistent with the range of frictional behavior observed in previous studies on similar gouge mixtures (Saffer and Marone, 2003; Tembe et al, 2010; Kenigsberg et al, in prep). While Tembe et al, 2010 presented a decrease in steady state friction with increasing smectite content we observe some deviation from this trend. The 30 % smectite mixture was slightly stronger than the 40 % mixture and one experimental run of 100 % smectite was stronger than the 70 % smectite mixtures. However, this type of variability has been observed in other studies of quartz and smectite mixtures (Saffer and Marone, 2003 and Kenigsbergs in prep). The composition of the mixtures is the first order control on the frictional strength and we believe this deviation may result from changes in relative humidity conditions which were not controlled during these experiments.

The most variability in μ_{ss} occurs for mixtures with the highest smectite content. Friction in samples composed solely of smectite varied from 0.12-0.22. One possible explanation for this behavior is the hydration state of the smectite clay may vary between experiments because the relative humidity conditions were not regulated. Ikari et al, 2007 investigated the impact of hydration state on pure smectite and quartz/smectite mixtures. The frictional strength of smectite decreases as additional water is bound in between Ca cations. The difference in frictional properties between dry and samples with water bound molecules scales with the amount of smectite in the mixture making pure smectite samples most susceptible to changes in friction from varying humidity conditions, consistent with our observation of higher frictional variation in mixtures with high smectite content. The μ_{ss} from the three 100 % mixture experiments are 0.12, 0.22, and 0.22 for humidity conditions of 100%, 56%, and 82-100%, respectively. The weakest coefficient of friction was recorded during the highest humidity experiment consistent with the observations of Ikari et al, 2007.

The relative steady state strengths of the four natural gouges are consistent with previous observations (Carpenter et al, 2016). It is important to note that the relative abundance of different phyllosilicate minerals is very important for determining strength as some minerals such as smectite are significantly weaker than others like illite and kaolinite. As evidenced by our synthetic mixtures which plot lower than natural gouges with similar phyllosilicate contents. In addition, there could be some differences between the material we used to conduct our frictional experiments and the material used to determine the mineralogy as some samples exhibited small-scale variability. For example, samples collected from the Nankai Trough just a few meters apart exhibited mineralogies with significantly more phyllosilicates (Steurer and Underwood, 2003).

2.5.2 Shear Stress Dependent Frictional Restrengthening in Synthetic and Natural Gouges:

Synthetic mixtures with smectite content less than 20% exhibit a similar shear stress dependence to pure quartz and Westerly granite gouges (Figure 2.9). In these mixtures, the frictionally strong particles control the frictional behavior as expected based on the work of Tembe et al, 2010. The quartz grains act as the supporting framework with small amounts of smectite interspersed. We suspect that in these systems changes in frictional strength derive primarily from particle rearrangement, dilatant work, and net compaction that occurs during SHS tests as evidenced by the η dependent changes in layer thickness (Figure 2.13).

As smectite content increases to 30-40% the magnitude of frictional healing decreases significantly and does not have a clear η dependence. However, total change in layer thickness continues to scale with η. We interpret this to mean that the restrenthening processes in gouges of intermediate composition do not primarily gain strength from processes involving just the quartz particles. In this case, strength results from the combined effects of particle rearrangement, dilatant work, and net compaction in quartz and a component from healing of smectite particles. During SHS test at high η, significant interparticle stresses prevent slip and this allows for aging of existing contacts. During low η SHS, it is possible that increased slips erases newly healed contacts and accounts for the positive η dependence of healing in smectite. This idea is consistent with the observations of ultrasonic amplitude increase during the hold period of SHS tests (Figure 2.17). For all mixtures with < 70% smectite the rate of healing during the hold period is greater for higher stresses. It is worth noting that this behavior is not observed in pure quartz systems (Figure 1.13). If smectite exhibits a positive η dependence during SHS tests than combined with the contribution of healing from quartz particles which show a negative η dependence the overall trend could appear η independent.

Synthetic mixtures containing 50 % smectite show a slight increase in frictional strengthening as η increases. A slight negative η dependence is still observed in total layer thickness change but the magnitude is relatively small (< 5μm) suggesting the quartz contribution to healing is less significant. From the steady state friction behavior, we infer that the gouge mixture is in a transitionary stage between a quartz supported frame work and a smectite matrix supported system in which more clay particles are filling the gaps between quartz grains. (Tembe et al, 2010). As smectite is more abundant, we expect the contribution from smectite healing to increase and become the dominant healing mechanism explaining the transition in η dependent strengthening from neutral to slightly positive.

For mixtures with 70% smectite or more, observed healing is negligible. In these mixtures smectite completely dominates the frictional strength and healing. This is consistent with other studies which suggest that contact area becomes completely saturated and no further strengthening is possible as the number of contacts and size of contacts remains constant. Since the quartz particles in the mixture are completely isolated and the smectite particles have reached their maximum stress and peak strength than we would expect the frictional state to be relatively constant, consistent with our observations.

The natural gouges examined contained 33-63% phyllosilicates. Therefore, we might expect that their η dependent healing behavior to be similar to synthetic mixtures with the same percentage of phyllosilicates. The results are in general agreement but there are some nuisances. As previously discussed, healing in the San Gregorio, Kodiak, and Nankai gouges exhibit a positive η dependence. This trend is similar to what is observed in the 50% smectite mixture but the increase in healing with η is more pronounced. This is not surprising if we consider that smectite has the lowest frictional strength and magnitude of healing of the phyllosilicates present in this study (Figure 2.2). In these natural gouges, although the total percentage of phyllosilicates

is similar the types of phyllosilicates are more varied and include frictionally stronger minerals that contribute more to healing.

The outlier in these observations is the Alpine Fault gouge which experiences the largest magnitude of healing of all samples studied. One explanation for the observed strength and pronounced strengthening in this sample is the influence of calcite. The strengthening rate of calcite is at least 3 times that observed in the other minerals present in the gouges. The Alpine Fault sample has ~40 % phyllosilicates. For synthetic gouges with a similar percentage we observed an η independent behavior thought to be the result of the competition between the negative dependence of η observed in the frictionally strong quartz grains and the positive η dependence of the smectite particles. In the case of the Alpine Fault we imagine that the influence of the quartz or frictionally strong component is increased 2-3 fold by the presence of calcite which would increase healing particularly at low η. The phyllosilicate minerals present are also stronger than the smectite from the synthetic mixtures and this would increase healing specifically at high η. The combined effect is an overall increase in healing observed at all η values. Therefore, we interpret this to mean that the same η dependent processes are in competition but that the magnitude of healing in both cases is elevated based on the specific mineral present.

2.5.3 Summary of Shear Stress Dependent Healing:

In summary, we interpret shear stress dependent healing in gouges of mixed mineralogy to result from the competition between two processes that have opposite dependences on η (Figure 2.19). The first process is controlled by the frictionally strong components of the gouge and exhibit a negative dependence on η (as discussed in Chapter 1 for Westerly granite). The second process is controlled by the weaker, phyllosilicate minerals and shows a positive η stress

dependence. How these processes operate in conjunction is determined by the relative abundance of minerals in the gouge. When the strong quartz grains dominate the system and have a well-defined grain network than an overall negative dependence on η is observed for healing. As the network becomes less connected and larger pockets of frictionally weak phyllosilicates disrupt the grain network, the contributions to healing from both processes are comparable in magnitude and combine for an overall neutral effect. As the weak minerals become slightly more dominant, they control the shear stress dependent behavior but ultimately if the system becomes completely matrix supported healing becomes negligible as contact area is likely saturated early on.

2.6 Conclusion:

The negative shear stress dependence of frictional strengthening previously observed in quartz and Westerly granite appears to be one of the competing processes that governs fault restrengthening behavior. In pure phyllosilicate systems, no stress dependence is observed as contract area is interpreted to be fully saturated and contacts are unable to grow or form. However, when phyllosilicates are abundant in gouge but interspersed with frictionally stronger grains they are prevented from reaching a stage where contact area and frictional strength have reached a maximum value and thus have room for frictional strength to evolve as a function of η. This study highlights the complexity of frictional strength that results from the interplay of minerology and shear stress conditions that can have important implications for faults at shallow crustal depths.

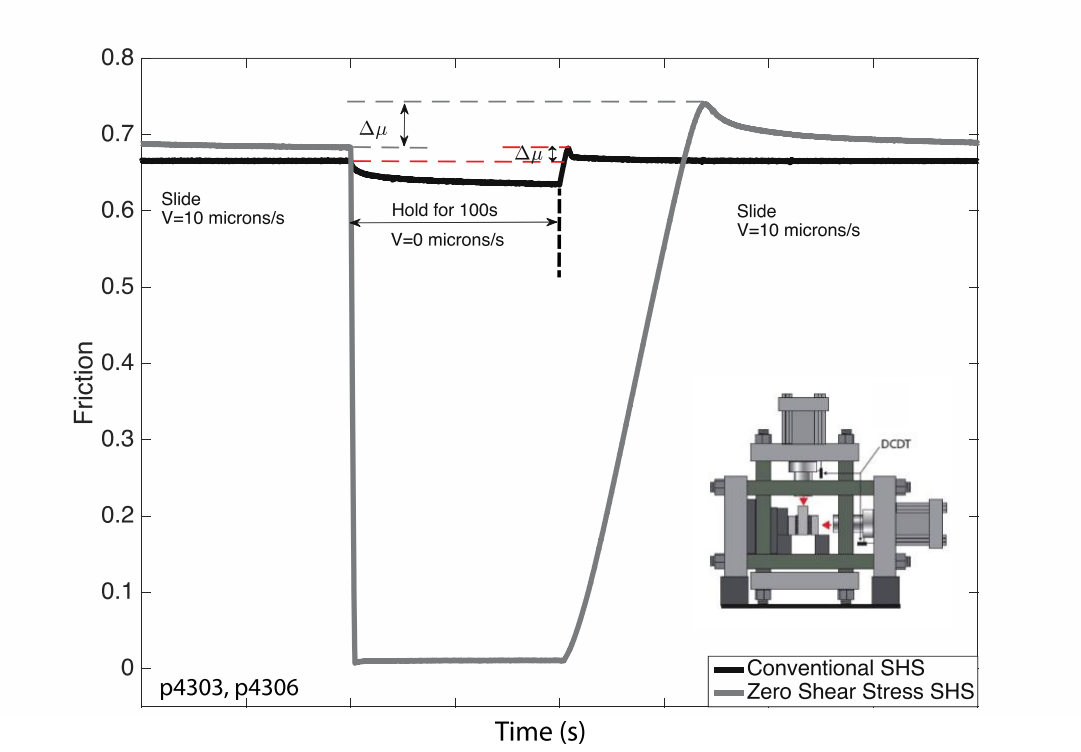

Figure 2.1:
Overview of frictional healing measurements from slide-hold-slide (SHS) tests conducted in a biaxial deformation apparatus (inset from Scuderi, 2014). The frictional evolution before, during, and after a 100-second hold period. Two shear stress end member cases are shown, the conventional case where the hold begins at the steady state shear stress level (η =1;black) and the zero shear stress case where the shear stress is completely removed prior to the hold (η =0; gray). Frictional healing, Δμ, is quantified by the difference between peak frictional strength upon reloading the sample after the hold and steady state friction prior to the hold.

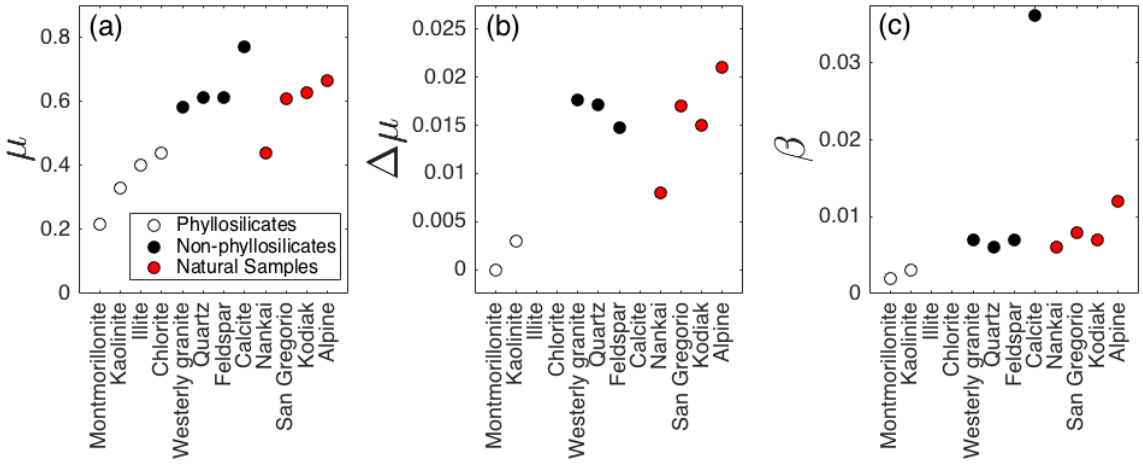

Figure 2.2:
Steady-state coefficient of friction, frictional healing, and healing rates for some common phyllosilicate materials (unfilled circles), non-phyllosilicate materials (filled circles), and natural gouges (red circles) used in this study (data from Carpenter et al, 2016; Giorgetti et al, 2015; and Behnsen and Faulkner, 2012). In general, phyllosilicate materials tend to be frictional weaker and have lower healing rates than non-phyllosilicates (i.e. quartz, feldspar, and calcite). Natural gouge samples contain between 30-60 % phyllosilicates.

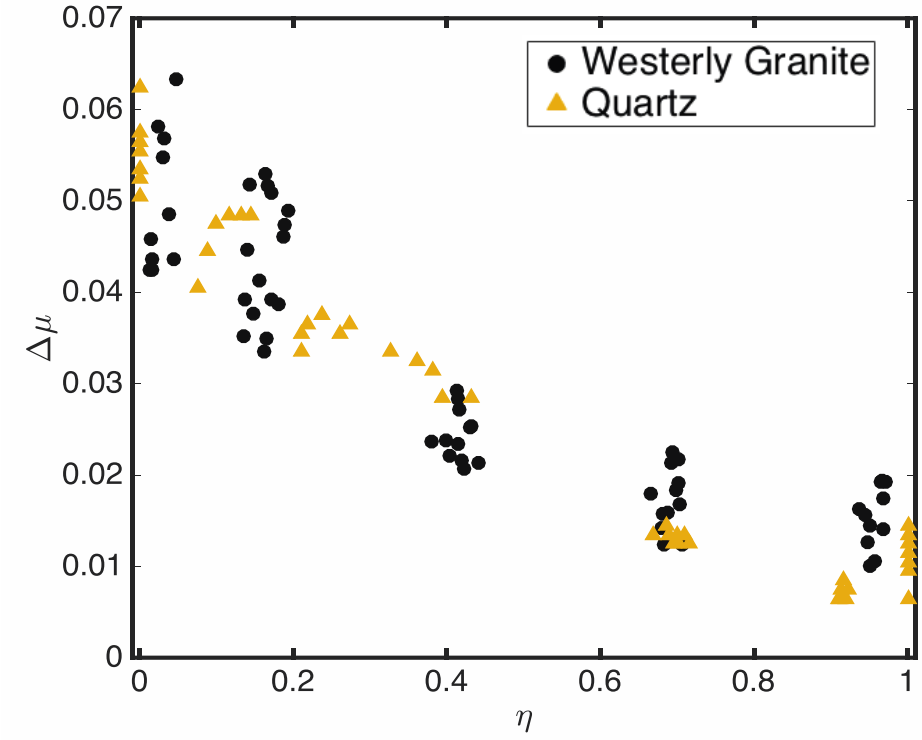

Figure 2.3:
Frictional healing versus normalized shear stress (η) for F110 (yellow triangles; Karner and Marone, 2001) and Westerly granite gouge (black circles; Ryan et al, submitted manuscript 2018). In these frictional strong granular materials frictional healing shows a clear dependence on η.

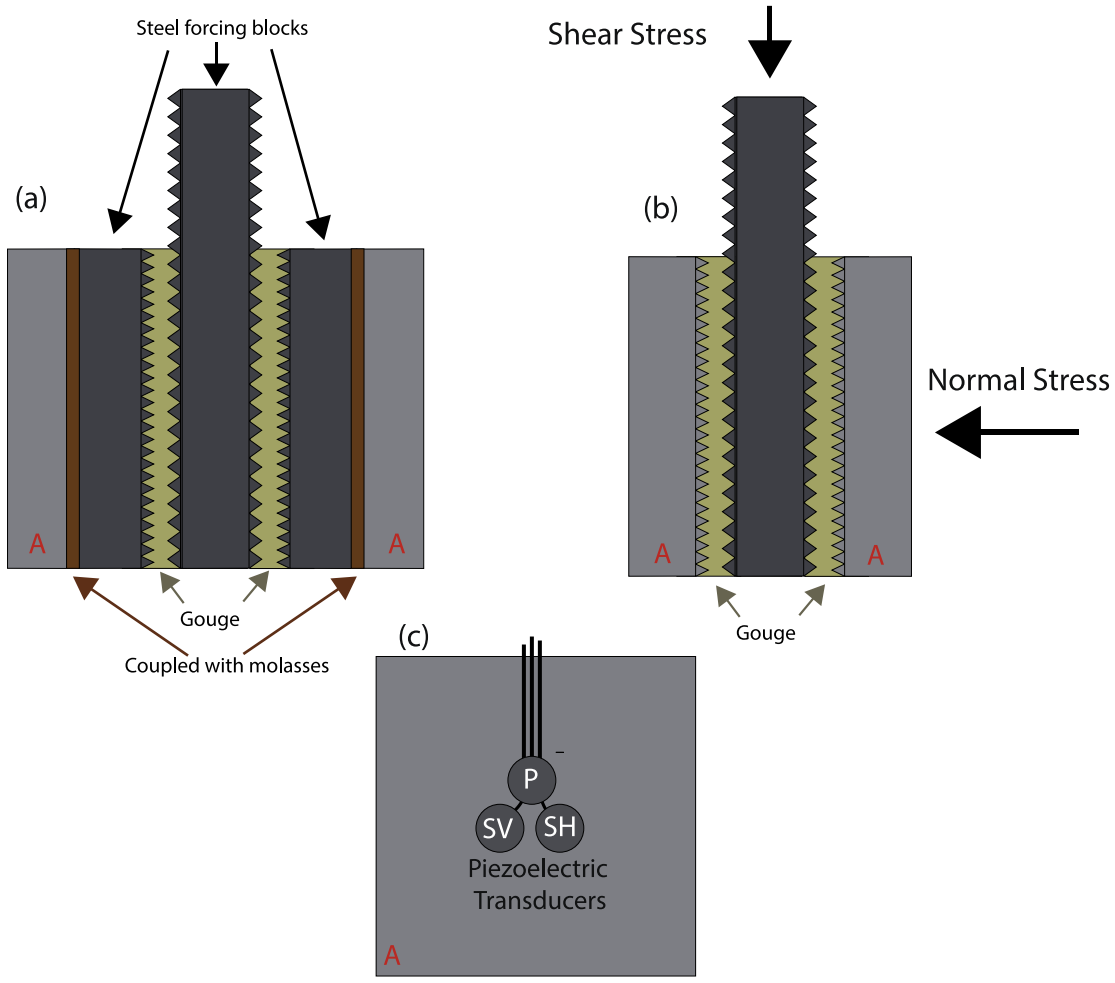

Figure 2.4:
(a) Double direct shear (DDS) geometry using the flat acoustic blocs. The flat acoustic blocks (labeled 'A') are placed on the outside of the three steel forcing blocks and two gouge layers. The acoustic blocks are coupled to the forcing blocks using a thin layer of molasses. (b) The DDS shear geometry with the grooved acoustic blocks. Here the acoustic blocks also serve as the forcing blocks. The black arrows indicate the directions of the applied normal and shear stresses. (c) Side view of the acoustic blocks that contain embedded piezoelectric transducers (PZTs) used to transmit and receive ultrasonic pulses Each block has 3 PZTs, one polarized in the P, SV, and SH directions.

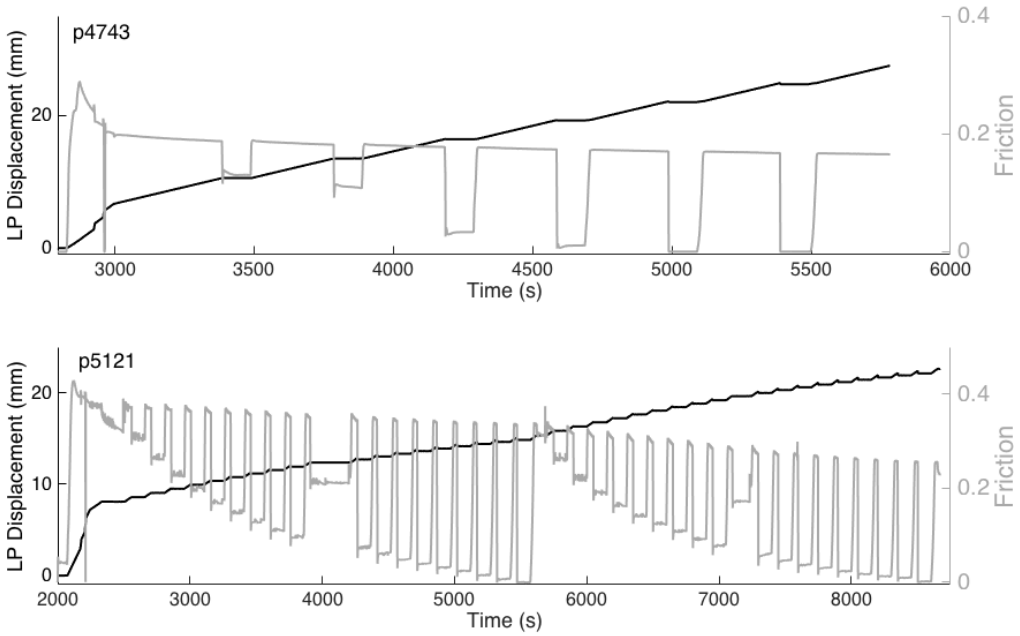

Figure 2.5:
Loading procedures (black) and frictional response (gray) for synthetic mixtures (a) and natural samples (b). In natural samples we reduce the amount of shearing between SHS tests due to smaller sample size and limited gouge material.

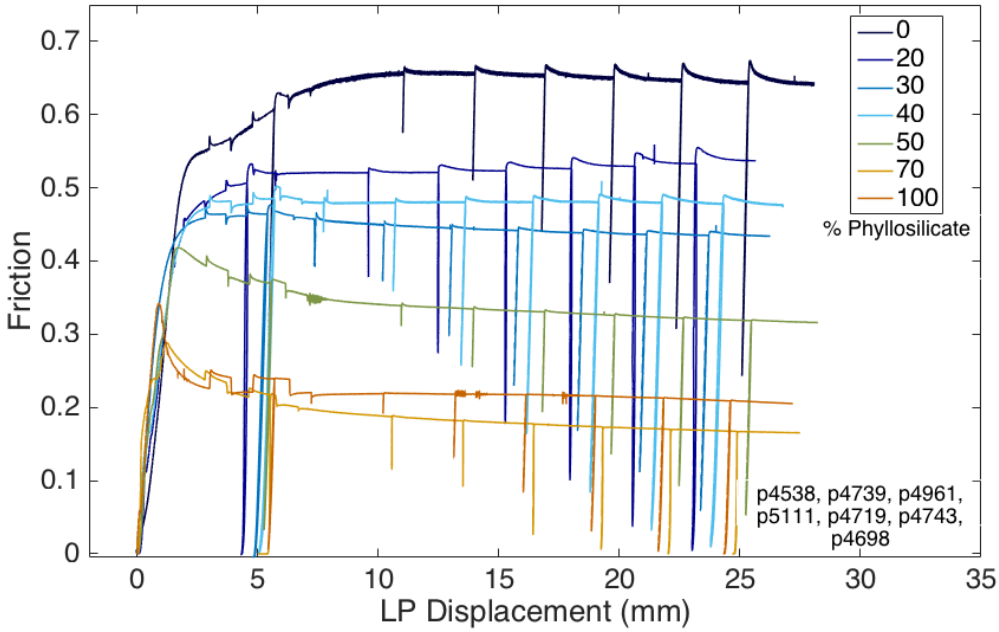

Figure 2.6:
Friction versus loadpoint displacement for a subset of experiments conducted on synthetic gouge mixtures with different compositions. One representative experiment of each mixture is shown. Mixtures contain different weight percentages of quartz powder (F110) and Ca-montmorillonite (smectite). Phyllosilicate content varied from 0-100%. Full list of experimental parameters is given in Table 2.

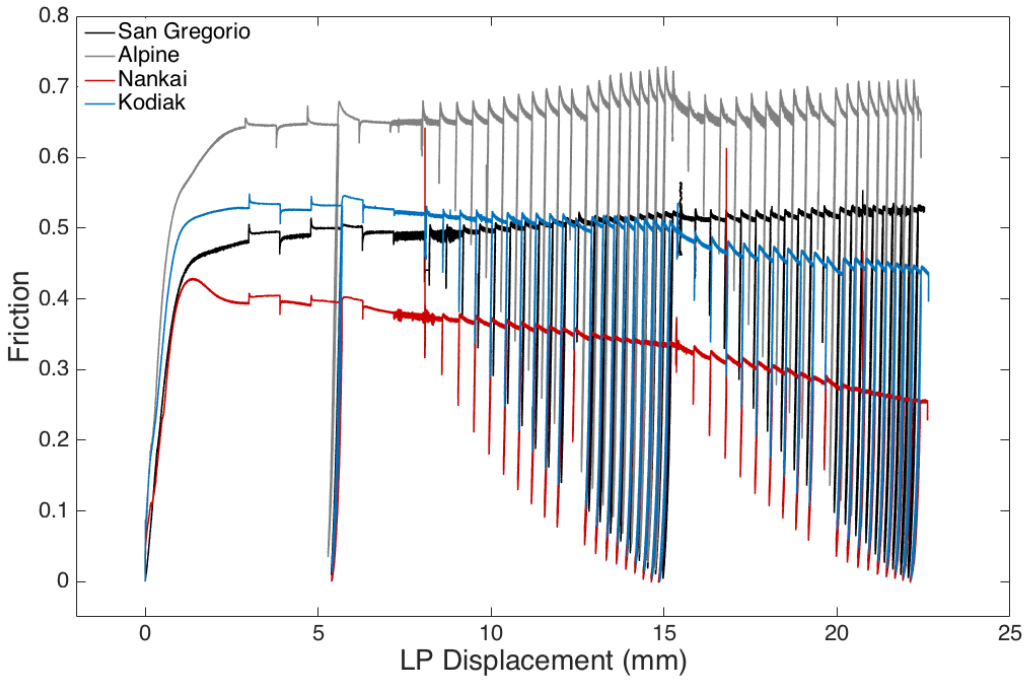

Figure 2.7:
Friction versus load point displacement for 4 experiments conducted on natural fault gouge materials. Each experiment included 36 100- second slide hold slide tests. Mineralogy of natural samples are described in Table 1 and key experimental and frictional parameters in Table 2.

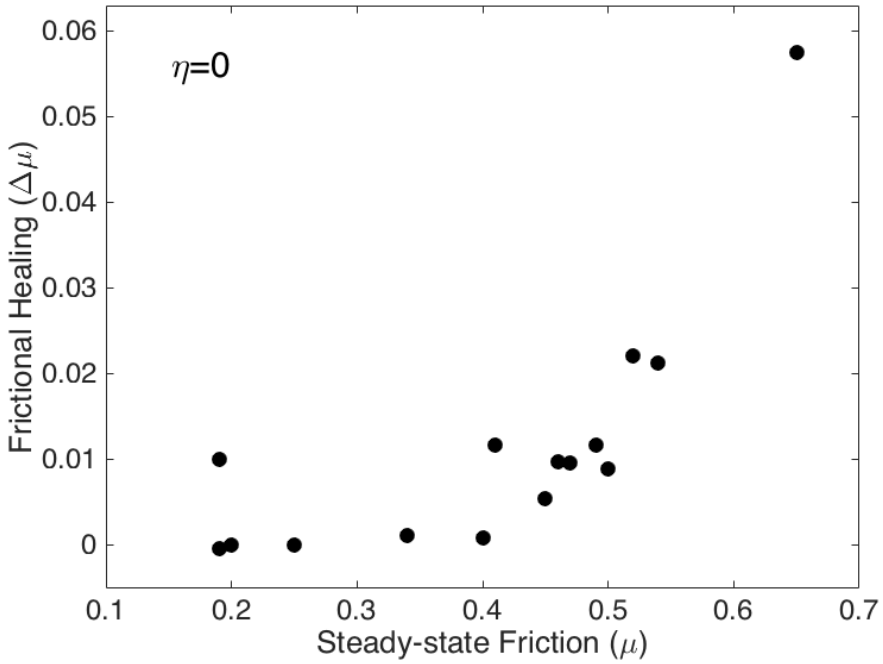

Figure 2.8:
Frictional healing versus steady-state friction for η=0. Frictional healing is minimal for steady-state friction < 0.4 and increases with steady-state friction for values > 0.4.

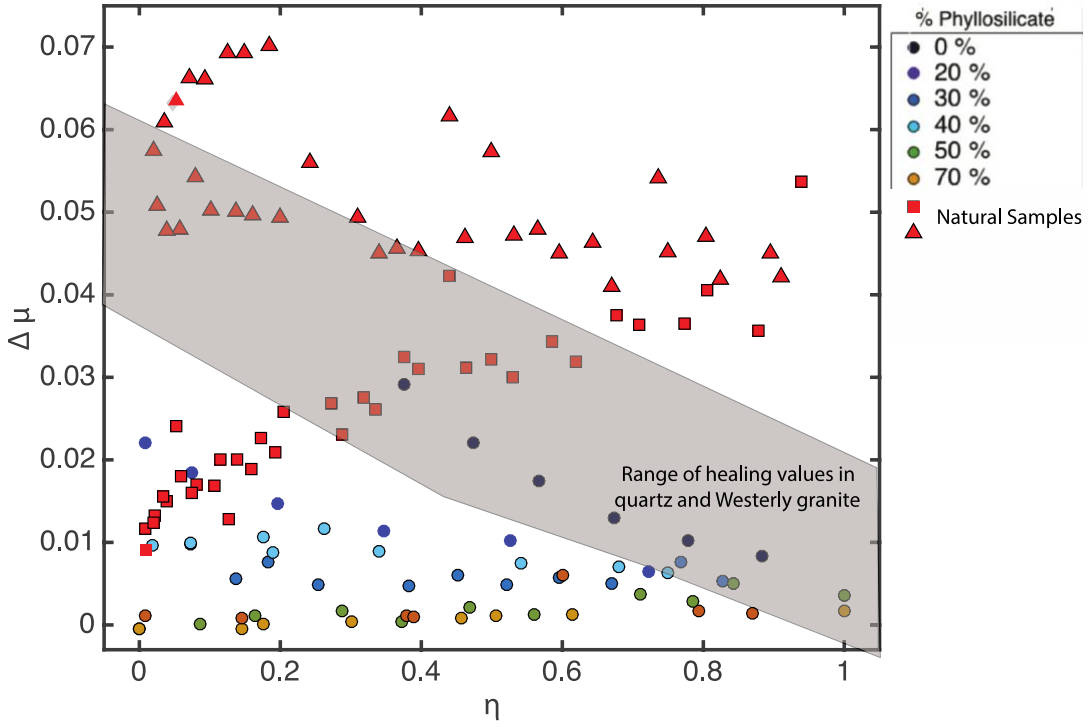

Figure 2.9:
Frictional healing (Δμ) versus normalized shear stress (η). Blue-gold colors denote different synthetic gouge compositions with phyllosilicate content ranging from 0-100%. Red symbols denote natural gouge samples. Frictional healing decreases with increasing phyllosilicate content in synthetic mixtures. For sample mixtures with < 20% phyllosilicate, frictional healing increases with decreasing normalized shear stress similar to the trends previously observed in F110 and Westerly granite (gray shaded area). For samples with < 50% phyllosilicate we observe a slight increase in frictional healing as η increases.

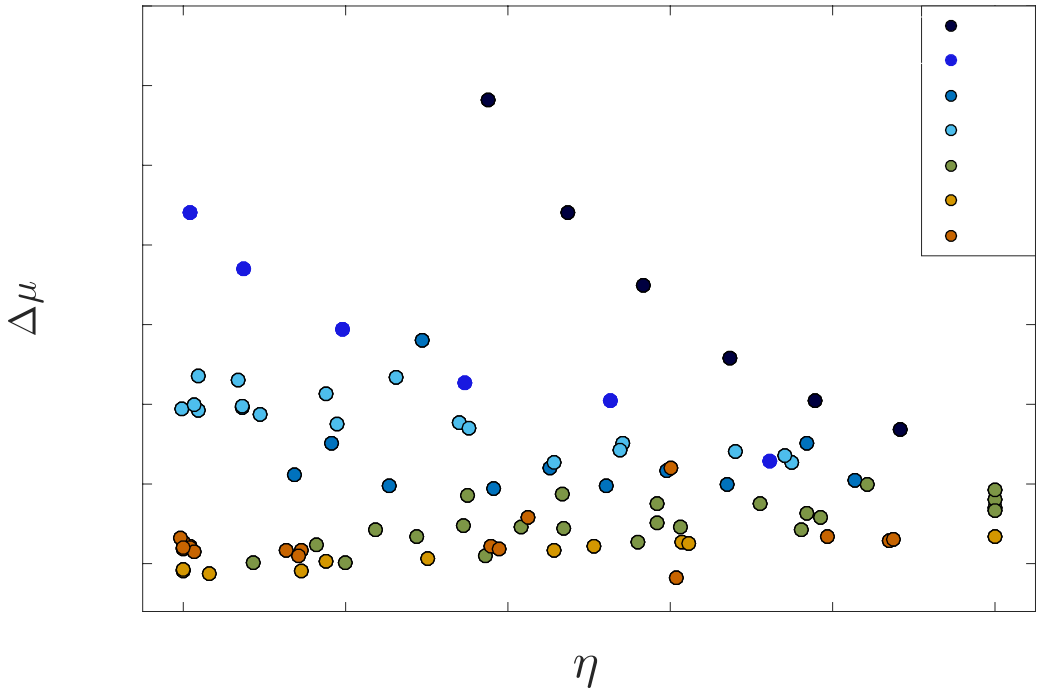

Figure 2.10:
Frictional healing versus η from synthetic gouge experiments. Mixtures with 20% smectite or or less show a negative dependence on η. Mixtures between 20% and 50% show η neutral behavior. 50 % smectite mixtures show a slight positive η dependence. Generally, very little healing is observed for mixtures with 70 % or more smectite.

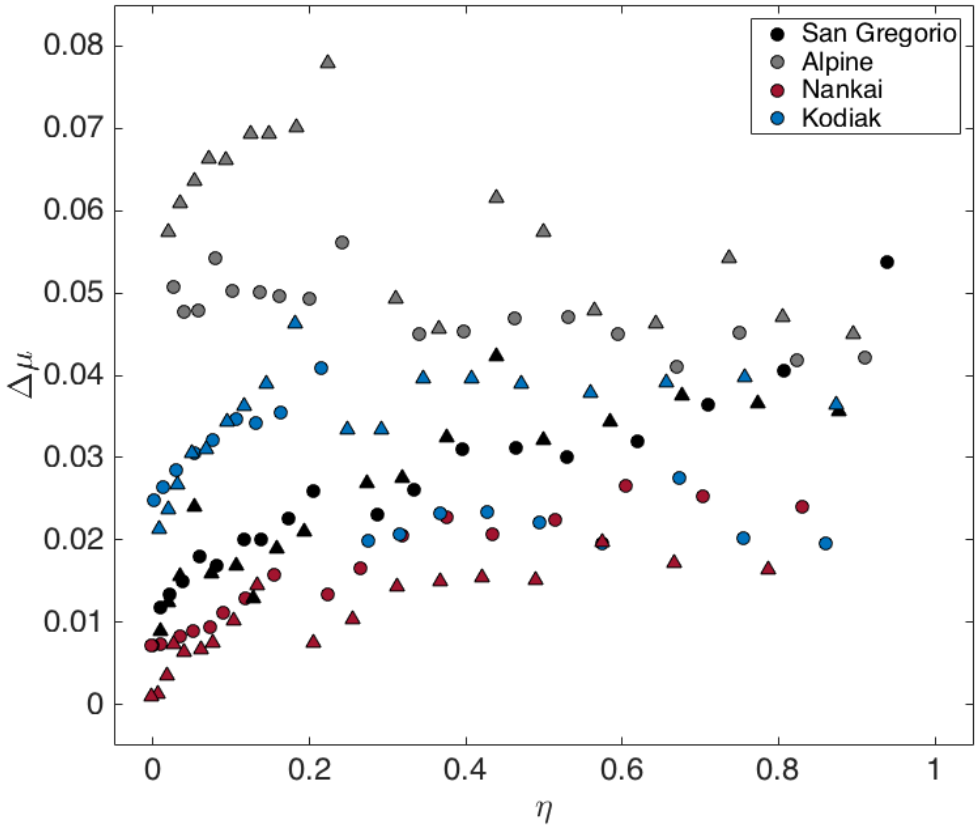

Figure 2.11:
Frictional healing versus η from natural gouge experiments. Circles indicate measurements from the first set of SHS tests and triangles from the second set of SHS tests. The San Gregorio, Nankai, and Kodiak faults show similar stress dependent trends for both sets of SHS tests. There is a notable break in healing trends observed around η = 0.2 which corresponds to break in control files (see Methods for details). In the Alpine Fault gouge (gray) we observe that the first set of SHS tests healing is inversely related to η. However, in the second set of SHS tests at η values between 0 and 0.2 an increase in healing with η is observed.

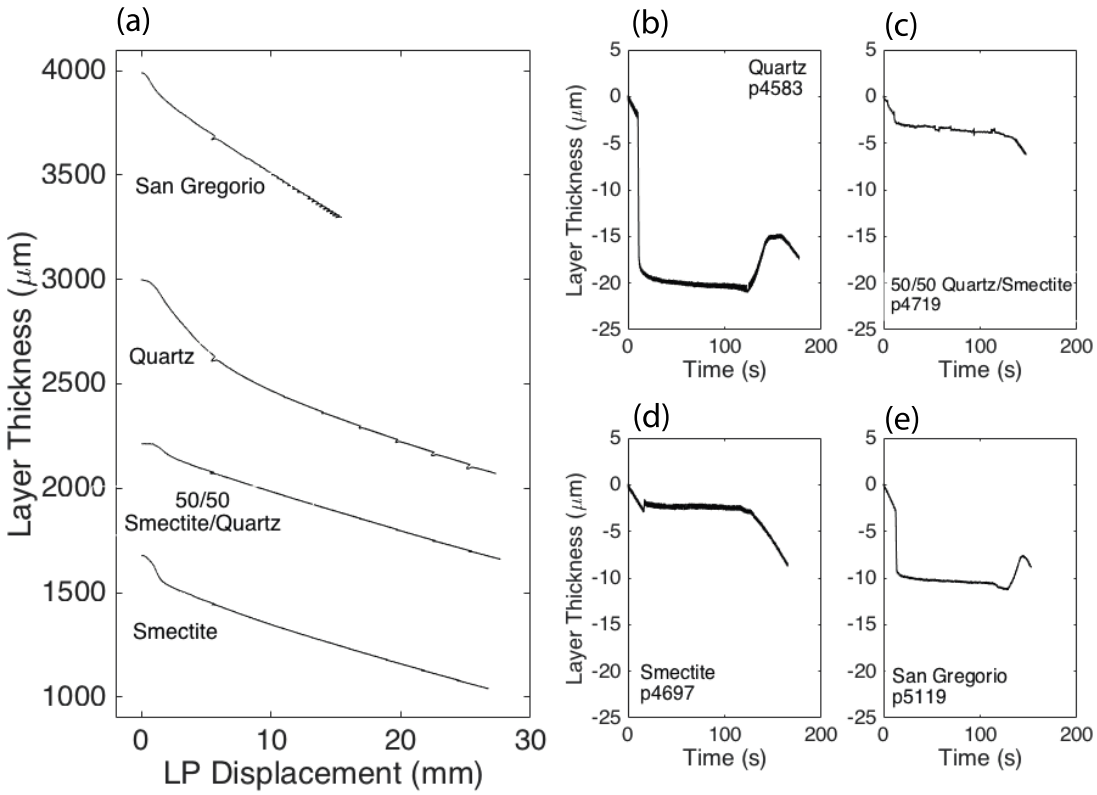

Figure 2.12:
(a) Layer thickness evolution versus loadpoint displacement during experiments in 0%, 50%, and 100% smectite mixtures as well as an example from a natural fault gouge (San Gregorio). All layers were initially 5 mm with the exception of the pure quartz which had an initial layer thickness of 3mm. After the normal load was applied samples were allowed to compact for a minimum of 15 minutes until the layer thickness reached a steady-state prior to applying a shear load. The gouge layers thin throughout the experiment partially due to geometric thinning (Scott et al, 1994). Small changes in layer thickness occur during SHS tests. Panels b-d show a zoom in of a single SHS from each experiment at low shear stress. Time and layer thickness are referenced to the beginning of unloading (duration <2 s). During unloading varying amounts of compaction are observed with frictionally strong samples showing much more compaction. Then the hold begins (100s duration) and layers continue to compact more gradually. Upon reloading the quartz and San Gregorio samples dilate as shear is reinitiated. 50 % and 100 % smectite samples exhibit very little dilation as they are reloaded.

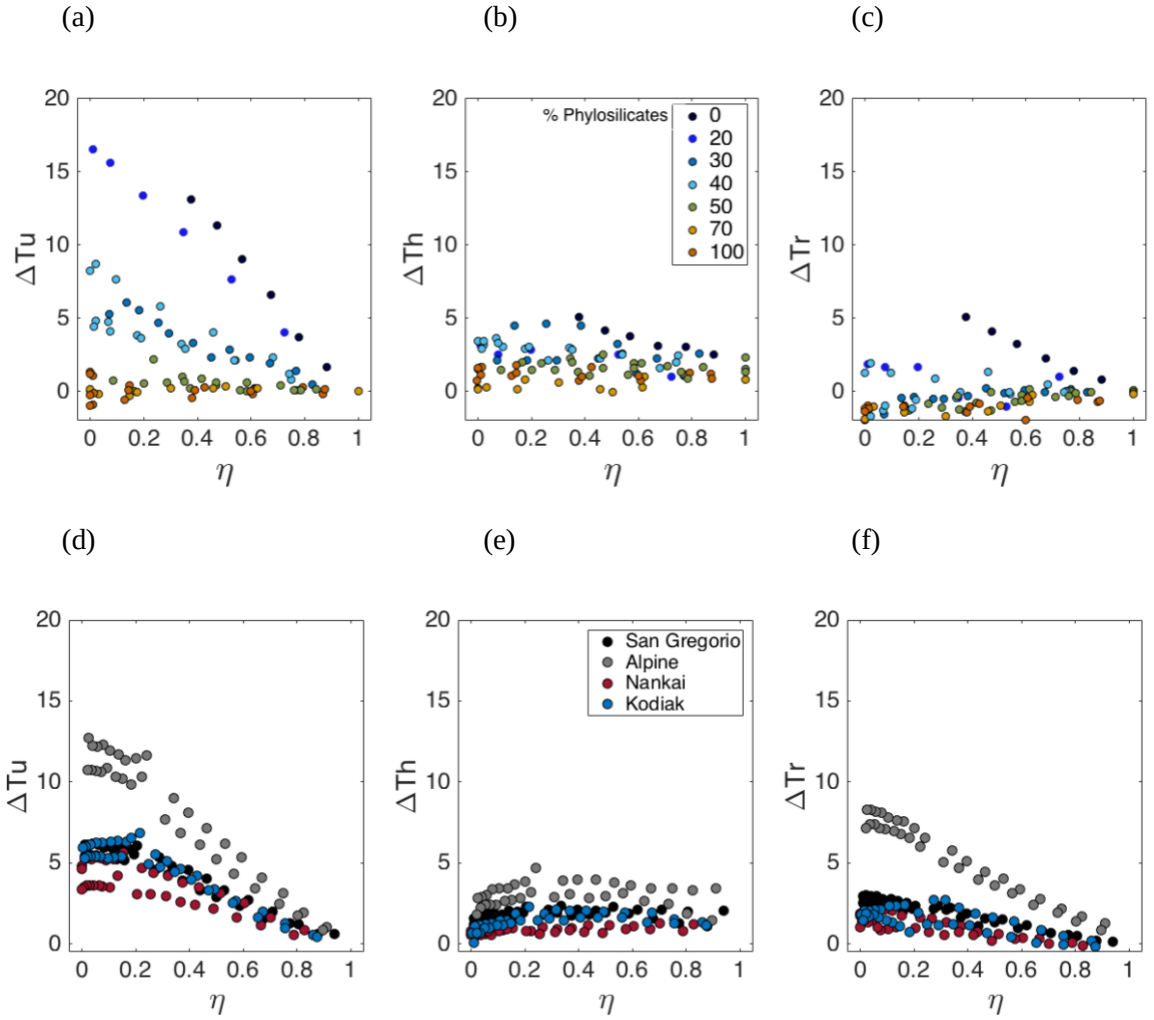

Figure 2.13:
Layer thickness changes during SHS tests. Left: Compaction during unloading. Center: compaction during the hold. Right: dilatancy during reloading.

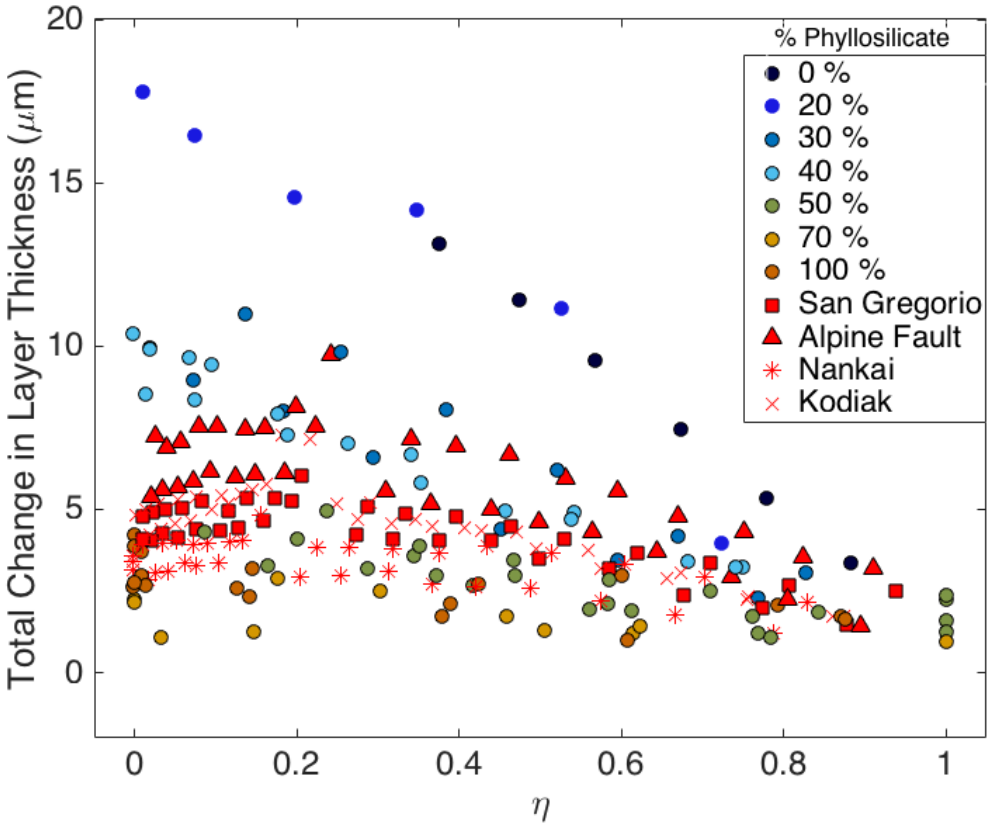

Figure 2.14:
Total change in layer thickness versus η for natural and synthetic samples. Blue-gold colors denote different synthetic gouge compositions with phyllosilicate content ranging from 0-100%. Red symbols denote natural gouge samples.

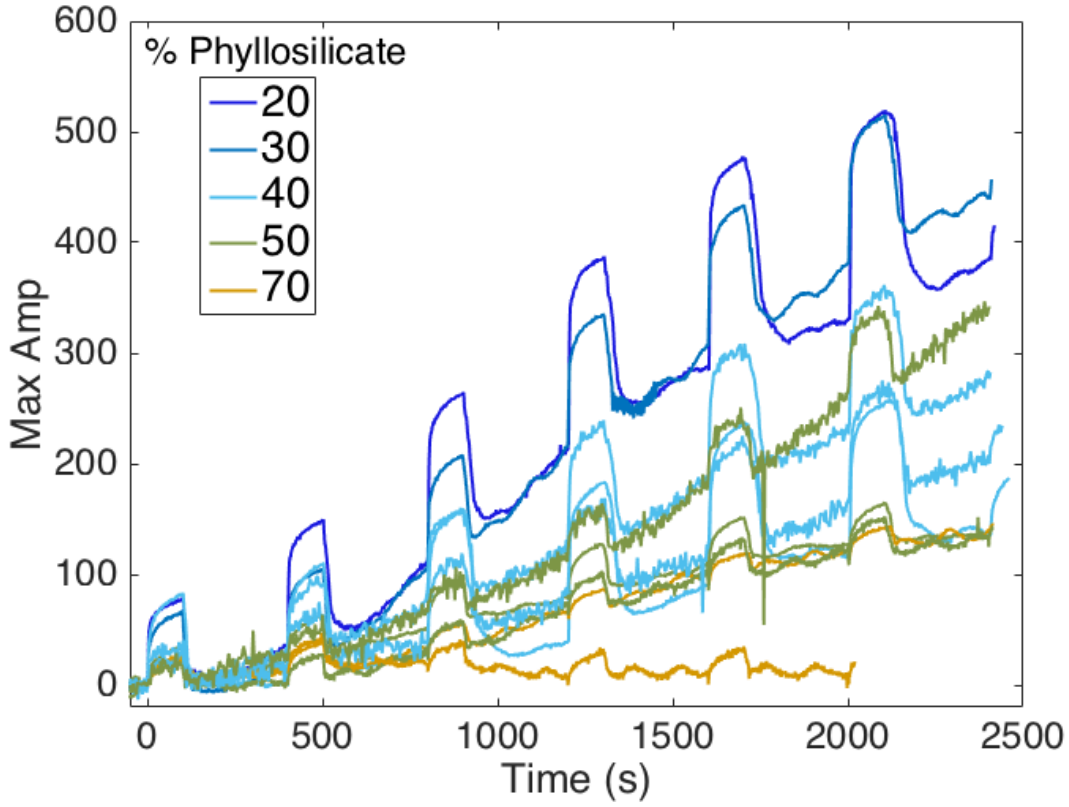

Figure 2.15:
Max amplitude during 6 SHS tests conducted on different synthetic mixtures. Amplitude corresponds to the first prominent positive peak in the selected analysis window. Change in amplitude decreases with increasing phyllosilicate content. A background increase in peak amplitude is observed during steady state shearing. The rate of increase is greater for mixtures with less phyllosilicates.

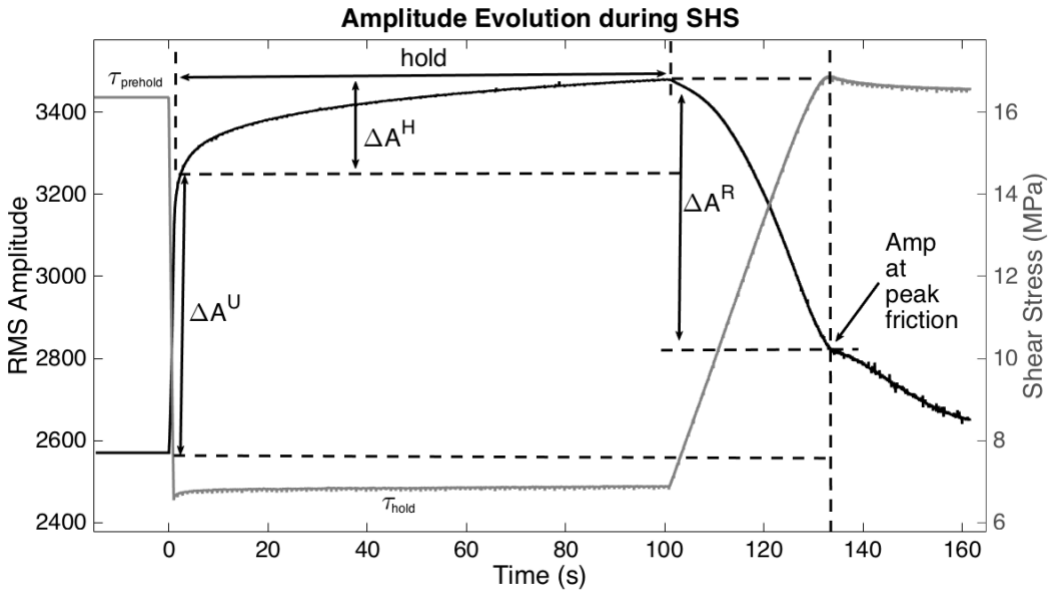

Figure 2.16:
Acoustic amplitude evolution during a SHS test in Westerly granite gouge in which η =0.42 . The amplitude here is defined as the root-mean square (RMS) average of the amplitude of the acoustic wave. Amplitude is shown in black on the left axis and the shear stress is shown in gray on the right axis. Amplitude increases dramatically during unloading and then at a more gradual rate during the hold period. Upon reloading, amplitude decreases at a rate than increases with time until just prior to the peak strength when the second derivative of amplitude vs. time passes through zero. The rate of amplitude decrease changes markedly at the peak strength. Defined are three amplitude measurements, AU, change in amplitude during unloading, AH, the change in amplitude during the hold, and AR, the change in amplitude from the onset of reloading to peak friction.

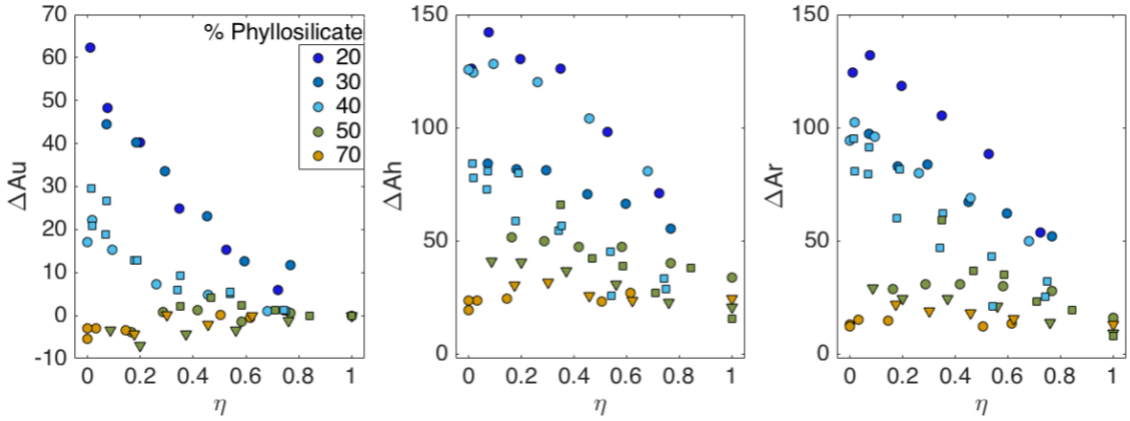

Figure 2.17:
Change in amplitude during unloading (ΔAu), during holding ((ΔAh), and during reloading (ΔAr) versus η. Changes in amplitude vary systematically with decreasing phyllosilicate content.

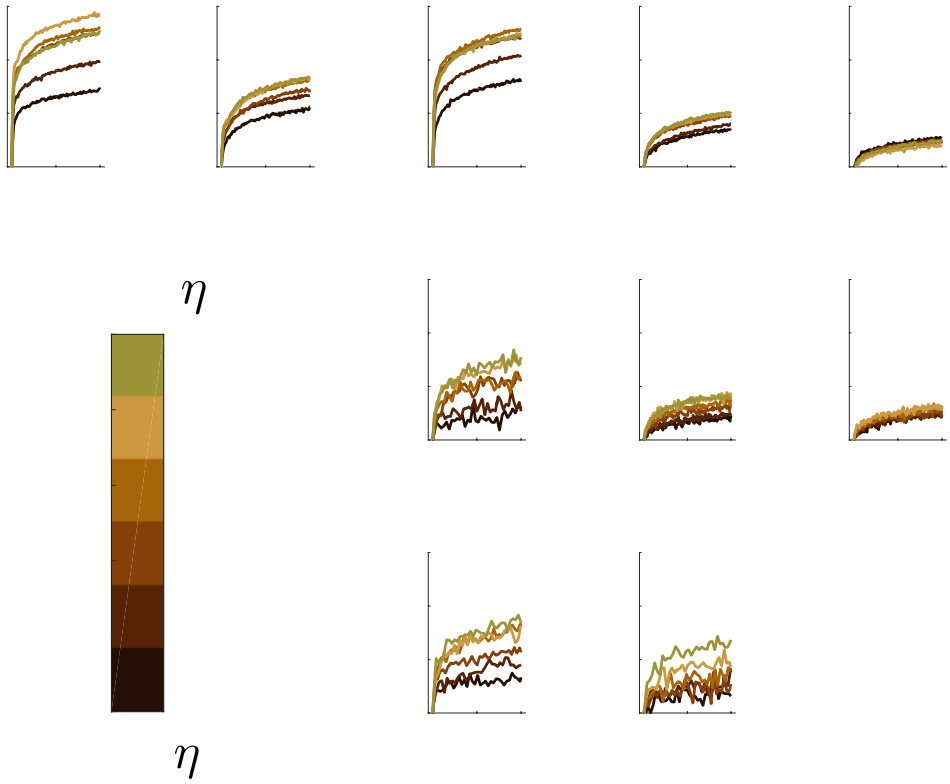

Figure 2.18:
Evolution of max amplitude during the hold period of SHS tests. Each column shows a different synthetic gouge composition. Each panel highlights SHS at different η values varying from high shear stress (dark brown) to low shear stress (gold).

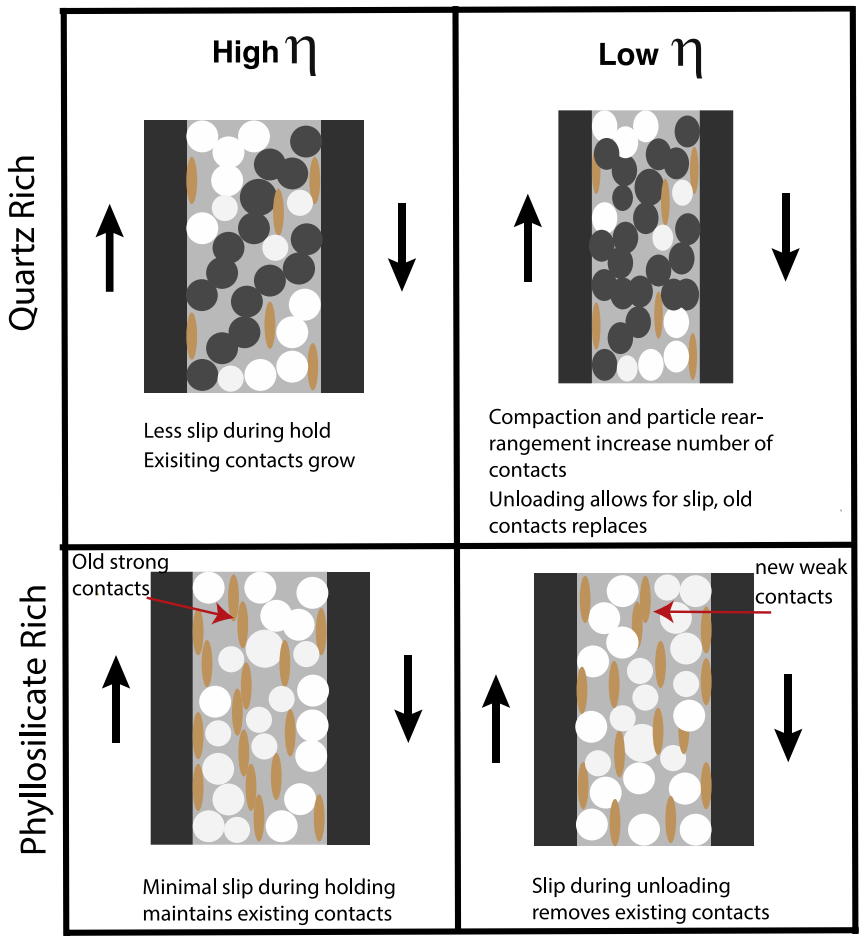

Figure 2.19:
Conceptual model for healing processes in quartz and phyllosilicate rich gouges.

Sample	Type	Location	Grain Size (μm)	Mineralogy	% Phyllosilicates
AF GC09-04 PSZ	Outcrop	Alpine Fault, New Zealand	<125	Quartz, Feldspar, Illite Minor: Chlorite, Smectite, Calcite and Muscovite	40
Kodiak SPP-06	Outcrop	Kodiak Accretionary Complex, Alaska	<125	Predominantly: Chlorite/Kaolinite, Illite, Quartz, and Feldspar	63
Nankai 190-1174B-72R-1	Borehole	Nankai Subduction Zone, Japan	<106	36% Quartz, 10% Feldspar, 10% Chlorite/Kaolinite, 10% Illite, 10% Smectite, 10% Calcite	33
San Gregorio A	Outcrop	San Gregorio Fault, California	<106	30% Smectite, 30% Feldspar, 15% Quartz, 15% Chlorite/Kaolinite, 10% Illite/Calcite	52

Table 2.1:
Description of Natural Samples

Synthetic Mixtures							
Experiment #		**% F110**	**% Smectite**	**RH %**	μ_{ss}	**η**	**Δμ**
p4538*		100	0	100	0.65	0.39-0.88	0.008-0.029
p4696		0	100	100	0.12	0-0.79	0-0.002
p4697		0	100	59	0.22	0-0.87	0-0.002
p4698		0	100	>82	0.22	0-0.88	0-0.006
p4719		50	50	100	0.34	0.16-1.00	0.001-0.004
p4720		50	50	100	0.37	0.24-1.00	0.002-0.004
p4739	F	80	20	100	0.52	0.01-0.72	0.006-0.022
p4742	F	70	30	100	0.46	0.07-0.77	0.006-0.014
p4743	F	30	70	100	0.19	0-0.61	0-0.001
p4745	F	60	40	100	0.47	0-0.68	0.006-0.011
p4961		70	30	100	0.45	0.14-1	0.004-0.006
p4963	F	30	70	100	0.20	0.18-1	0-0.002
p4964	F	50	50	100	0.25	0.09-1	0-0.003
p5111	G	60	40	62	0.48	0.02-0.75	0.006-0.012
p5112	G	60	40	62	0.49	0.013-0.74	0.007-0.010
p5113	G	50	50	60	0.41	0.35-1	0.004-0.005
* Conducted at 20 MPa			F: Flat block geometry			G: Grooved block geometry	

Natural Gouges					
Experiment #	**Sample**	**RH %**	μ_{ss}	**η**	**Δμ**
p5119	San Gregorio	100	0.50	0.01-0.94	0.009-0.054
p5120	Alpine Fault	100	0.65	0.02-0.91	0.041-0.078
p5121	Nankai	100	0.40	0-0.0.83	0-0.027
p5122	Kodiak	100	0.54	0-0.87	0.020-0.046

Table 2.2:
List of key experimental and frictional parameters

Chapter 3

Variations in Ultrasonic P-Wave Amplitude with Normal Stress and Layer Thickness: Implications for Granular Rock Friction Experiments

3.1 Abstract:

Ultrasonic waves have been used as a nondestructive method for investigating the physical and frictional properties of intact rocks and granular fault gouges for a variety of applications on the field and laboratory scale. Some studies have used ultrasonic amplitude to investigate changes in contact area during compressional and shearing experiments. However, interpretation of amplitude variation during laboratory experiments is complicated because samples experience changes in stress state and layer thickness which also influence amplitude. Limited studies have focused on systematic variations in ultrasonic amplitude with these important experimental parameters. Therefore, we investigate how ultrasonic p-wave amplitude changes with normal stress and layer thickness. We conduct a series of experiments on pure quartz samples to evaluate how amplitude changes under normal stress conditions ranging from 5-50 MPa and gouge layer thicknesses from 1-16 mm, typical conditions used during biaxial deformation experiments.

We find that amplitude varies systematically with normal stress and layer thickness. Amplitude increases with the natural logarithm of normal stress and decreases linearly with layer thickness. Using the best fitting trends to our data, we model the expected change in amplitude during laboratory slide-hold-slide (SHS) tests. We find that during the sliding portions of SHS tests, the observed amplitude variation could be described by layer thickness changes whereas during the hold section, amplitude variation is controlled by both layer thickness changes as well

as other micromechanical processes. These results are important for understanding appropriate interpretations of contact evolution during rock friction experiments.

3.2 Introduction:

Evaluating and mitigating earthquake hazards is based on an understanding of earthquake nucleation processes. Fault instabilities are governed by microscale processes that can ultimately manifest in macroscopic slip behavior. Therefore, laboratory studies play an essential role in understanding and relating small scale deformation processes to natural fault behaviors using theoretical and numerical models (Marone, 1998a).

Ultrasonic emission and active source propagation studies have been used successfully to investigate rock deformation processes including grain size reduction (Gheibi and Hedayat, 2018), microcracking (Lockner, D., 1993), stable frictional sliding (Nagata et al, 2008; Nagata et al, 2012), and stick-slip (Johnson et al, 2013; Tinti et al, 2016; Scuderi et al, 2017a). Ultrasonic waves have also been used to evaluate changes in the rock properties including bulk modulus, shear modulus and pore space (Knuth et al, 2013). Other recent studies have focused on using changes in velocity as precursors for failure in stick slip experiments (Johnson et al, 2013; Tinti et al, 2016; Scuderi et al, 2017a). A majority of these studies have focused on techniques that monitor changes in ultrasonic velocity.

Far fewer studies have investigated variations in ultrasonic amplitude (Gheibi and Hedayat, 2018). However, ultrasonic amplitude can provide unique insight into deformation processes and contact area evolution (Nagata, et al, 2008). Ultrasonic wave amplitude will vary as a function of applied stress, contact area, and sample thickness. The relationships between these

parameters are not well studied for granular fault materials and the effects of attenuation on the lab scale have primarily focused on unconsolidated soils and marine sediments (Buckingham, 1997; Oelze et al, 2002; Hefner and Williams, 2006). These studies have not explored the material compositions and stress states central to our frictional studies of fault healing.

To investigate fault healing we use laboratory slide-hold-slide (SHS) tests. SHS are a simple analog for the seismic cycle (Dieterich, 1972). The sliding represents slip along the fault, i.e. an earthquake and the hold time represents the inter-seismic period. The sample is first sheared at a constant load point velocity until a steady state is attained. Then, the load point velocity is set to zero and the hold begins. After the specified hold time, the sample is reloaded and friction increases to a peak value before the fault is able to begin sliding again. The mechanism for time dependent healing resides in the real area of contact between grains and the evolution of these contacts (Dieterich and Kilgore, 1996). For intact rocks, contact area will vary with surface roughness and in granular materials it is a function of particle angularity, size, and porosity. During shear experiments, contact area evolves with time and slip.

Our primary concern is deconvolving the portions of the signal resulting from layer thickness changes and the portion we can attribute to time and slip dependent healing that alter the material properties and frictional state of laboratory faults during SHS tests. We conduct a series of experiments to investigate amplitude variations with normal stress and layer thickness. Best fit trend lines are used to calculate the magnitude of amplitude change expected for an observed change in layer thickness measured during a SHS test experiment and compared with measured results.

3.3 Materials and Methods:

3.3.1 Mechanical Setup:

Compressional experiments were conducted on samples using three experimental configurations: (1) Flat, (2) Grooved and (3) Double Direct Shear (DDS) (Figure 3.1). For the flat and grooved configuration, a single quartz gouge layer is sandwiched between two steel blocks with embedded piezoelectric transducers. The acoustic blocks are in direct contact with the gouge layer. All sample blocks have a surface area of 10×10 cm^2. The initial gouge layer thickness is varied between 1-16mm. In the full DDS setup, two gouge layers are sandwiched between 3 steel forcing blocks. The flat acoustic blocks are then coupled to the outside of the sample assembly using molasses (Figure 3.1). Each acoustic block contains 3 piezoelectric transducers and each transducer has a different polarization (P, SV, or SH; Figure 3.1).

Samples are loaded perpendicular to the thin gouge layer and ultrasonic waves are propagated in the same direction (Figure 3.1). Normal stress is increased in increments of 5 MPa from 0 to 25 MPa and then up brought up to 50 MPa (Figure 3.2 top). For the flat and grooved configurations, the samples were also unloaded in the same step-wise manner.

3.3.2 Data Collection and Amplitude Measurements:

We probed the evolution of elastic properties during our experiments using piezoelectric transducers (PZT) with central frequency 500 kHz. One transducer transmits short pulses (half a sine cycle at 500 kHz) every 10 milliseconds throughout the experiment, while the three PZTs in the second acoustic block are used as receivers. The transmitter cycles through the 3 transmitter

PZTs (P, SV, and SH). A 14-bit acquisition system records the waveforms at 25 MHz. At each normal stress we record waveforms for 15 mins and verify that the amplitude measurements are consistent during that time. An example waveform is shown in Figure 3.2 (bottom).

To compare amplitudes throughout experiments and between experiments we had to select a metric for reporting amplitudes. We measured the peak or maximum amplitude which corresponds to the maximum amplitude in the first 3 μs (the first upward peak in the waveform; Figure 3.4). Many of the waveforms have a downward first arrival but it was not always present or greater than the background noise and, therefore, we could not reliably select it and chose to use the maximum value instead. For each experiment, the peak amplitude was measured 10 minutes after a normal stress increase.

In addition, we used different ultrasonic velocity input voltages for the three different block setups (flat, grooved, and DDS). In other words, the wave that was transmitted through the sample had a different voltage and therefore different initial amplitude. The input voltage was 14.8 V for the DDS and flat block experiments and 1.6 V for the grooved block experiments. The voltage for the grooved block experiments was reduced to prevent clipping of waveforms which was previously observed in the other configurations. Clipping occurs when the maximum amplitude in bits exceeds the range of bit values that can be recorded. To allow for comparison between configurations we conducted a calibration of input voltage with amplitude (Figure 3.3). We evaluated four different amplitude metrics as we were unsure at the time which would be most appropriate for this study. The root mean squared (RMS) amplitude was calculated over an ~3 μs that included the first two peaks. In the same time window, we select the first peak which we called the min amplitude as it was negative in polarity and the max which is positive in polarity. This is

the metric discussed in this study. We also considered the peak-to-peak amplitude which includes a full sine cycle and include the max amplitude and ends with the following trough.

For each of the three configurations we recorded peak amplitude during experiments with at least 4 different initial layer thickness. For each individual experiment we fit the amplitude as a function of the natural logarithim of normal stress with the equation:

$$\text{Amplitude} = \mathbf{C} * \mathbf{ln}(\sigma_n) + \mathbf{B}$$

where σ_n is the normal stress and C and B are the best fitting coefficients. For each configuration type and normal stress, we fit linear and exponential trends to amplitude variations with layer thickness.

Using the empirically derived trends, we calculate the maximum amplitude change expected for an observed change in layer thickness from a shearing experiment conducted on the same quartz material. The amplitude change associated with the change in layer thickness is subtracted from the observed amplitude change.

3.4 Results

3.4.1 Amplitude Variations with Input Voltage:

Four measurements of ultrasonic amplitude were reported as input voltage was increased from 1.6 V to 96.6 voltages and then reduced back to the initial value. We looked at the RMS amplitude in a 3 μs window near the first arrival, the peak to peak amplitude in that same window, the first arrival (referred to as the minimum as the), and the maximum or peak value in the selected

time window. All four amplitude measurements varied linearly over the input voltage range studied indicating that we can use any of the four amplitude measurement methods as long as the chosen method is consistently used (Figure 3.3).

3.4.2 Amplitude Variation with Normal Stress:

For the flat, grooved, and DDS configurations, we observed that amplitude increased non-linearly with normal stress (Figure 3.5). We examined several trends including linearly, logarithmic, and exponential fits and found that the amplitude was best fit by a natural logarithmic fit with normal stress. All of the trend lines can be found in Appendix B and the best fitting parameters are summarized in Table 3.2.

The flat block experiments have the highest variability in fitting parameters. The fits for experiments with initial layer thickness of 4mm and 6mm have similar C and B parameters as well as high R^2 values (>0.93) which indicates a good fit to the data. The experiments that had thicker initial layers, 8mm and 10mm respectively, had different best fit parameters. C was notably higher in the 8mm experiment and lower in the 10 mm experiment. These fits exhibited lower R^2 values of 0.76 and 0.73 respectively. The grooved block experiments showed less variability in fitting parameters. C varied from 43.3 to 57.9and B from -46.0 to 62.4. Again, we observe that the thinner layers have high R^2 values. The 16 mm thick experiment also has an anomalously high $R^{2,}$ likely due to gouge extrusion that occurred during the experiment. The 10 mm experiment had an $R^{2\ of}$ 0.71, the lowest observed in this group. Experiments using the DDS configuration had the best fit normal stress trends with R^2 >0.92 for all experiments . The parameter C varied from 315.9 to 455.5 and B varied from -526.4 to -841.2. Overall, these fits are relatively self-consistent.

3.4.3 Amplitude Variation with Layer Thickness:

For the DDS setup, we observe that peak amplitude does not vary systematically with layer thickness (Figure 3.6). For layer thickness from 1-5 mm, amplitudes increase with increasing layer thickness. Amplitude declines between experiments with initial layer thicknesses of 5mm and 10 mm. These observations are consistent at all values of normal stress. This configuration did not show a systematic trend between amplitude and layer thickness which we suspect might result from complexity of the sample geometry (which has many interfaces between the 5 steel blocks and 2 gouge layers) or as a result of coupling between the acoustic blocks and the steel forcing blocks. We continued investigating the relationship between amplitude and layer thickness with a simplified experimental setup including only one gouge layer.

In the flat block and grooved block setups with one gouge layer, we observed a systematic decrease in amplitude with increasing layer thickness (Figure 3.7). The amplitude of the ultrasonic waves transmitted through the samples varied between the two configurations. An input ultrasonic wave voltage of 14.8 V was used for the flat block experiments and a voltage of 1.6 V was used for the grooved block experiments. Best fitting linear and exponential trends are fit to the data (Figure 3.7 shows example trends at 25 MPa; Table 3 summarizes all best fitting parameters).

3.4.4 Empirical Correction of Amplitude during SHS Tests:

Based on the best fitting trends, we calculate expected changes in amplitude based solely on layer thickness changes during a frictional healing experiment. We conduct a SHS experiment

on the same quartz material used throughout this study (Figure 3.7). Throughout the experiment, layer thickness decreases due to geometric layer thinning (Scott et al, 1994). We calculate the layer thinning rate after several SHS tests. Rates varied between 0.21 and 0.48 μs/s (Figure 3.7). SHS tests are run on samples in a modified DDS configuration using a biaxial apparatus (Figure 3.8). In the modified configuration, the grooved acoustic blocks are used as the side forcing blocks such that the gouge is in direct contact with the acoustic blocks.

During each SHS test, 3 changes in amplitude are quantified (Figure 3.8). We measure A^U, the change in amplitude during unloading, A^H, the change in amplitude during the hold, and A^R, the change in amplitude from the onset of reloading to peak friction. Amplitude typically decreases as the sample is unloaded during the SHS test. During the hold period the amplitude increases as the fault is quasi-stationary contact. The amplitude then decreases as the sample is reloaded and continues to slide (Figure 3.9). We observe that during sliding between SHS tests, the amplitude decreases which is consistent with the behavior of some SHS tests in Westerly granite gouge (Figure 1.9).

During the biaxial experiment, the waveform quality was poor at 1.6 V, the voltage used for the grooved block experiments. We increased the voltage to 10 V and scaled the measured the voltage to compare with the modeled values. To reduced noise in recorded ultrasonic data, we stacked 100 waveforms throughout the experiment. We also observed some disturbances in the normal stress which are responsible for the bump in normal stress at the end of the 5^{th} and 6^{th} SHS tests (Figure 3.9)

Using the best fitting linear trends (Table 3.3), we model the amplitude change expected

from the observed change in layer thickness (Figure 3.10). Changes calculated from the best fit to the flat block experiments are greater than those expected based on the grooved block experiments. Some variation is observed between the fits of data collected as normal stress was increased/decreased. Amplitudes projected from data collected while normal stress was decreasing can be up to two times the values calculated from the normal stress increasing trends.

We compare the measured values of amplitude to the projected values from the empirical fits (Figure 3.11). The amplitude change during unloading, reloading, and the total change all indicate the observed change in amplitude is less than or equal to the value predicted from a change in layer thickness. The amplitude change during the hold is the measured value that was considerably higher than the projected amplitude values. Measured changes during the hold were 2-3 times larger than the change expected solely from layer thickness.

3.5 Discussion:

3.5.1 Normal Stress Dependence of Amplitude:

Experiments conducted in each of the 3 configurations showed a nonlinear normal stress dependence. Empirical trends with a natural logarithmic dependence were initially fit to normal stress data. To explain this behavior, we first consider a Hertzian contact model in which contact area between frictionless and adhesiveless contacts will vary as:

$$A \propto (\sigma_n)^{2/3},$$

Where A is the contact area and σ_n is normal stress (Zavarise et al, 2007; Dies et al, 2015). A comparison of this model with our data suggests that the amplitude dependence on normal stress

is in reasonable agreement with a Hertzian model when taking amplitude as a proxy for contact area during many of our experiments (Figure 3.12). In some experiments, the data at normal stresses between 5-25 MPa are well described by a model but, we notice a deviation from the model as the sample is loading to 50 MPa and as the sample is unloaded (Figure 3.12b). One explanation for this observation is that between 25 and 50 MPa considerable grain crushing may occur, altering the size of the grains in our experiments. The model assumes a certain radius of particles and does not account for a change in particle size.

3.5.2 Layer Thickness Dependence of Amplitude

Our first observation is that amplitude variations in the DDS setup did not vary systematically with layer thickness suggesting that other factors had a larger impact on attenuation in the sample. We considered the impact of relative humidity on these experiments. Relative humidity is known to influence the frictional properties of granular materials (Frye et al, 2002; Ikari et al, 2007). However, the relative humidity values during these experiments varied by < 10% and we see no systematic variation in humidity with the relative amplitudes measured in this experiment suite. In addition, the other two sample configurations were also run over a similar spread of relative humidity values. Thus, we do not think that relative humidity is the dominant factor influencing amplitude.

One consideration is that the coupling between the flat forcing acoustic blocks and the sample forcing blocks varies between experiments. Although we follow a systematic procedure when setting up samples, there is no reliable method to monitor the quality of the coupling between the acoustic blocks and the sample block. This is the only configuration we tested in which the

acoustic blocks were not in direct contact with the gouge layer. Another possibility is that the complex DDS geometry influences the transmitted amplitude due to the multiple different interfaces that the signal travels through. In the future, it would be useful to run a series of experiments using the acoustic blocks as forcing blocks in a DDS configuration. This would retain some of the complex geometry but eliminate the coupled interface to help understand if one or both of these factors largely controls the amplitude response.

The flat and grooved experiment sets show more consistent variations in amplitude with layer thickness. Laboratory friction experiments typically test gouge layers from 0-10mm. Over this relatively small range, the variation in amplitude with layer thickness is linear and amplitude decreases with increasing layer thickness. This trend is expected as more energy is lost as the ultrasonic wave travels a greater distance in the gouge layer.

3.5.3 Interpretation of Amplitude Changes During SHS Tests:

Background layer thickness thinning rates varied between 0.21 and 0.48 μs/s. Using the best fit linear trends, this can be converted to background change in amplitude rates. For a 25 MPa gouge experiment, the amplitude rates would range from 0.01-0.02 bits/s. During steady-state sliding, we do not observe this background increase in amplitude as the layer thins. Instead we observed a highly variable decrease in amplitude. It is possibly that fabric development in the gouge layer maintains the first order control on amplitude evolution during steady-state sliding. This phenomenon is currently under investigation by Kenigsberg et al, in prep. The experimental studies we conducted do not take into account the strain dependence but seek to isolate the effects of layer

thickness. It is possible that the rate of amplitude change with thickness also varies as a function of shear strain.

Comparison of the predicted amplitude changes and the measured amplitude changes shows that during sliding layer thickness change alone could explain the variation in amplitude observed. That is not to say that these processes do not contribute and are not important to frictional restrengthening, but care must be taken when interpreting these results. During holding, the measured signal exceeds the expected change suggesting that contact area growth during this time can be investigated using ultrasonic amplitude measurements.

It is worth noting that in previous chapters, we examined changes in ultrasonic amplitude during SHS and observed different background amplitude behaviors during shearing (Ch 1: bare surface Westerly granite; Ch 2: phyllosilicate materials). A better characterization of amplitude variations with thickness in different materials would be required to perform a similar analysis and understand the conditions where ultrasonic amplitude can be used as a proxy for contact area.

3.6 Conclusion

Active source ultrasonic amplitude measurements provide a valuable tool for probing deformation mechanisms in laboratory experiments. We find that amplitude varies systematically with normal stress as expected from theoretical models of Hertzian contact and elasticity. Changes in amplitude with layer thickness are well approximated by linear trends over the small range of gouge thicknesses typically used in laboratory experiments. During laboratory SHS tests, amplitude variations during the hold period may be interpreted as changes in contact area. However, caution

should be taken when considering the sliding portions as layer thickness changes alone could account for the variation in amplitude observed in our quartz experiment.

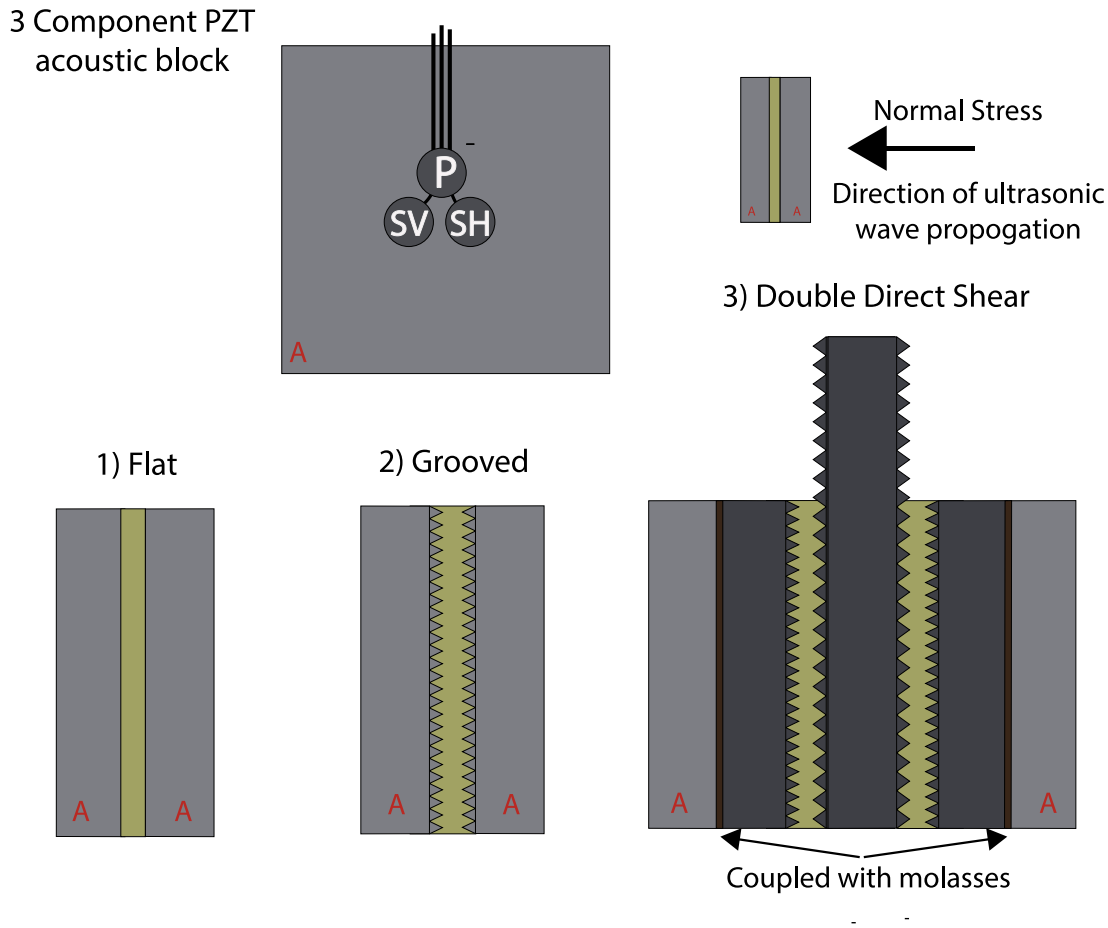

Figure 3.1:
Top left: Side view of the acoustic blocks that contain embedded piezoelectric transducers (PZTs) used to transmit and receive ultrasonic pulses Each block has 3 PZTs, one polarized in the P, SV, and SH directions. Bottom: Schematic of sample geometries and acoustic blocks used to transmit and record ultrasonic pulses. Three experimental configurations were used in this study. In the flat block configuration (1), there is a single gouge layer between two flat acoustic blocks. In the grooved block configuration (2) , there is a single gouge layer built between two grooved acoustic blocks. In geometries (1) and (2) the acoustic blocks also serve as the forcing blocks. In the double direct shear geometry (3) two gouge layers are constructed between 3 grooved forcing blocks. The flat acoustic blocks are then coupled to the outside of the sample assemblage using molasses. Top right: Show the direction of the applied normal stress and ultrasonic wave propagation.

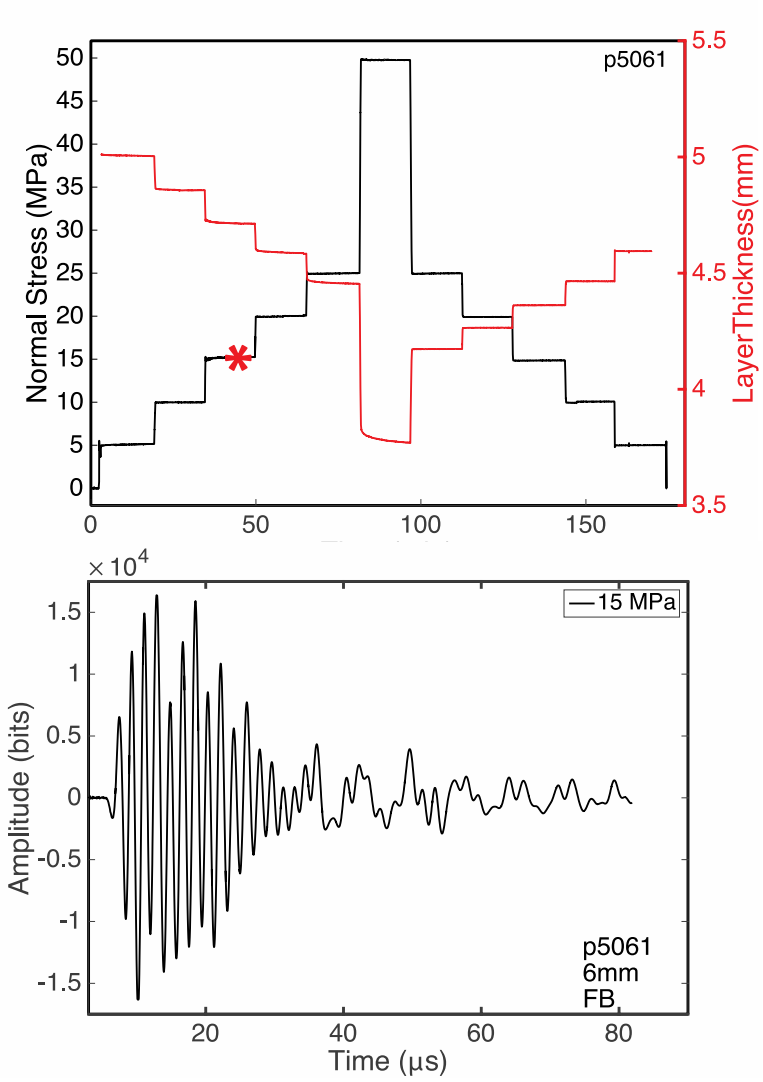

Figure 3.2:
Top: Example normal stress loading procedure and layer thickness evolution from experiment p5061. For each experiment, the normal stress was increased from 0 MPa to a maximum normal stress of 50 MPa. We recorded 15 minutes worth of acoustic measurements at each stress value. Acoustic measurements were also recorded as the normal stress was decreased. Red star indicates location of example waveform shown below.

Bottom: Example waveform from experiment p5061. Amplitudes are recorded in bits for ~80 seconds after the pulse is transmitted.

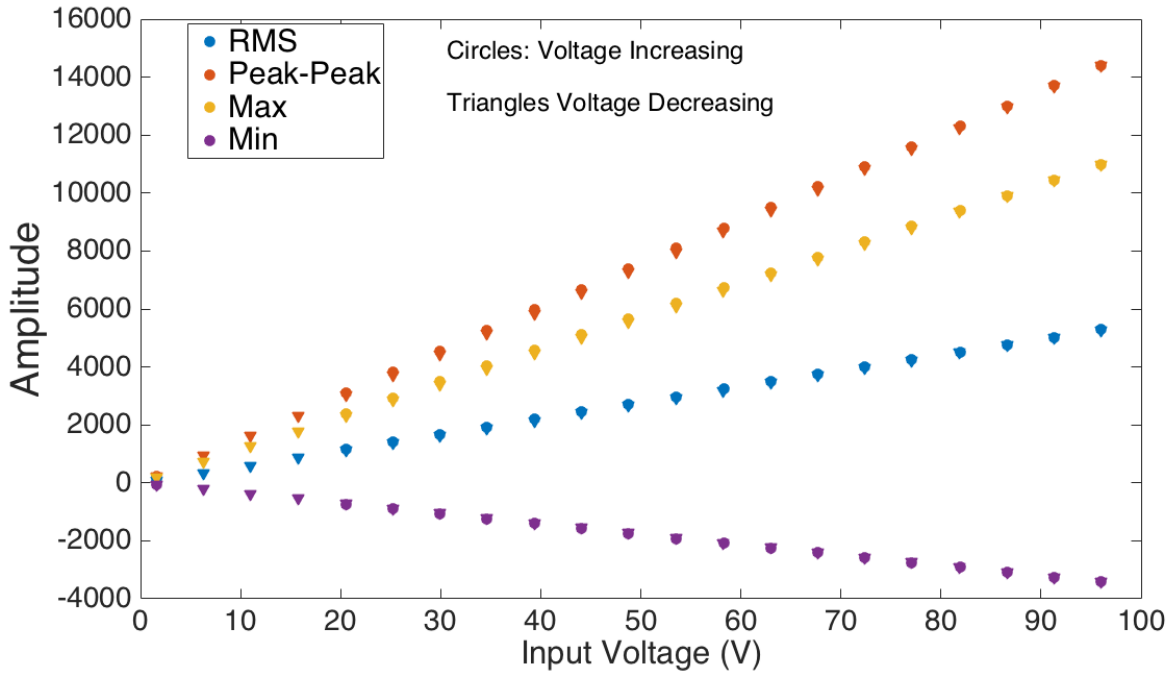

Figure 3.3:
Amplitude versus input voltage during a grooved block experiment conducted at 25 MPa on an F110 sample with initial layer thickness of 3mm. Four amplitude measurements are shown: RMS (blue), peak-to-peak (orange), first maximum (yellow) and first minimum (purple). Amplitudes were recorded as the input voltage was increased from 1.6 V to 96.6 V and then decreased back to 1.6V. All four voltage measurements vary linearly with input voltage.

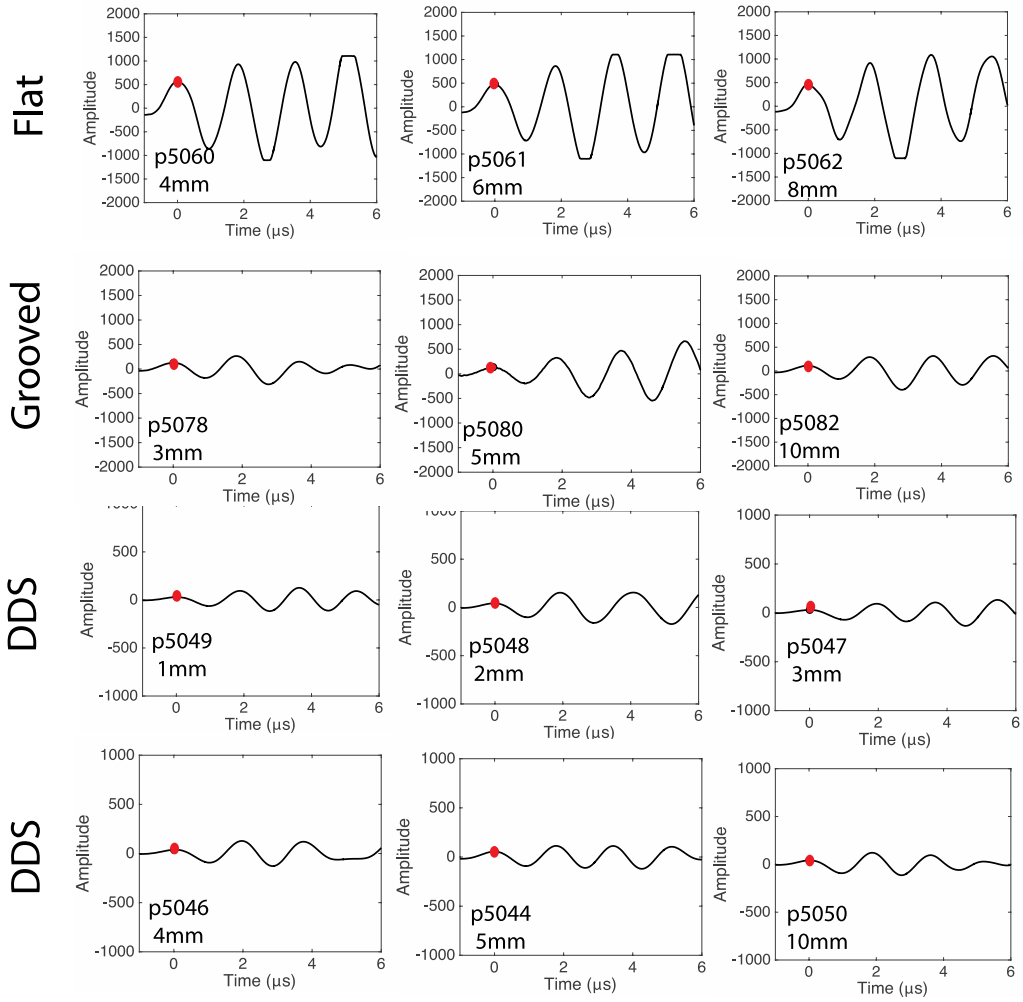

Figure 3.4:
Waveforms from experiments conducted on gouge layers of different initial thicknesses at a normal stress of 25 MPa using different sample configurations flat, grooved, and DDS. Red dots indicate the peak amplitude. Amplitudes are normalized by input voltage signal for comparison.

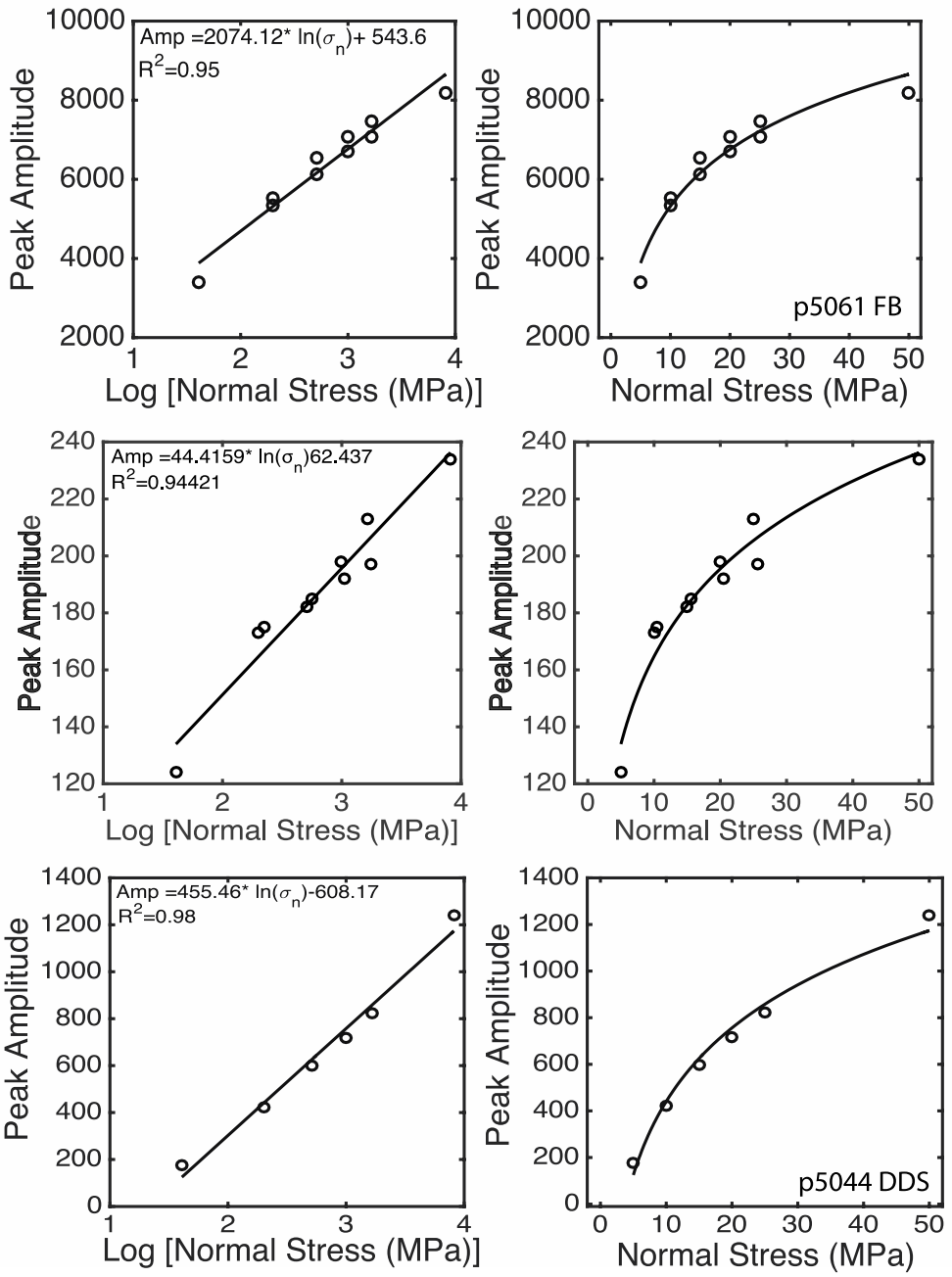

Figure 3.5:
Best logarithmic fits to peak P-wave amplitude versus normal stress for 3 example experiments (1 of each configuration type).

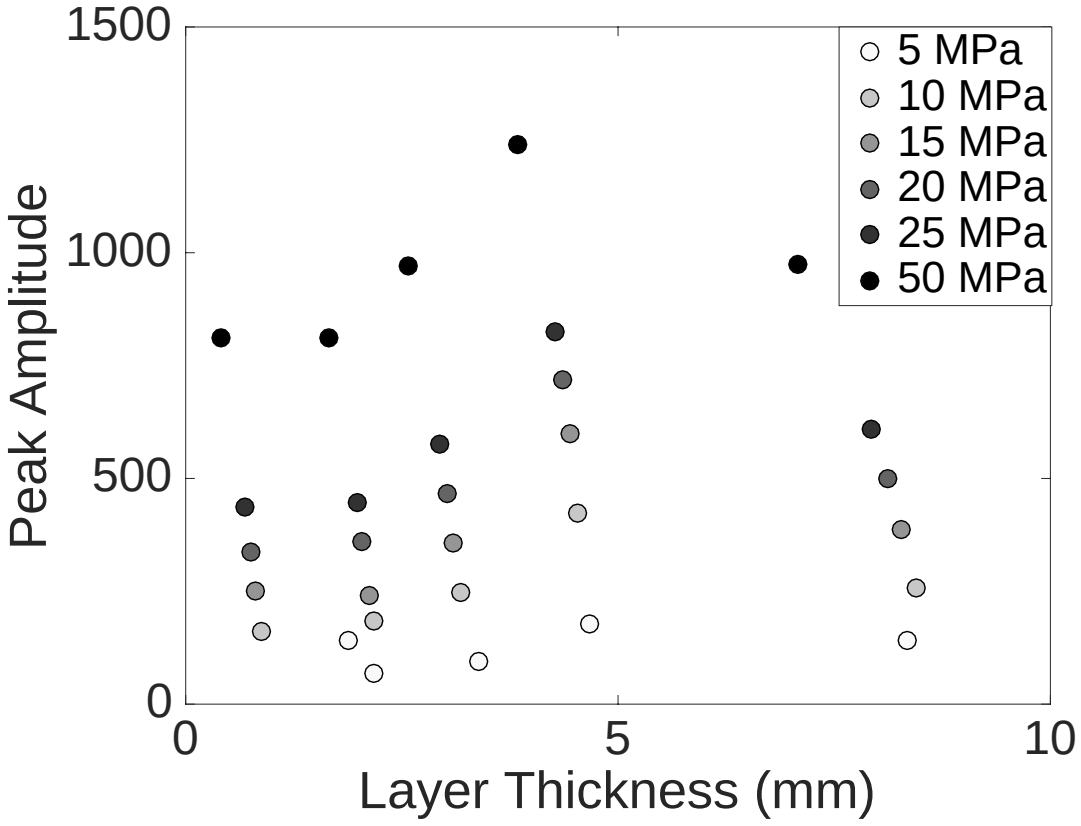

Figure 3.6:
Peak amplitude (bits) versus layer thickness (mm) for DDS experiments. A systematic trend is not observed between amplitude and layer thickness.

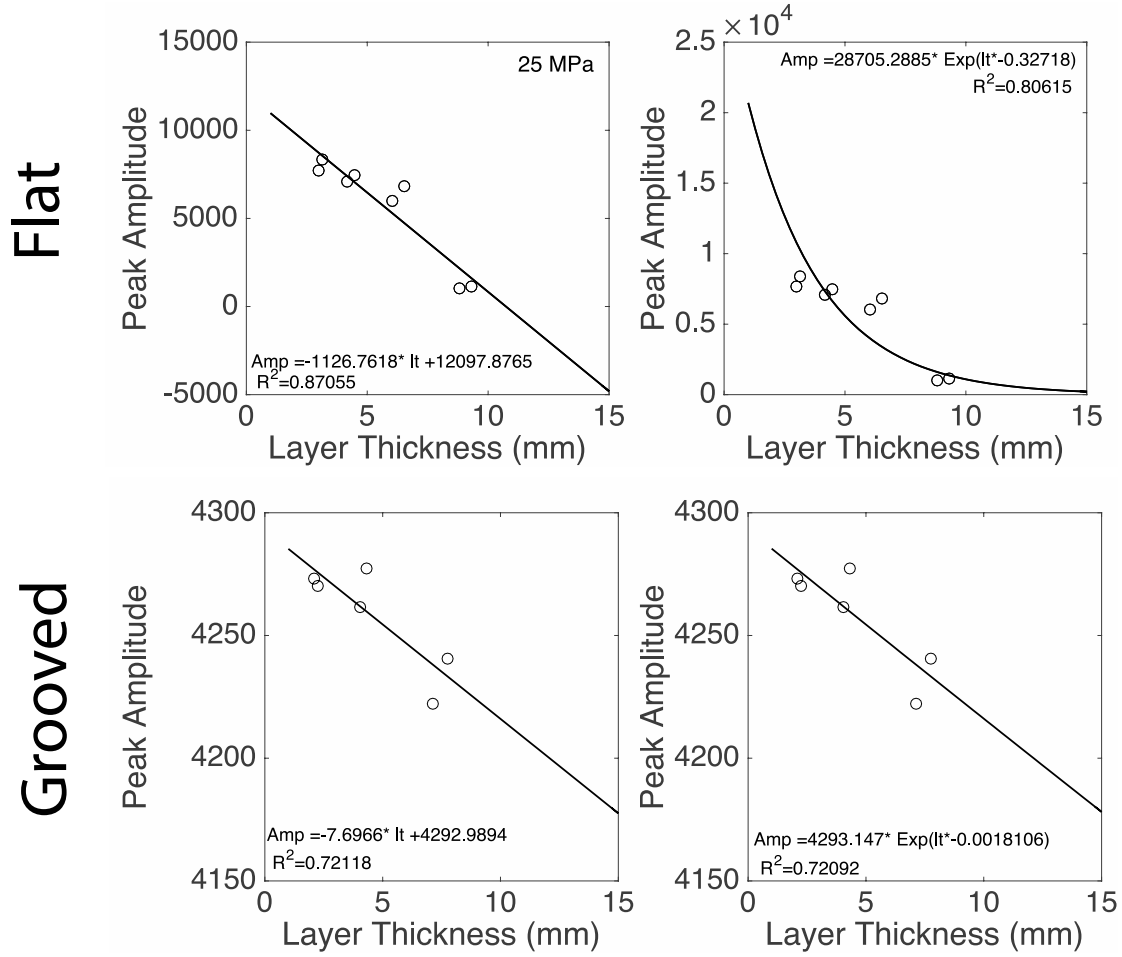

Figure 3.7:
Best logarithmic fits to peak P-wave amplitude versus normal stress for 3 example experiments (1 of each configuration type).

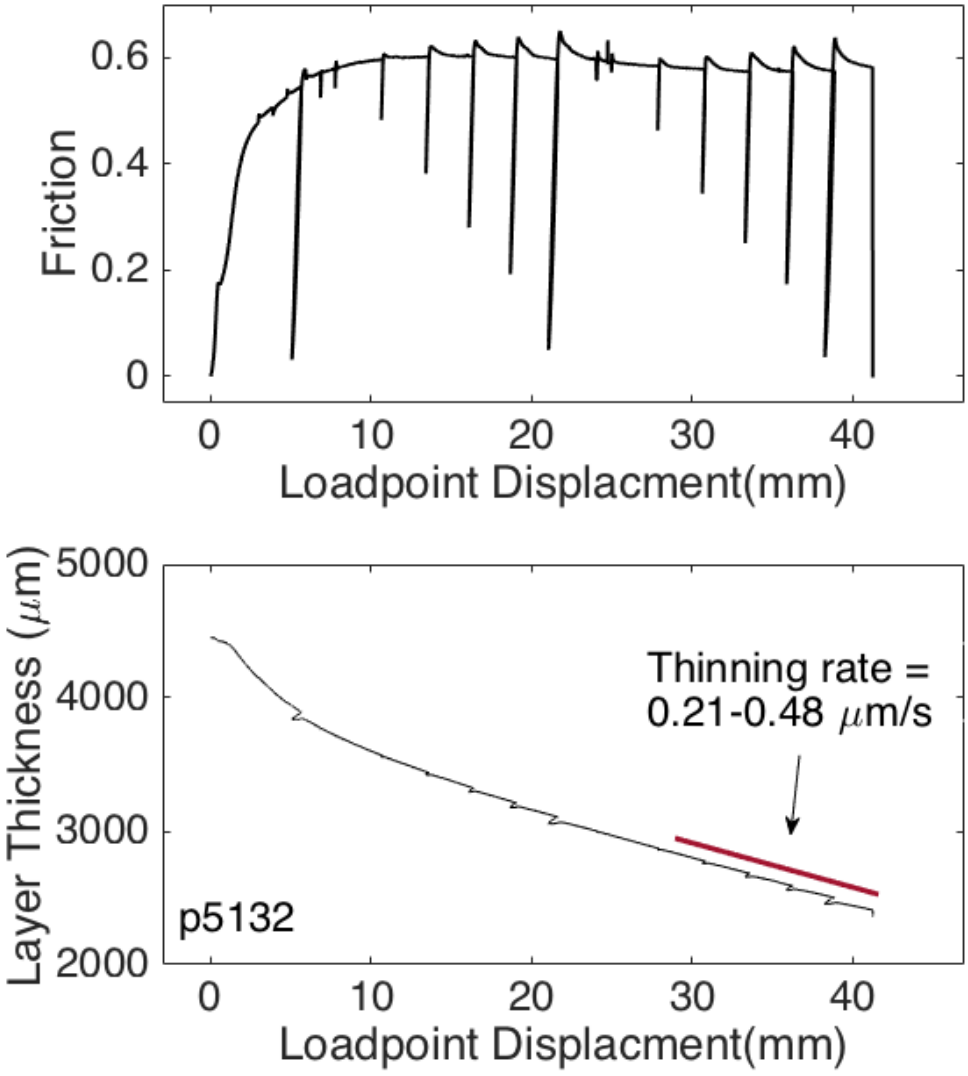

Figure 3.8:
Mechanical data from biaxial shear experiment p5132 on quartz gouge. Top: friction versus load point displacement. Over the first 10 mm we conduct velocity step tests and allow the gouge to reach a steady state value. Then we conduct a series of SHS test at different shear stress values. Bottom: Evolution of layer thickness throughout the experiment. The layer compacts during shear partially due to geometric layer thinning (Scott et al, 1994).

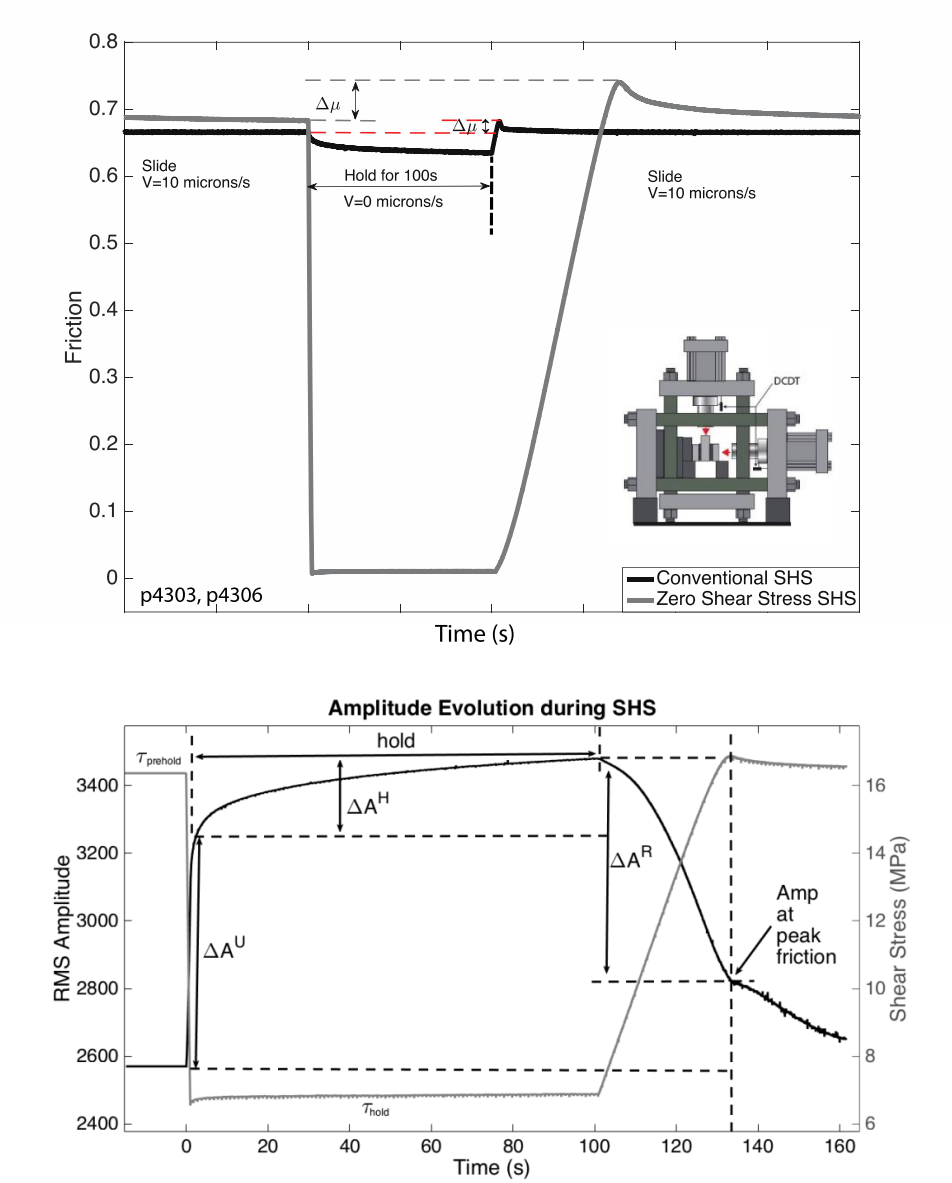

Figure 3.9:
Top: Overview of frictional response during slide-hold-slide (SHS) tests conducted in a biaxial deformation apparatus (inset from Scuderi, 2014). Shown is the frictional evolution before, during, and after a 100-second hold period. Two shear stress end member cases are shown, the conventional case where the hold begins at the steady state shear stress level (black) and the zero shear stress case where the shear stress is completely removed prior to the hold (gray).
Bottom: Example of amplitude evolution during a SHS test. Defined are three amplitude measurements, A^U, change in amplitude during unloading, A^H, the change in amplitude during the hold, and A^R, the change in amplitude from the onset of reloading to peak friction.

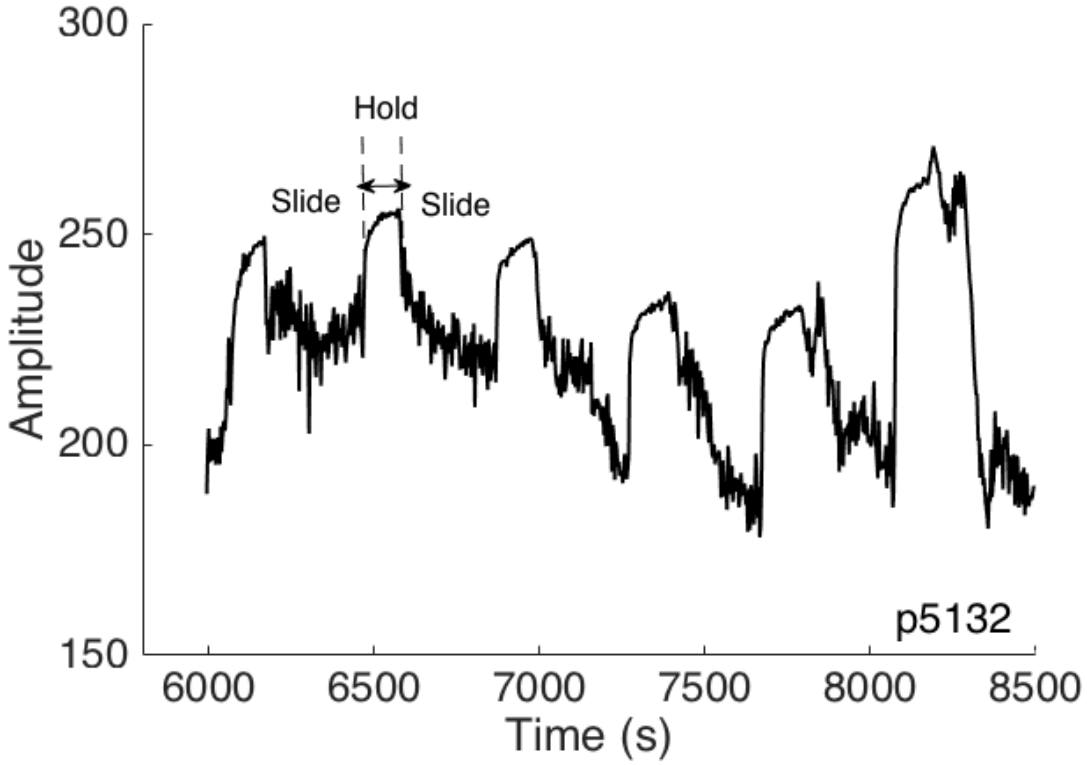

Figure 3.10:
Peak amplitude versus time during a series of 6 SHS test from experiment p5132 (corresponds to displacement of 28-40 mm in Figure 3.7). Data are relatively noisy and some SHS tests were influences by normal stress instabilities (~7800 and 8300 s) which are included in our discussion. In general, the amplitude decreases during steady state sliding periods.

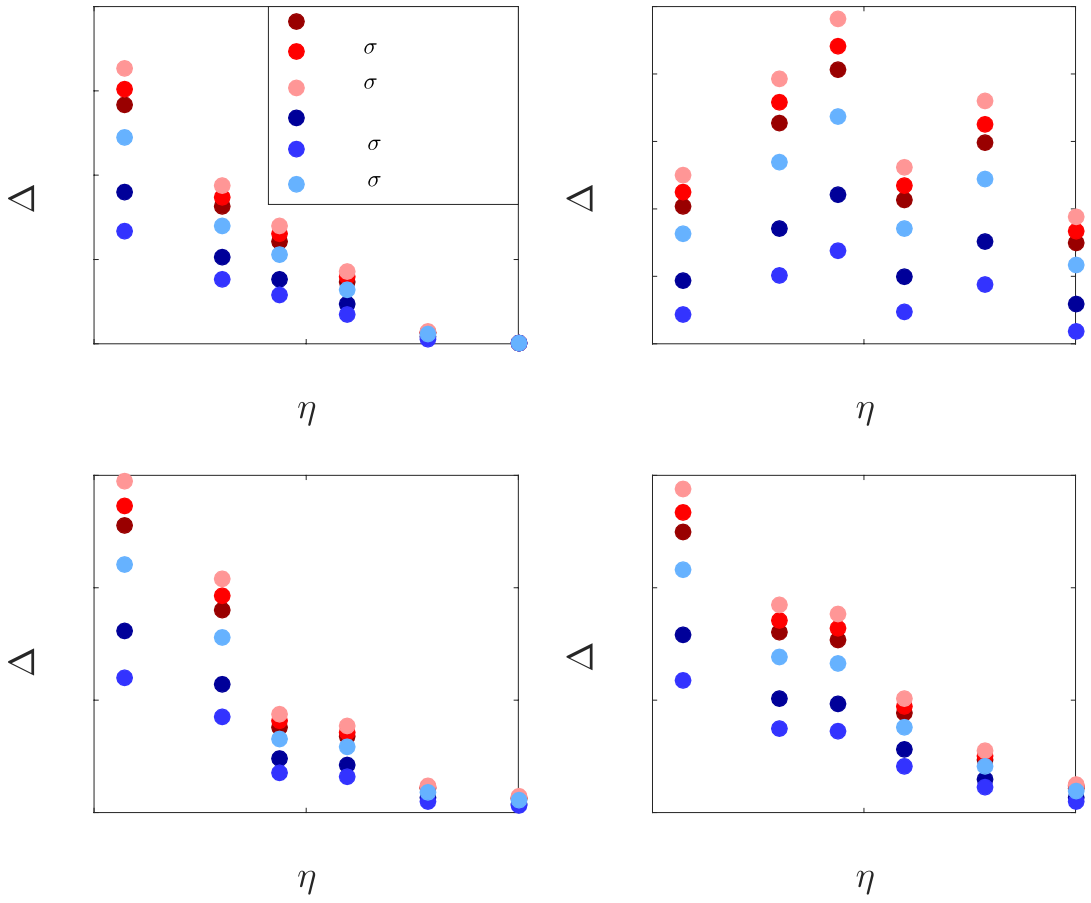

Figure 3.11:
Projected change in amplitude during each part of the SHS test (as defined in Figure 3.8). Changes in amplitude are calculated using the measured change in layer thickness from experiment p5132 and best linear fits for both flat and grooved blocks. Three trends are shown for each block type using data collected as normal stress was increased, as normal stress was decreased, and using all data (Figure 3.2). Changes calculated from the best fit to the flat block experiments are greater than those expected based on the grooved block experiments.

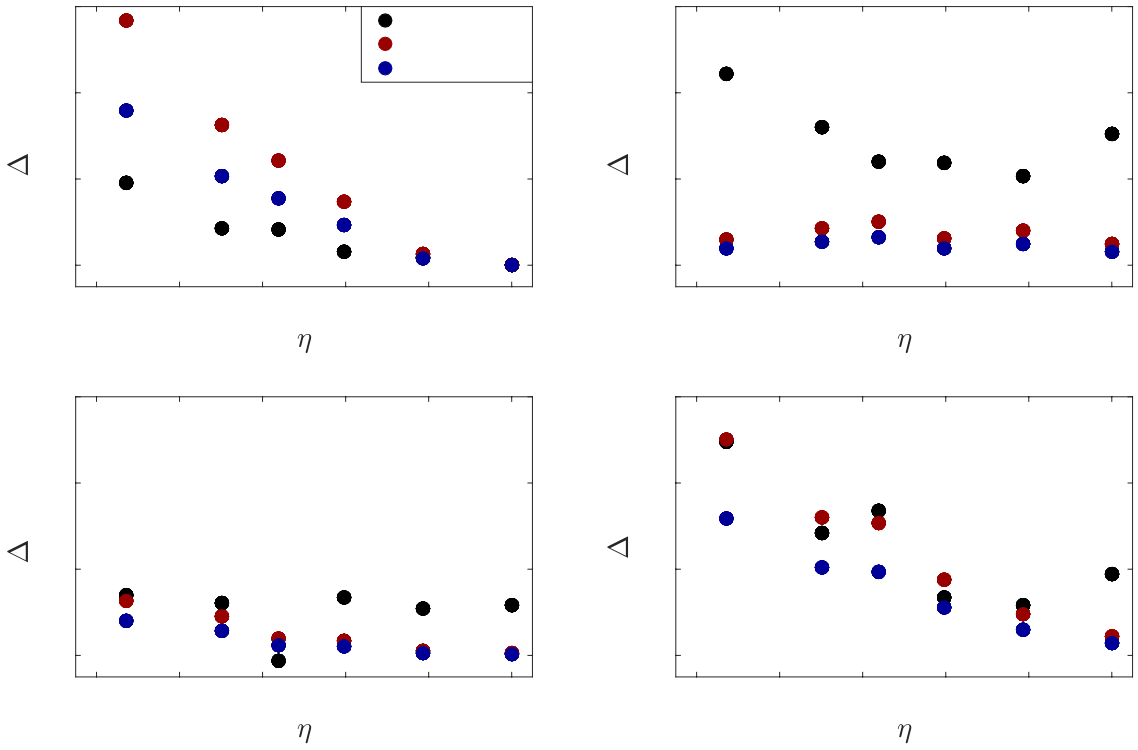

Figure 3.12:
Projected change in amplitude during each part of the SHS test (as defined in Figure 3.8). Changes in amplitude are calculated using the measured change in layer thickness from experiment p5132 and best linear fits for both flat and grooved blocks. Three trends are shown for each block type using data collected as normal stress was increased, as normal stress was decreased, and using all data (Figure 3.2). Changes calculated from the best fit to the flat block experiments are greater than those expected based on the grooved block experiments.

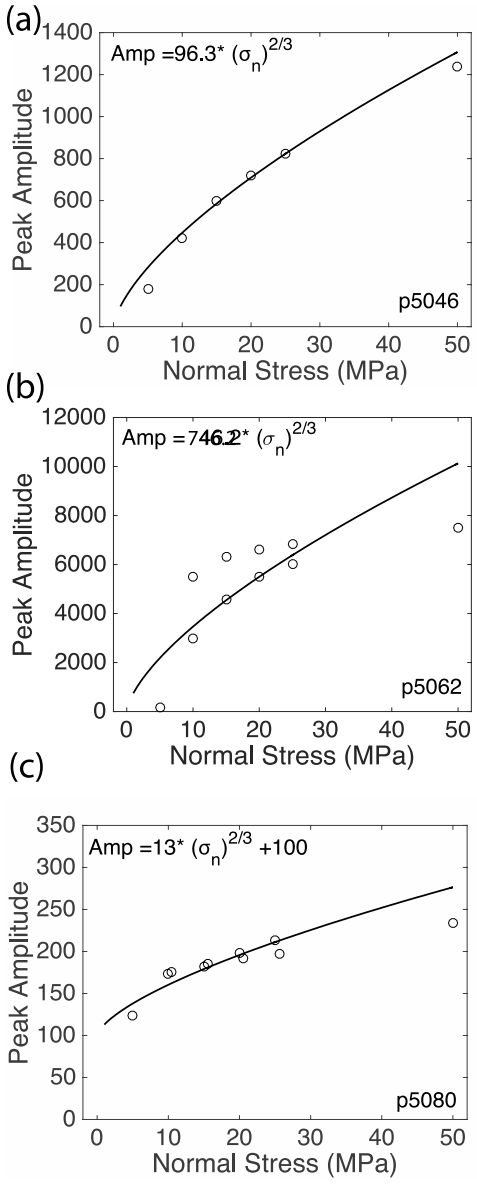

Figure 3.13:
Comparison of normal stress data from select experiment (one from each configuration type). (a) DDS experiment p5046 that shows good agreement with Hertzian model. (b) Comparison of data from FB experiment p5062 shows data collected between 5-25 MPa is reasonably fit by the model by deviates from the model at 50 MPa and as the normal stress is unloaded. (c) Grooved block experiment compared with the best fit model.

Experiment #	Configuration	Initial Layer Thickness (mm)	Normal Stress (MPa)	Ultrasonic Input Voltage (V)
p5060	Flat Block	4	0-50	14.8
p5061	Flat Block	6	0-50	14.8
p5062	Flat Block	8	0-50	14.8
p5074	Flat Block	10	0-50	14.8
p5078	Grooved Block	3	0-50	1.6
p5080	Grooved Block	5	0-50	1.6
p5082	Grooved Block	10	0-50	1.6
p5083	Grooved Block	16	0-25	1.6
p5118	Grooved Block	3	25	1.6-96.6
p5044	DDS	5	0-50	14.8
p5046	DDS	4	0-50	14.8
p5047	DDS	3	0-50	14.8
p5048	DDS	2	0-50	14.8
p5049	DDS	1	0-50	14.8
p5050	DDS	10	0-50	14.8

Table 3.1:
List of experimental parameters

Experiment #	Config.	Initial Layer Thickness (mm)	Logarithmic Fit $Amp=C*\ln(\sigma_n)+B$		R^2
			C	B	
p5074	FB	10	771.1	-1400.1	0.73
p5062	FB	8	3018.1	-3241.9	0.76
p5061	FB	6	2074.1	543.6	0.95
p5060	FB	4	2194.6	869.2	0.93
p5083	GB	16	57.9	-46.0	0.99
p5082	GB	10	43.3	27.6	0.71
p5080	GB	5	44.4	62.4	0.94
p5078	GB	3	49.1	49.8	0.96
p5050	DDS	10	361.8	-531.5	0.94
p5044	DDS	5	455.5	-608.2	0.98
p5046	DDS	4	373.7	-591.1	0.94
p5047	DDS	3	315.9	-526.4	0.92
p5048	DDS	2	375.7	-559.7	0.97
p5049	DDS	1	409.7	-841.2	0.96

Table 3.2:
Best fitting parameters for peak amplitude as a function of normal stress

	Linear Fit					
Normal Stress (MPa)	Amp=m*lt+b					
	Flat			**Grooved**		
	m	**b**	**R^2**	**m**	**b**	**R^2**
5	-622.79	5919.94	0.82	-6.28	4208.29	0.57
10	-921.40	9603.18	0.83	-7.46	4256.48	0.82
15	-1044.37	11000.75	0.84	-6.33	4263.71	0.80
20	-1099.18	11712.38	0.86	-6.59	4278.03	0.90
25	-1126.76	12097.88	0.87	-7.46	4288.94	0.81
50	-1115.65	12347.52	0.88	-10.76	4327.35	0.99
	Exponential Fit					
Normal Stress (MPa)	Amp=A*exp(lt*d)					
	Flat			**Grooved**		
	A	**d**	**R^2**	**A**	**d**	**R^2**
5	19945.67	-0.51	0.77	4208.54	-0.0015	0.57
10	65897.82	-0.56	0.79	4256.83	-0.0018	0.82
15	47207.50	-0.46	0.75	4263.92	-0.0015	0.80
20	34099.55	-0.37	0.79	4278.23	-0.0016	0.90
25	28705.29	-0.33	0.81	4289.07	-0.0018	0.81
50	19339.61	-0.23	0.83	4327.54	-0.0025	0.99

Table 3.3:
Best fitting parameters for peak amplitude as a function of layer thickness.

Bibliography

Anthony, J. L., & Marone, C. (2005). Influence of particle characteristics on granular friction. *Journal of Geophysical Research: Solid Earth*, *110*(B8).

Beeler, N. M., Tullis, T. E., & Weeks, J. D. (1994). The roles of time and displacement in the evolution effect in rock friction. *Geophysical Research Letters*, *21*(18), 1987-1990.

Behnsen, J., & Faulkner, D. R. (2012). The effect of mineralogy and effective normal stress on frictional strength of sheet silicates. *Journal of Structural Geology*, *42*, 49-61.

Bishop, A. W. (1954). The use of pore-pressure coefficients in practice. *Geotechnique*, *4*(4), 148-152.

Buckingham, M. J. (1997). Theory of acoustic attenuation, dispersion, and pulse propagation in unconsolidated granular materials including marine sediments. *The Journal of the Acoustical Society of America*, *102*(5), 2579-2596.

Brace, W. F., & Byerlee, J. D. (1966). Stick-slip as a mechanism for earthquakes. *Science*, *153*(3739), 990-992.

Byerlee, J. D., & Brace, W. F. (1968). Stick slip, stable sliding, and earthquakes—effect of rock type, pressure, strain rate, and stiffness. *Journal of Geophysical Research*, *73*(18), 6031-6037.

Carpenter, B. M., Ikari, M. J., & Marone, C. (2016). Laboratory observations of time-dependent frictional strengthening and stress relaxation in natural and synthetic fault gouges. *Journal of Geophysical Research: Solid Earth*, *121*(2), 1183-1201.

Carpenter, B. M., Saffer, D. M., & Marone, C. (2015). Frictional properties of the active San Andreas Fault at SAFOD: Implications for fault strength and slip behavior. *Journal of Geophysical Research: Solid Earth*, *120*(7), 5273-5289.

Dies, L., Restagno, F., Weil, R., Léger, L., & Poulard, C. (2015). Role of adhesion between asperities in the formation of elastic solid/solid contacts. *The European Physical Journal E*, *38*(12), 130.

Dieterich, J. H. (1972). Time-dependent friction in rocks. *Journal of Geophysical Research*, *77*(20), 3690-3697.

Dieterich, J. H. (1979). Modeling of rock friction: 1. Experimental results and constitutive equations. *Journal of Geophysical Research: Solid Earth*, *84*(B5), 2161-2168.

Dieterich, J. H. (1981). Constitutive properties of faults with simulated gouge. *Mechanical behavior of crustal rocks: the Handin volume*, 103-120.

Dieterich, J. H., & Kilgore, B. D. (1996). Imaging surface contacts: power law contact distributions and contact stresses in quartz, calcite, glass and acrylic plastic. *Tectonophysics*, *256*(1-4), 219-239.

Edmond, J. M., & Paterson, M. S. (1972). Volume changes during the deformation of rocks at high pressures. In *International Journal of Rock Mechanics and Mining Sciences & Geomechanics Abstracts* (Vol. 9, No. 2, pp. 161-182). Pergamon.

Frye, K. M., & Marone, C. (2002). Effect of humidity on granular friction at room temperature. *Journal of Geophysical Research: Solid Earth*, *107*(B11).

Gheibi, A., Slouka, S., & Hedayat, A. (2018, August). Ultrasonic investigation of friction processes in granular gouge materials. In *52nd US Rock Mechanics/Geomechanics Symposium*. American Rock Mechanics Association.

Giorgetti, C., Carpenter, B. M., & Collettini, C. (2015). Frictional behavior of talc-calcite mixtures. *Journal of Geophysical Research: Solid Earth*, *120*(9), 6614-6633.

Hefner, B. T., & Williams, K. L. (2006). Sound speed and attenuation measurements in unconsolidated glass-bead sediments saturated with viscous pore fluids. *The Journal of the Acoustical Society of America*, *120*(5), 2538-2549.

Ikari, M. J., Saffer, D. M., & Marone, C. (2007). Effect of hydration state on the frictional properties of montmorillonite-based fault gouge. *Journal of Geophysical Research: Solid Earth*, *112*(B6).

Johnson, P. A., Carpenter, B., Knuth, M., Kaproth, B. M., Le Bas, P. Y., Daub, E. G., & Marone, C. (2012). Nonlinear dynamical triggering of slow slip on simulated earthquake faults with implications to Earth. *Journal of Geophysical Research: Solid Earth*, *117*(B4).

Johnson, P. A., Ferdowsi, B., Kaproth, B. M., Scuderi, M., Griffa, M., Carmeliet, J., & Marone, C. (2013). Acoustic emission and microslip precursors to stick-slip failure in sheared granular material. *Geophysical Research Letters*, *40*(21), 5627-5631.

Kaproth, B. M., & Marone, C. (2013). Slow earthquakes, preseismic velocity changes, and the origin of slow frictional stick-slip. *Science*, *341*(6151), 1229-1232.

Karner, S. L., & Marone, C. (1998). The effect of shear load on frictional healing in simulated fault gouge. *Geophysical research letters*, *25*(24), 4561-4564.

Karner, S. L., & Marone, C. (2001). Fractional restrengthening in simulated fault gouge: Effect of shear load perturbations. *Journal of Geophysical Research: Solid Earth*, *106*(B9), 19319-19337.

Knuth, M. W., Tobin, H. J., & Marone, C. (2013). Evolution of ultrasonic velocity and dynamic elastic moduli with shear strain in granular layers. *Granular Matter*, *15*(5), 499-515.

Leeman, J. R., Saffer, D. M., Scuderi, M. M., & Marone, C. (2016). Laboratory observations of slow earthquakes and the spectrum of tectonic fault slip modes. *Nature communications*, *7*, 11104.

Li, Y. G., Vidale, J. E., Day, S. M., Oglesby, D. D., & Cochran, E. (2003). Postseismic fault healing on the rupture zone of the 1999 M 7.1 Hector Mine, California, earthquake. *Bulletin of the Seismological Society of America*, *93*(2), 854-869.

Lockner, D. (1993, December). The role of acoustic emission in the study of rock fracture. In *International Journal of Rock Mechanics and Mining Sciences & Geomechanics Abstracts*(Vol. 30, No. 7, pp. 883-899). Pergamon.

Logan, J. M., Dengo, C. A., Higgs, N. G., & Wang, Z. Z. (1992). Fabrics of experimental fault zones: Their development and relationship to mechanical behavior. In *International Geophysics* (Vol. 51, pp. 33-67). Academic Press.

Lupini, J. F., Skinner, A. E., & Vaughan, P. R. (1981). The drained residual strength of cohesive soils. *Geotechnique*, *31*(2), 181-213.

Marone, C. (1998a). Laboratory-derived friction laws and their application to seismic faulting. *Annual Review of Earth and Planetary Sciences*, *26*(1), 643-696.

Marone, C. (1998b). The effect of loading rate on static friction and the rate of fault healing during the earthquake cycle. *Nature*, *391*(6662), 69.

Marone, C., Raleigh, C. B., & Scholz, C. H. (1990). Frictional behavior and constitutive modeling of simulated fault gouge. *Journal of Geophysical Research: Solid Earth*, *95*(B5), 7007-7025.

Marone, C., & Scholz, C. H. (1989). Particle-size distribution and microstructures within simulated fault gouge. *Journal of Structural Geology*, *11*(7), 799-814.

Marone, C., Vidale, J. E., & Ellsworth, W. L. (1995). Fault healing inferred from time dependent variations in source properties of repeating earthquakes. *Geophysical Research Letters*, *22*(22), 3095-3098.

McLaskey, G. C., Thomas, A. M., Glaser, S. D., & Nadeau, R. M. (2012). Fault healing promotes high-frequency earthquakes in laboratory experiments and on natural faults. *Nature*, *491*(7422), 101.

Muhuri, S. K., Dewers, T. A., Scott Jr, T. E., & Reches, Z. E. (2003). Interseismic fault strengthening and earthquake-slip instability: Friction or cohesion?. *Geology*, *31*(10), 881-884.

Nagata, K., Nakatani, M., & Yoshida, S. (2008). Monitoring frictional strength with acoustic wave transmission. *Geophysical Research Letters*, *35*(6).

Nagata, K., Nakatani, M., & Yoshida, S. (2012). A revised rate-and state-dependent friction law obtained by constraining constitutive and evolution laws separately with laboratory data. *Journal of Geophysical Research: Solid Earth*, *117*(B2).

Nakatani, M., & Mochizuki, H. (1996). Effects of shear stress applied to surfaces in stationary contact on rock friction. *Geophysical research letters*, *23*(8), 869-872.

Niemeijer, A. R., & Spiers, C. J. (2006). Velocity dependence of strength and healing behaviour in simulated phyllosilicate-bearing fault gouge. *Tectonophysics*, *427*(1-4), 231-253.

Niemeijer, A. R., Spiers, C. J., & Bos, B. (2002). Compaction creep of quartz sand at 400–600 C: Experimental evidence for dissolution-controlled pressure solution. *Earth and Planetary Science Letters*, *195*(3-4), 261-275.

Oelze, M. L., O'Brien, W. D., & Darmody, R. G. (2002). Measurement of attenuation and speed of sound in soils. *Soil Science Society of America Journal*, *66*(3), 788-796.

Peng, Z., Vidale, J. E., Marone, C., & Rubin, A. (2005). Systematic variations in recurrence interval and moment of repeating aftershocks. *Geophysical research letters*, *32*(15).

Pyrak-Nolte, L. J., Myer, L. R., & Cook, N. G. (1990). Transmission of seismic waves across single natural fractures. *Journal of Geophysical Research: Solid Earth*, *95*(B6), 8617-8638.

Rathbun, A. P., Renard, F., & Abe, S. (2013). Numerical investigation of the interplay between wall geometry and friction in granular fault gouge. *Journal of Geophysical Research: Solid Earth*, *118*(3), 878-896.

Rice, J. R., & Ruina, A. L. (1983). Stability of steady frictional slipping. *Journal of applied mechanics*, *50*(2), 343-349.

Ruina, A. (1983). Slip instability and state variable friction laws. *Journal of Geophysical Research: Solid Earth*, *88*(B12), 10359-10370.

Saffer, D. M., & Marone, C. (2003). Comparison of smectite-and illite-rich gouge frictional properties: application to the updip limit of the seismogenic zone along subduction megathrusts. *Earth and Planetary Science Letters*, *215*(1-2), 219-235.

Scholz, C. H. (2002). *The mechanics of earthquakes and faulting*. Cambridge university press.

Scholz, C. H., Aviles, C. A., & Wesnousky, S. G. (1986). Scaling differences between large interplate and intraplate earthquakes. *Bulletin of the Seismological Society of America*, *76*(1), 65-70.

Scholz, C., Molnar, P., & Johnson, T. (1972). Detailed studies of frictional sliding of granite and implications for the earthquake mechanism. *Journal of geophysical research*, *77*(32), 6392-6406.

Scott, D. R., Marone, C. J., & Sammis, C. G. (1994). The apparent friction of granular fault gouge in sheared layers. *Journal of Geophysical Research: Solid Earth*, *99*(B4), 7231-7246.

Scuderi, M. M., Carpenter, B. M., & Marone, C. (2014). Physicochemical processes of frictional healing: Effects of water on stick‐slip stress drop and friction of granular fault gouge. Journal of Geophysical Research: Solid Earth, 119(5), 4090-4105.

Scuderi, M. M., Collettini, C., & Marone, C. (2017a). Frictional stability and earthquake triggering during fluid pressure stimulation of an experimental fault. *Earth and Planetary Science Letters*, *477*, 84-96.

Scuderi, M. M., Collettini, C., Viti, C., Tinti, E., & Marone, C. (2017b). Evolution of shear fabric in granular fault gouge from stable sliding to stick slip and implications for fault slip mode. *Geology*, *45*(8), 731-734.

Steurer, J. F., & Underwood, M. B. (2003). Clay mineralogy of mudstones from the Nankai Trough reference Sites 1173 and 1177 and frontal accretionary prism Site 1174. In *Proc. ODP, Sci. Results* (Vol. 190, No. 196, pp. 1-37).

Tadokoro, K., & Ando, M. (2002). Evidence for rapid fault healing derived from temporal changes in S wave splitting. *Geophysical Research Letters*, *29*(4).

Tembe, S., Lockner, D. A., & Wong, T. F. (2010). Effect of clay content and mineralogy on frictional sliding behavior of simulated gouges: Binary and ternary mixtures of quartz, illite, and montmorillonite. *Journal of Geophysical Research: Solid Earth*, *115*(B3).

Tenthorey, E., Cox, S. F., & Todd, H. F. (2003). Evolution of strength recovery and permeability during fluid–rock reaction in experimental fault zones. *Earth and Planetary Science Letters*, *206*(1-2), 161-172.

Tesei, T., Collettini, C., Carpenter, B. M., Viti, C., & Marone, C. (2012). Frictional strength and healing behavior of phyllosilicate-rich faults. *Journal of Geophysical Research: Solid Earth*, *117*(B9).

Tian, K., Gosvami, N. N., Goldsby, D. L., Liu, Y., Szlufarska, I., & Carpick, R. W. (2017). Load and Time Dependence of Interfacial Chemical Bond-Induced Friction at the Nanoscale. *Physical review letters*, *118*(7), 076103.

Tinti, E., Scuderi, M. M., Scognamiglio, L., Di Stefano, G., Marone, C., & Collettini, C. (2016). On the evolution of elastic properties during laboratory stick-slip experiments spanning the transition from slow slip to dynamic rupture. *Journal of Geophysical Research: Solid Earth*, *121*(12), 8569-8594.

Tullis, T. E., & Weeks, J. D. (1986). Constitutive behavior and stability of frictional sliding of granite. *Pure and Applied Geophysics*, *124*(3), 383-414.

Vidale, J. E., ElIsworth, W. L., Cole, A., & Marone, C. (1994). Variations in rupture process with recurrence interval in a repeated small earthquake. *Nature*, *368*(6472), 624.

Zavarise, G., Borri-Brunetto, M., & Paggi, M. (2007). On the resolution dependence of micromechanical contact models. *Wear*, *262*(1-2), 42-54.

Zhu, W., & Wong, T. F. (1997). The transition from brittle faulting to cataclastic flow: Permeability evolution. *Journal of Geophysical Research: Solid Earth*, *102*(B2), 3027-3041.

Acknowledgements: This material is based upon work supported by NSF-EAR1520760, DE-EE0006762, and a CSES grant from LANL. Any opinions, findings, and conclusions or recommendations expressed in this publication are those of the author(s) and do not necessarily reflect the views of the National Science Foundation or the U.S. Department of Energy.

Appendix A

Chapter 1 Supplementary Material

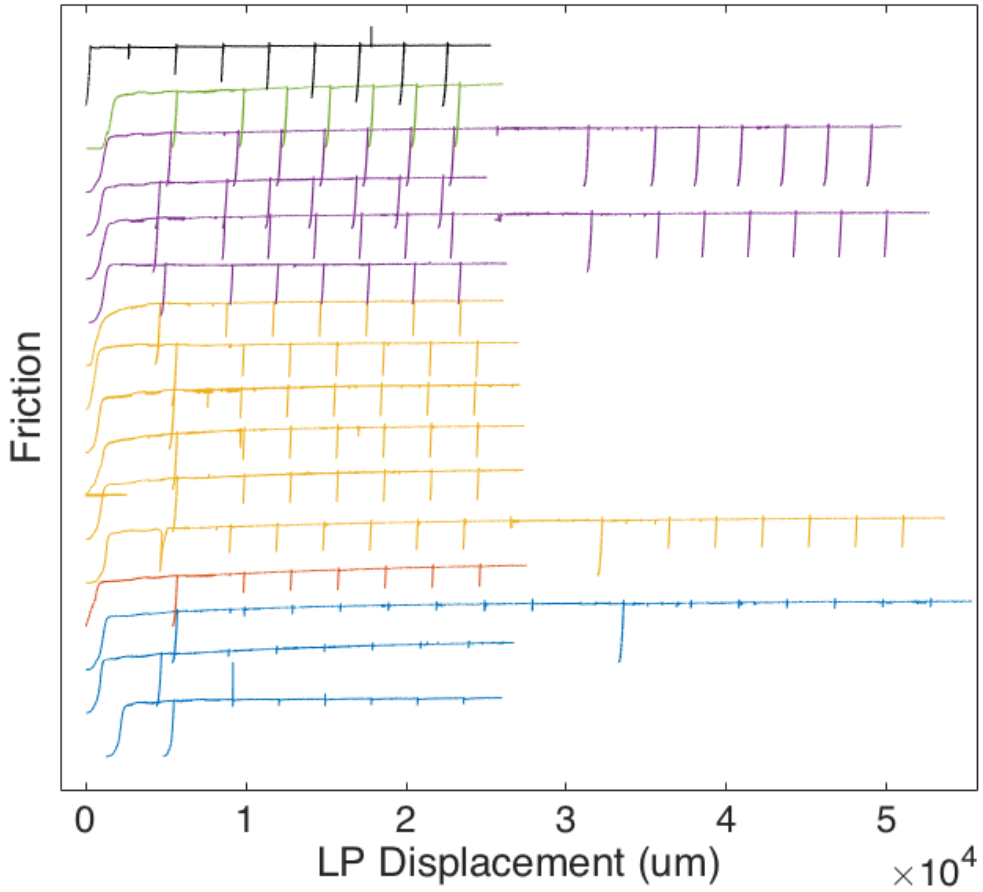

Figure A1. Friction versus load point displacement for full experiment runs in Westerly granite bare surfaces. Colors depict different ranges of eta values with eta increasing from top to bottom. The black experiment shown on top has different eta values throughout the experiment.

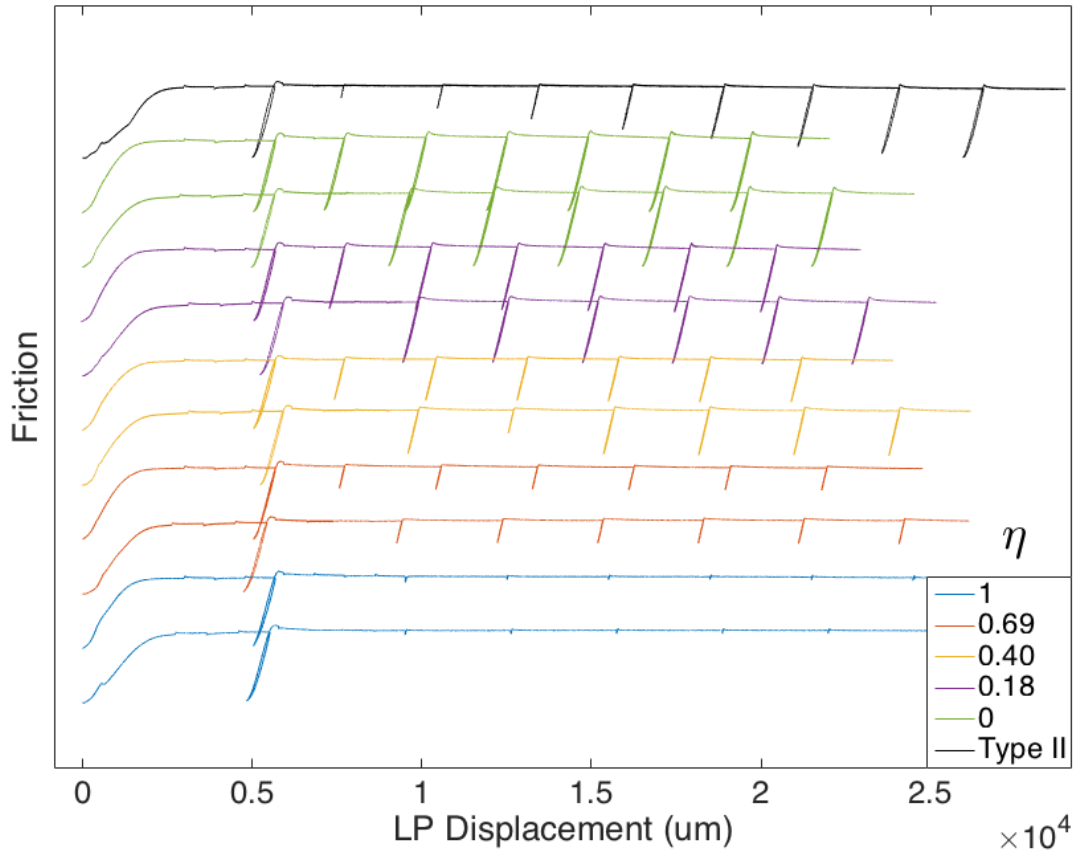

Figure A2. Friction versus load point displacement for full experiment runs in Westerly granite gouge. Colors depict different ranges of eta values with eta increasing from top to bottom. The black line shown on top has different eta values throughout the experiment.

Appendix B

Chapter 3 Supplementary Material

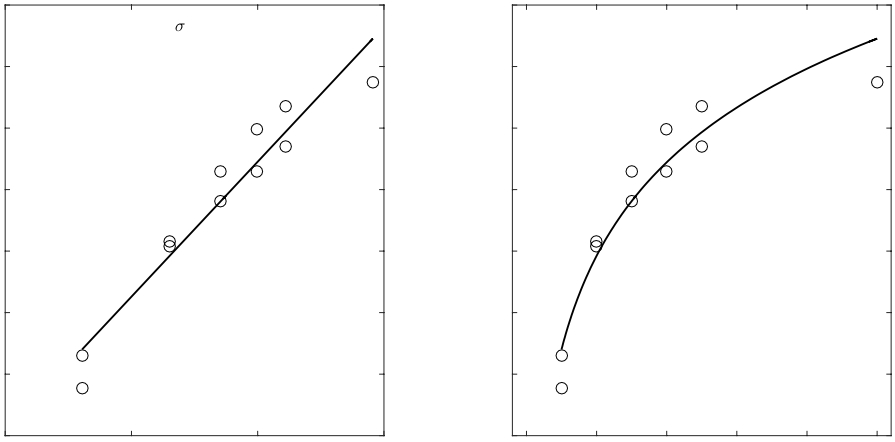

Figure B1:
Best logarithmic fit to peak amplitude versus normal stress for experiment p5060 with initial layer thickness of 4 mm using the flat block configuration.

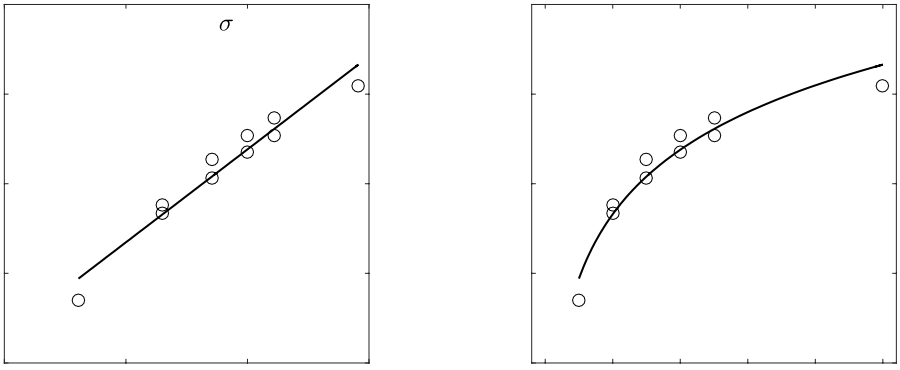

Figure B2:
Best logarithmic fit to peak amplitude versus normal stress for experiment p5061 with initial layer thickness of 6 mm using the flat block configuration.

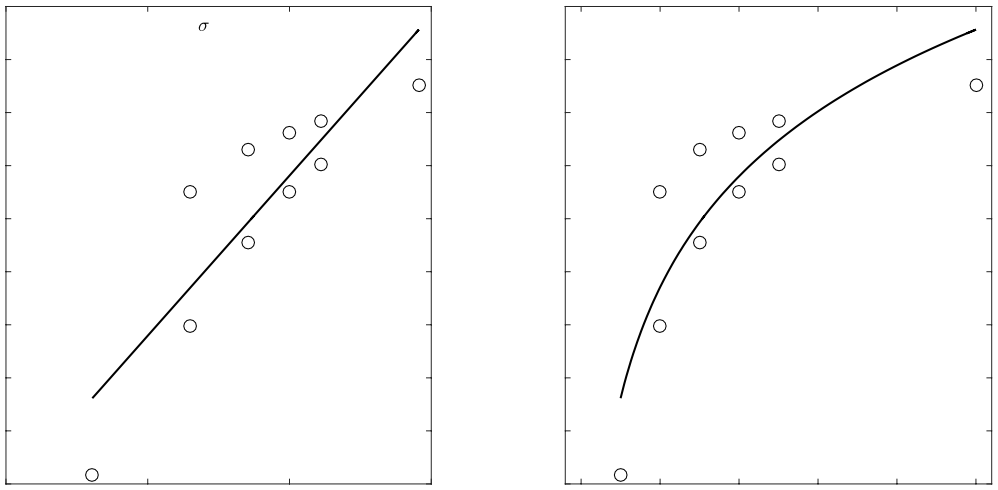

Figure B3:
Best logarithmic fit to peak amplitude versus normal stress for experiment p5062 with initial layer thickness of 8 mm using the flat block configuration.

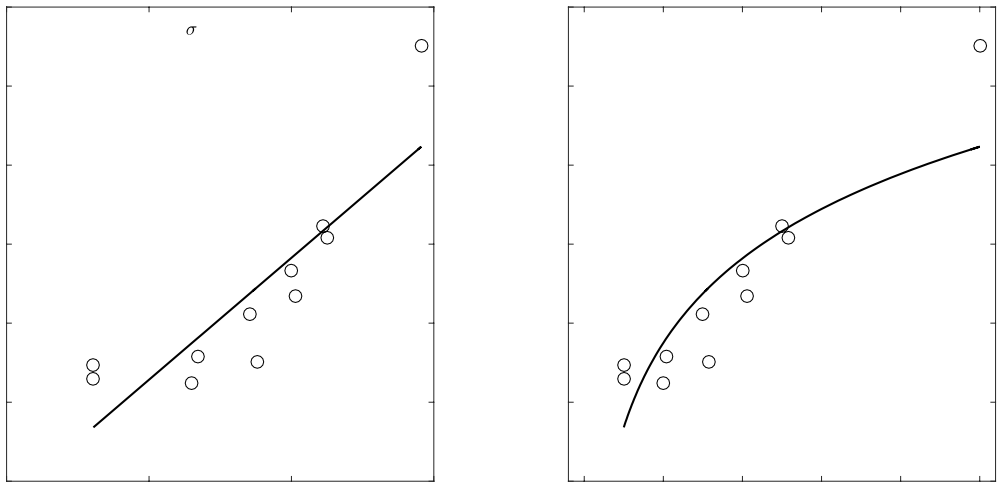

Figure B4:
Best logarithmic fit to peak amplitude versus normal stress for experiment p5062 with initial layer thickness of 8 mm using the flat block configuration.

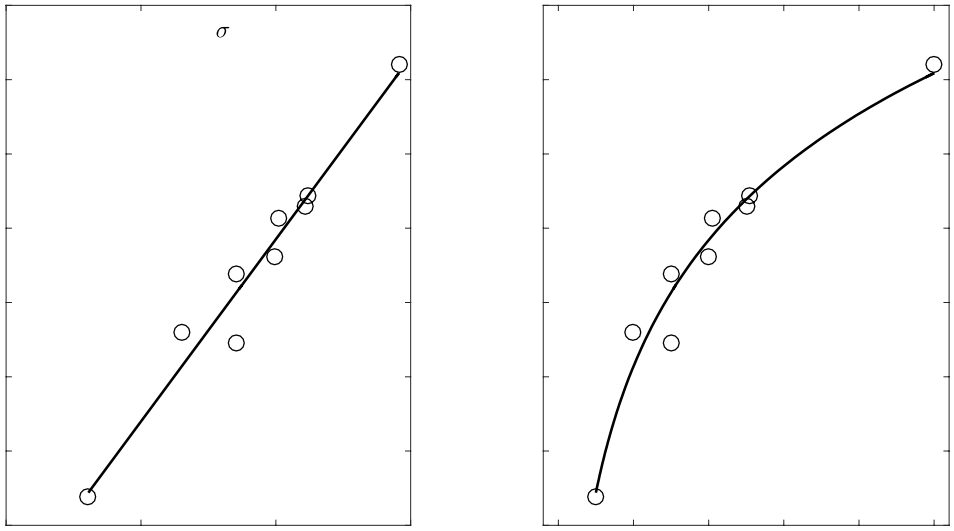

Figure B5:
Best logarithmic fit to peak amplitude versus normal stress for experiment p5078 with initial layer thickness of 3 mm using the grooved block configuration.

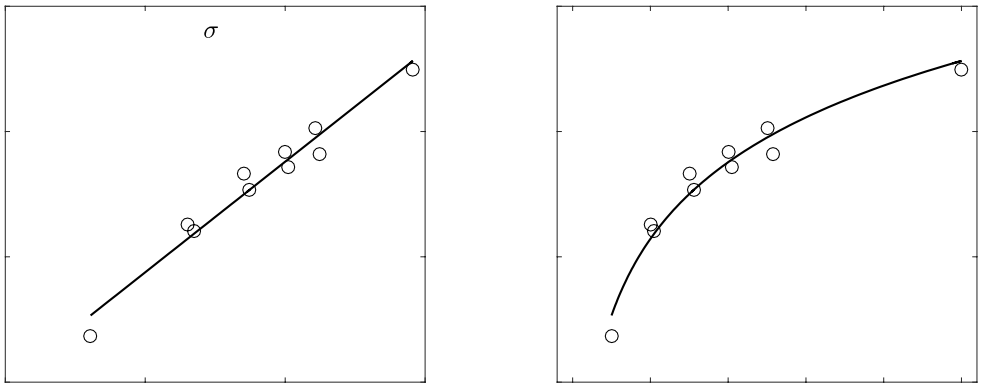

Figure B6:
Best logarithmic fit to peak amplitude versus normal stress for experiment p5080 with initial layer thickness of 5 mm using the grooved block configuration.

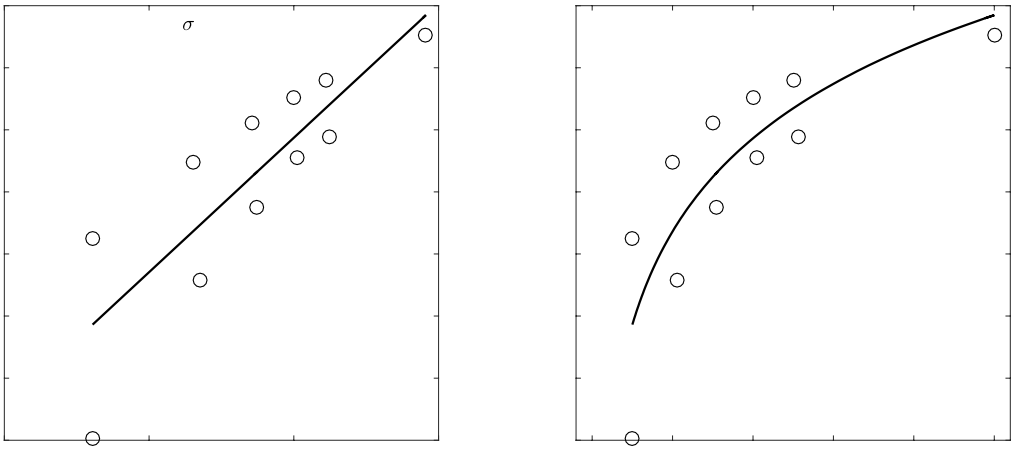

Figure B6:
Best logarithmic fit to peak amplitude versus normal stress for experiment p5082 with initial layer thickness of 8 mm using the grooved block configuration.

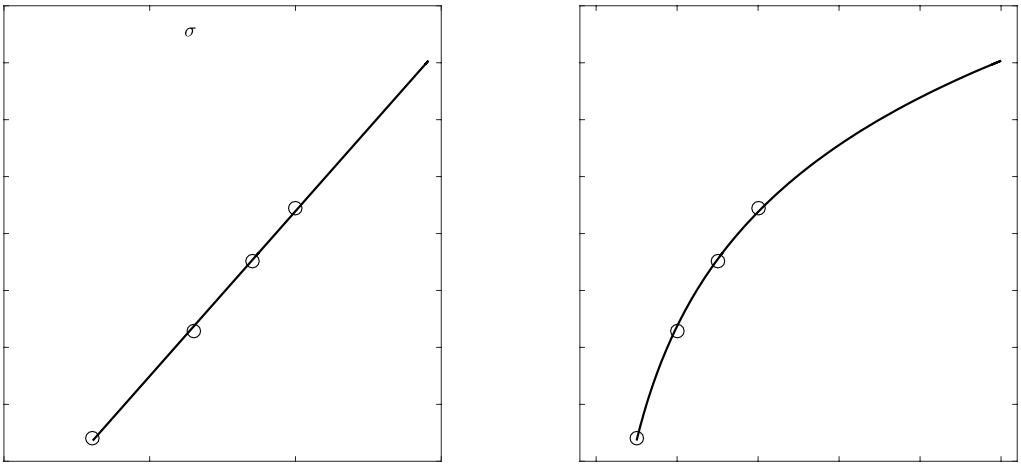

Figure B7:
Best logarithmic fit to peak amplitude versus normal stress for experiment p5083 with initial layer thickness of 16 mm using the grooved block configuration.

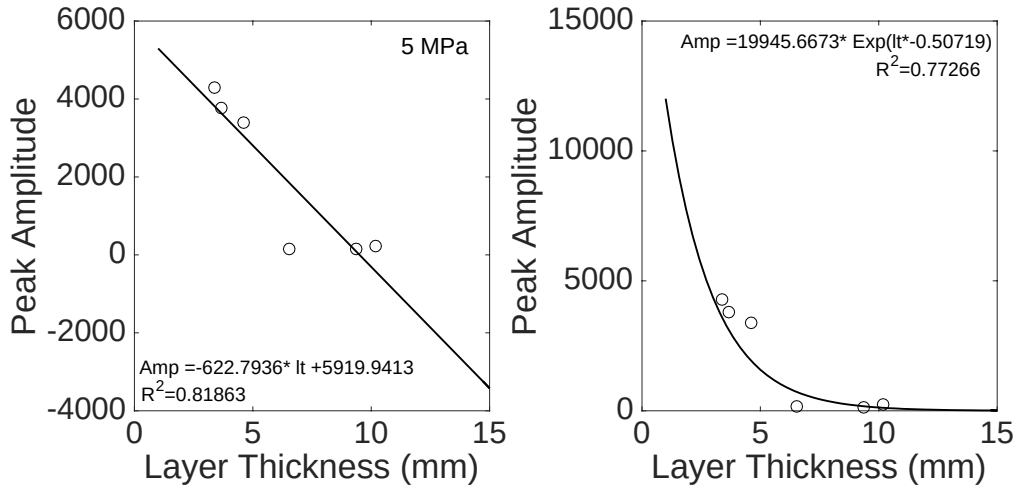

Figure B8:
Best linear (left) and exponential (right) fit to peak amplitude versus layer thickness at 5 MPa using flat block configuration.

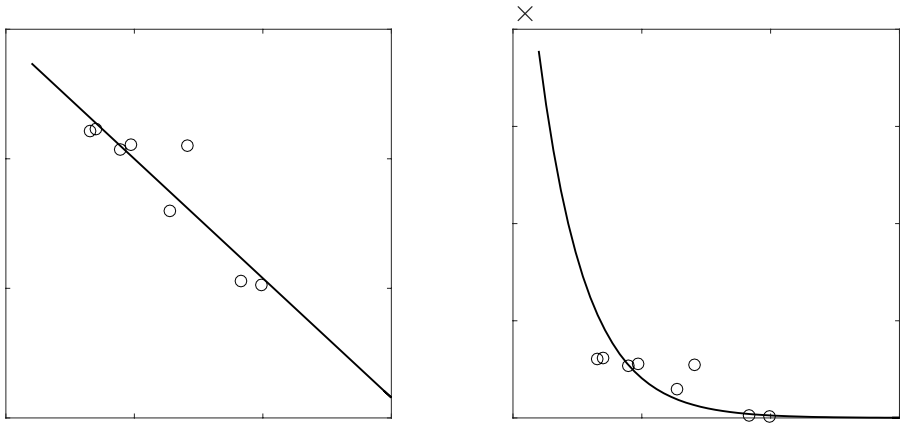

Figure B9:
Best linear (left) and exponential (right) fit to peak amplitude versus layer thickness at 10 MPa using flat block configuration.

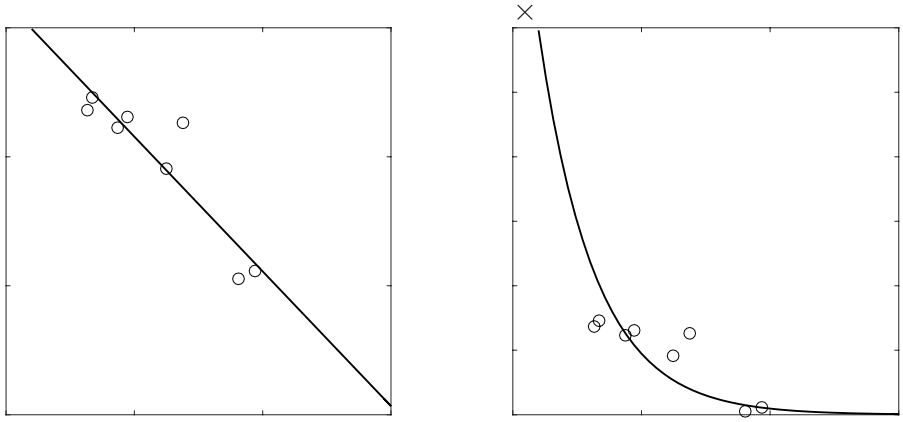

Figure B10:
Best linear (left) and exponential (right) fit to peak amplitude versus layer thickness at 15 MPa using flat block configuration.

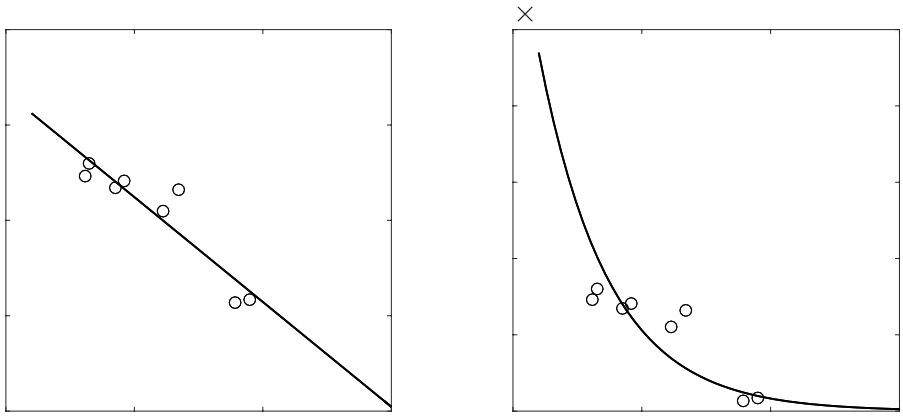

Figure B11:
Best linear (left) and exponential (right) fit to peak amplitude versus layer thickness at 20 MPa using flat block configuration.

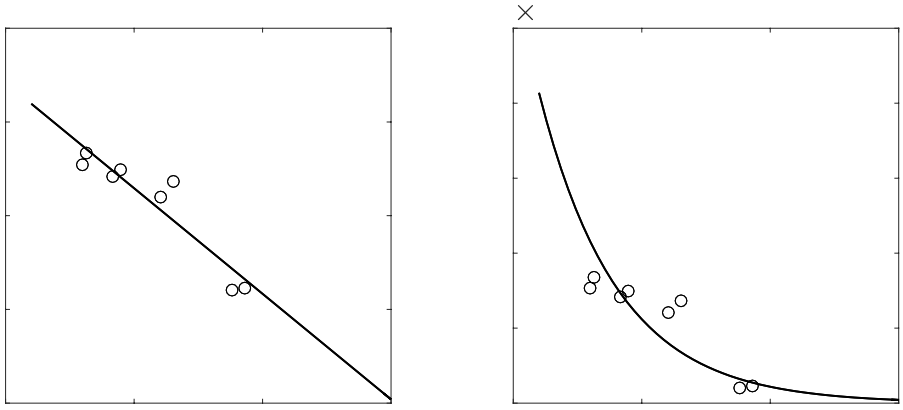

Figure B12:
Best linear (left) and exponential (right) fit to peak amplitude versus layer thickness at 25 MPa using flat block configuration.

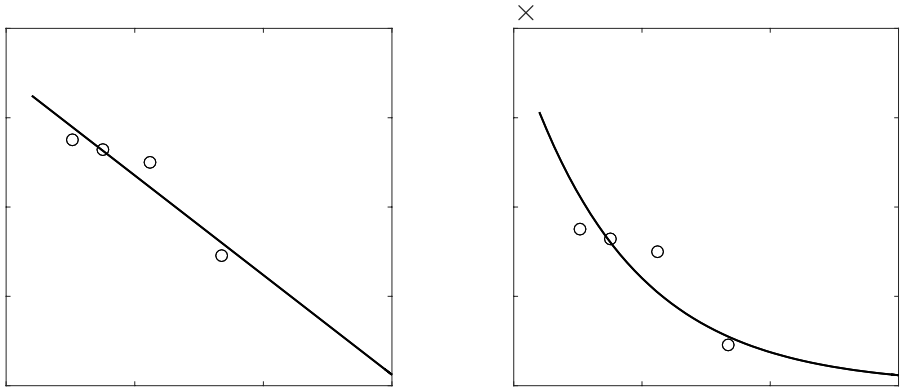

Figure B13:
Best linear (left) and exponential (right) fit to peak amplitude versus layer thickness at 50 MPa using flat block configuration.

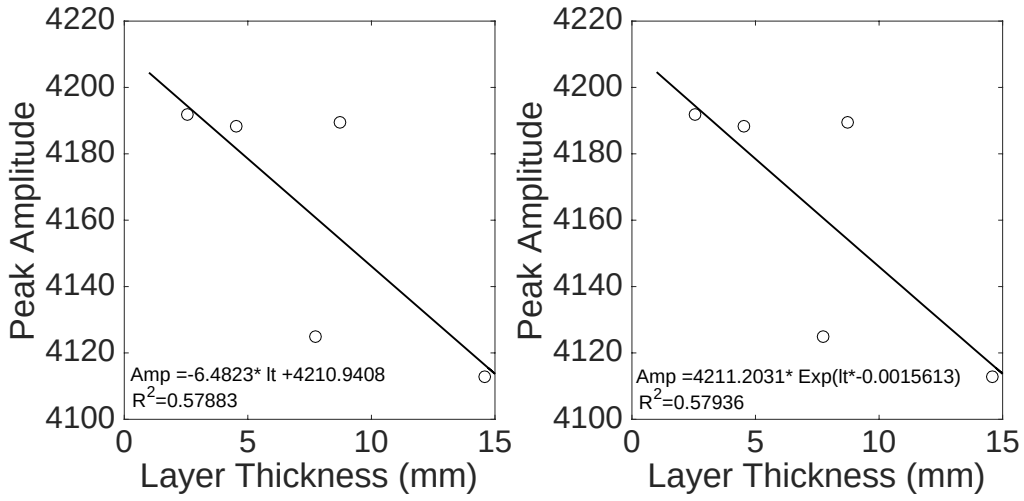

Figure B14:
Best linear (left) and exponential (right) fit to peak amplitude versus layer thickness at 5 MPa using flat grooved configuration.

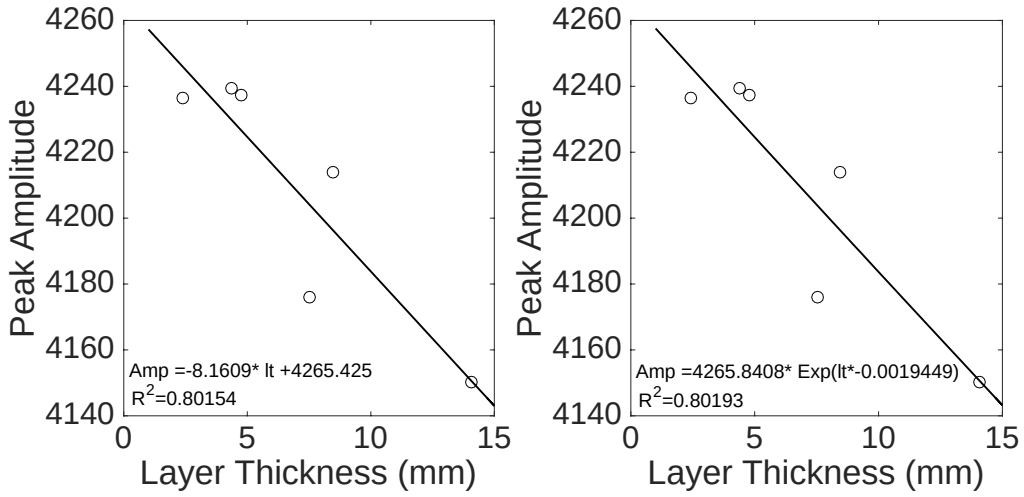

Figure B15:
Best linear (left) and exponential (right) fit to peak amplitude versus layer thickness at 10 MPa using flat grooved configuration.

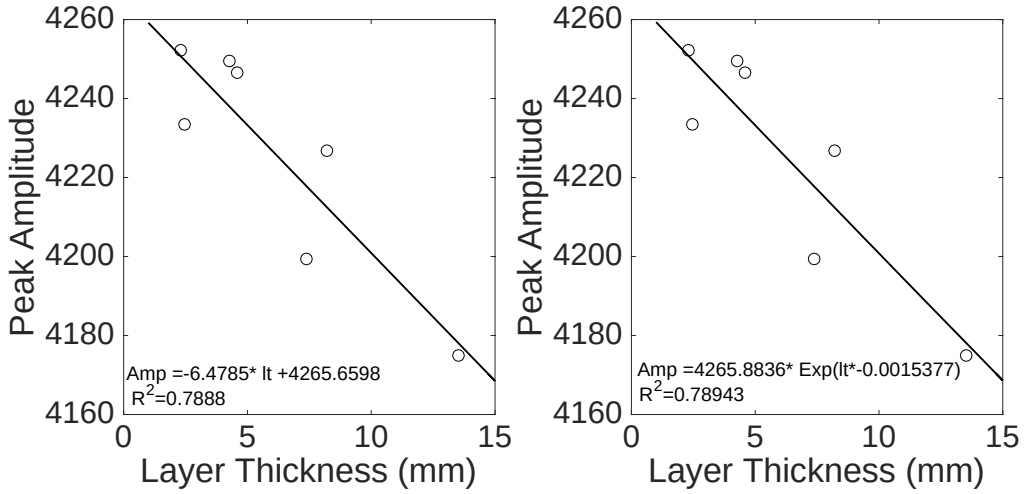

Figure B16:
Best linear (left) and exponential (right) fit to peak amplitude versus layer thickness at 15 MPa using flat grooved configuration.

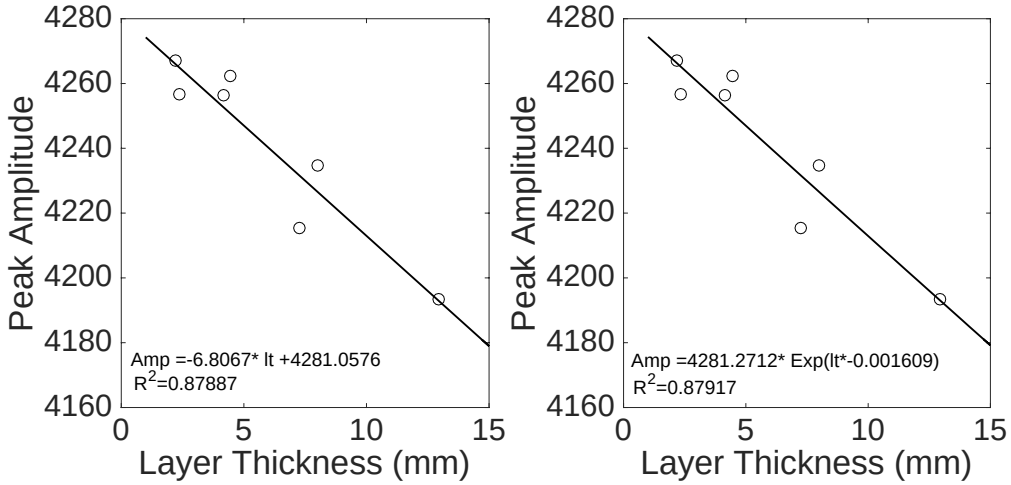

Figure B17:
Best linear (left) and exponential (right) fit to peak amplitude versus layer thickness at 20 MPa using flat grooved configuration.

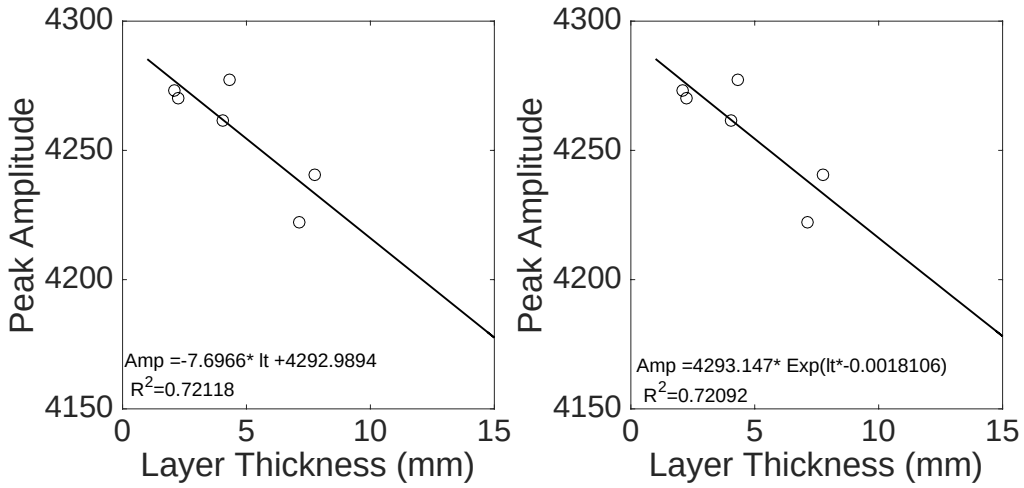

Figure B18:
Best linear (left) and exponential (right) fit to peak amplitude versus layer thickness at 25 MPa using flat grooved configuration.

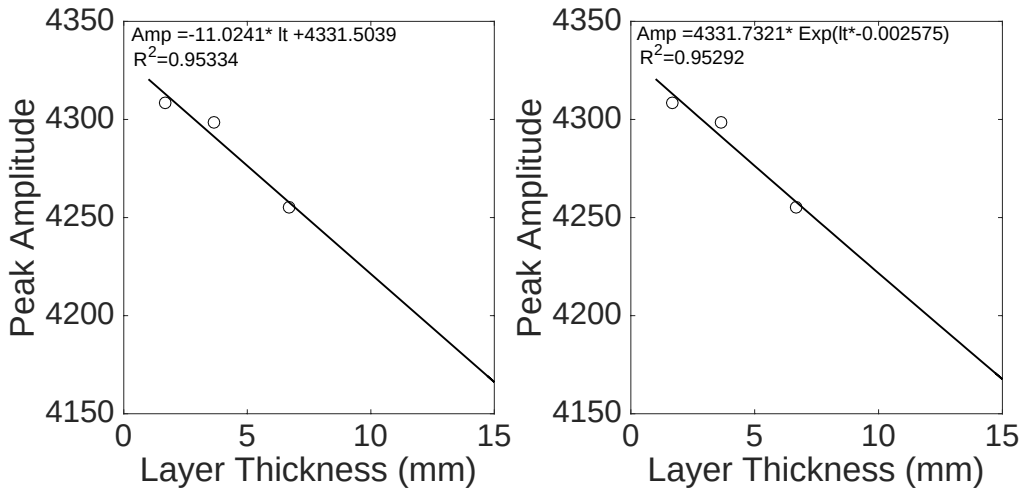

Figure B18:
Best linear (left) and exponential (right) fit to peak amplitude versus layer thickness at 50 MPa using flat grooved configuration.

Vita
Kerry L. Ryan

Education

The Pennsylvania State University June 2013-December 2018
- Ph.D. in Geosciences December, 2018

The College of New Jersey August 2009-May 2013
- Bachelor of Arts, Physics

Relevant Coursework

Petroleum Geosystems	Mathematical Modeling	Fault Mechanics
Seismology I & II	Techniques of Geoscientific Experimentation	
Geodynamics	Differential Equations	Thermal Physics
Continuum Mechanics		

Skills

Sound knowledge of programing fundamentals: experience with MATLAB and xlook
Working knowledge of Elfen and Techlog
Effective communication of scientific findings to audiences with varying backgrounds
4 years of collection and analysis of large data sets

Work Experience

Geoscience Internship, ExxonMobil **Fall 2017**
Structural Analysis and Geomechanics: Advanced capabilities and identified limitations of using Elfen finite element salt models for understanding trap architecture

Geoscience Internship, Noble Energy Inc. **Summer 2017**
East Canada Exploration: Modeled AVO responses using Rokdoc and compared with seismic observations

Geoscience Internship, Noble Energy Inc. **Summer 2016**
Reservoir Systems: Produced geomechanical model to optimize hydraulic fracturing in unconventional reservoirs.

Research Assistantship, The Pennsylvania State University **Summer 2013- current**
Conduct and analyze laboratory data from rock friction experiments

Teaching Assistant, The Pennsylvania State University **August 2013- Dec 2016**
Lead weekly lab exercises, developed and graded assignments, and met with students for Physical Processes in Geology and The Sea Around Us

Awards

Marathon Alumni Centennial Graduate Fellowship
Hess Corporation Exploration and Production Technology Scholarship
Shell Geosciences Energy Research Facilitation Award
Paul D. Krynine Scholarship
Charles E. Knopf, Sr., Memorial Scholarship